DEVELOPMENT OF AN OPTOMECHANICAL RESONATOR FOR LOW-FREQUENCY ACCELERATION SENSING

A Dissertation

by

ADAM SCOTT HINES

Submitted to the Graduate and Professional School of
Texas A&M University
in partial fulfillment of the requirements for the degree of

DOCTOR OF PHILOSOPHY

Chair of Committee,	Felipe Guzman
Committee Members,	John Junkins
	Manoranjan Majji
	Alexei Sokolov
Head of Department,	Ivett Leyva

December 2022

Major Subject: Aerospace Engineering

ABSTRACT

Low-frequency acceleration measurements are a vital component to many technologies and fields of science. High-precision, low-frequency accelerometers are used for inertial navigation, seismology, geophysics, satellite geodesy missions, gravitational wave detectors and more. However, many such devices are heavy, have large test masses, and are not easily portable, which limit the applications in which they can be deployed.

This dissertation covers the development of an optomechanical low-frequency accelerometer which couples monolithic fused silica mechanical resonators with compact high-precision optical readout systems. Fused silica has extremely low losses, which allows us to create highly sensitive devices with comparatively small test masses. Accelerometers that use such resonators are consequently more compact, lightweight, and portable.

These resonators are designed and simulated using finite element analysis and models based on first principles and detailed experimentation. Furthermore, prototype optomechanical accelerometers have been developed and tested in the laboratory, demonstrating the capability to detect seismic noise down to 1 mHz. These experimental studies have been conducted together with a commercial seismometer for comparison purposes. Finally, we present several fused silica resonator topologies developed for other inertial sensing applications.

CONTRIBUTORS AND FUNDING SOURCES

Contributors

This work was supported by a dissertation committee consisting of Professor Felipe Guzman and Professors John Junkins and Manoranjan Majji of the Department of Aerospace Engineering and Professor Alexei Sokolov of the Department of Physics.

The mechanical resonator presented in Chapter 2 was designed by Professor Felipe Guzman. The interferometric readout in Chapter 4 was designed, constructed, and tested by Dr. Yanqi Zhang and was published in 2021 [1]. The quasi-monolithic interferometer units in Chapter 6 was designed by Dr. Yanqi Zhang and tested by Dr. Yanqi Zhang, Dr. Xiangyu Guo, and Ian Harley. The atom interferometer design and analysis in Chapter 7 was conducted by Dr. Logan Richardson in collaboration with Andrew Schaffer (University of Arizona), Dr. Brian Anderson (University of Arizona), and Dr. Felipe Guzman and was published in 2020 [2].

All other work conducted for the dissertation was completed by the student independently.

Funding Sources

Graduate study was supported by the National Geospatial-Intelligence Agency (NGA) (grant HMA04762010016), National Science Foundation (NSF) (grant PHY-2045579), National Aeronautics and Space Administration (NASA) (grants 80NSSC20K1723 and 80NSSC22K0281), and Jet Propulsion Laboratory (JPL) (subcontracts 1659175 and 1677619).

TABLE OF CONTENTS

LIST OF FIGURES

LIST OF TABLES

1. INTRODUCTION

1.1 Accelerometry

The ability to measure accelerations is a core capability that is required for many different technologies and industries. A few select everyday applications of accelerometry include the electronic stability controls (ESCs) in automobiles [8], navigation in aircraft [9], and human activity detection in commercial electronics such as smartphones and smartwatches [10]. Furthermore, many scientific investigations require high-sensitivity acceleration measurements, the bandwidths of which varying by application. The Laser Interferometric Gravitational wave Observatory (LIGO) detectors, for example, use acceleration data ranging from the mHz regime to hundreds of Hz for active feedback seismic isolation and for identifying noise in the detectors in order to achieve test mass displacement stabilities on the order of $1 \times 10^{-19}\,\mathrm{mHz}^{-1/2}$. Satellite geodesy and climate experiments like the Gravity Recover And Climate Experiment (GRACE) and GRACE Follow-On (GRACE-FO) [11, 12] make use of on-board low-frequency accelerometers the detection of non-inertial forces such as radiation pressure and air drag so these effects can be removed from data. Moreover, space missions are especially challenging because the demand for high precision over a wide bandwidth is always in competition with the desire for small size, weight, and power (SWAP).

Accelerometers typically feature test masses which are subjected to the accelerations one wants to measure. By measuring the movement of the test mass, the acceleration that caused its motion can be recovered. The ultimate noise floor of an accelerometer is limited by the thermal motion of the test mass, which is in turn dependent on the size of the test mass and its mechanical loss coefficient. Large test masses made from low-loss materials offer lower thermal noise and better acceleration sensitivity. Many low-frequency accelerometers, such as commercial seismometers for example, use heavy test masses to obtain low acceleration noise [13]. This can result in sensors with total masses exceeding $10\,\mathrm{kg}$, which restricts their portability and is disadvantageous for applications such as field work or space mission applications. However, the need for large test masses can be lessened by utilizing low-loss materials. Fused silica glass, for instance, has demonstrated mechanical quality factors much greater than 1×10^6 [14, 15] whereas metals typically have Q-values of at most 1×10^3-1×10^4 [16]. To this end, we propose the use the use of fused silica to create high-sensitivity low-frequency accelerometers that are smaller and more portable than their commercial counterparts while maintaining competitive noise floors.

Moreover, many acceleration sensing technologies use electrostatic readouts to track the test mass motion. Micro-electromechanical systems (MEMS), for example, are used to make many different types of compact and highly portable sensors, including accelerometers and inertial sensors [17, 18]. However, their electrostatic readout scheme makes them sensitive to the local magnetic field and stray capacitances. Furthermore, MEMS devices typically exhibit noise floors several orders of magnitude worse than other types of accelerometers. Other examples of electrostatic accelerometers are the devices on-board the GRACE and GRACE-FO satellite constellations, which featured electrically suspended, quasi-free falling test masses. Despite demonstrating excellent acceleration sensitivities, these accelerometers could not be tested on ground, which posed significant challenges for the development of these experiments. As such, we also propose the use of optomechanical readout schemes which avoid the problems listed above by exploiting the exquisite temporal and spatial coherence of laser light to make precision displacement measurements.

1.2 Optomechanics

Optomechanics, which studies the interactions between optical and mechanical processes, has emerged over the past two decades as a promising solution for many high precision sensing applications. Devices developed using optomechanics include, but are not limited to, force sensors [19], magnetometers [20], displacement sensors [21], acoustic sensors, and atomic force microscopy. In the context of accelerometry, optomechanics is used to measure the displacement of the test mass. High-frequency optomechanical accelerometers have been developed using Fabry-Perot cavities which have demonstrated exquisite displacement sensitivities [22]. The nominal cavity length is tuned to have a resonance near the wavelength of the input laser beam. As the test mass oscillates, the cavity length and its resonant wavelength change in accordance with:

$$\frac{dL}{L} = \frac{d\lambda}{\lambda} \tag{1.1}$$

where L is the cavity length and λ is the resonant wavelength. The changing cavity resonance consequently changes the optical power transmitted and reflected by the cavity, the measurement of which is used to recover the test mass motion.

However, this cavity readout approach is limited to high-frequency devices which have relatively small dynamic test mass ranges. A $10\,\mathrm{kHz}$ mechanical resonator for example would deflect from equilibrium by only $2\,\mathrm{nm}$ under the force of gravity. A low-frequency device, can have displacements exceeding $1\,\mathrm{mm}$ under that same force. A cavity readout would not be appropriate for this case because the test mass can displace by many free spectral ranges of the cavity. Instead, heterodyne laser interferometry is a popular method for low-frequency test mass readout, being used in experiments such as the Laser Interferometer Space Antenna (LISA) Path Finder satellite [3]. Heterodyne inteferometry uses a Mach-Zedner type optical arrangement with two input beams of unlike frequency. As the test mass moves, a phase change is imprinted into the beatnote of the two beams, typically on the order of kHz or MHz. Measurement of the beatnote with a phasemeter allow for an observation of the test mass motion. As this project focuses on the development of a low-frequency optomechanical accelerometer, this heterodyne readout scheme will be used throughout the work presented in this dissertation.

1.3 Dissertation Outline

The work presented in this dissertation is developed in part from results of a combination of journal publications [23, 7] interlaced with supporting research and analyses that at this time have not been published. The chapters are organized as follows:

- Chapter 2 applies the research of the LIGO Scientific Collaboration (LSC) to a low-frequency fused silica resonator with parallelogram flexures to identify fundamentally limiting noise sources and ways to reduce them. Using theoretical and experimentally-derived models for various mechanical loss mechanisms, we predict the thermal motion of the resonator to estimate the lowest possible acceleration noise floor obtainable with this optomechanical resonator. Furthermore, we use finite element analysis (FEA) to simulate damping caused by air resistance and parasitic effects of the resonator mounting apparatus. Finally, preliminary characterization measurements of the resonator which demonstrate high mechanical $Q-$values are presented. This chapter is based on the journal publication [23].

- Chapter 3 discusses the drawbacks of the optomechanical resonator presented in Chapter 2 and uses the noise models developed in that chapter to optimize this resonator topology for low-frequency acceleration sensing.

- Chapter 4 presents a second iteration design of our optomechanical accelerometer with a new resonator and laser interferometer setup. We demonstrate our optomechanical accelerometer's ability to detect seismic noise by comparing results to those of a commercial seismometer. Moreover, we identify postcorrection methods of removing noise originating for the ambient environment and the laser source to improve our acceleration noise by as much as an order of magnitude. These results are then used to estimate the temperature stability and laser frequency stability required to achieve a thermally-limited acceleration measurement. This chapter is based on the journal publication [7].

- Chapter 5 investigates the temperature-dependent performance of our optomechanical accelerometer. Starting from theory, we derive equations predicting the change in mechanical resonance due to several thermal effects and compare to experimental results. Furthermore, we derive a model for the acceleration noise induced by the changing resonance.

- Chapter 6 discusses the process of integrating a compact heterodyne interferometer. New acceleration measurements are presented to demonstrate the device's seismic sensing capabilities as well as estimate its acceleration noise floor.

- Chapter 7 presents optomechanical resonator topologies designed for different applications, including a double-mass resonator for improved acceleration sensing over an extended bandwidth and a drum-head resonator for novel hybrid atom interferometry techniques. The atom interferometry portion of this chapter is based on the publication [2].

2. FIRST ITERATION LOW-FREQUENCY OPTOMECHANICAL ACCELEROMETER [*]

The development of a novel optomechanical accelerometer necessitates an in-depth understanding of its fundamental sensitivity limit to inform us on how to achieve the lowest acceleration noise floor we can. In high-frequency devices, this fundamentally limiting noise is approximately white, providing broadband sensing capabilities over kHz bandwidths or larger. Low-frequency, on the other hand, are known to be limited by pink noise that goes like $f^{-1/2}$, indicating that this class of devices is subject to fundamentally by different noise sources. Models for low-frequency acceleration noise can be derived from the work of the LIGO Scientific Collaboration, which has developed the theoretical framework of thermal noise and studied mechanical losses in fused silica glass. In this chapter, based on the article [23], we utilize these models to predict the acceleration noise floor of an optomechanical resonator, from which we argue that optomechanics has the potential to produce high-sensitivity inertial sensing devices that are competitive with commercial technologies. Moreover, we present an optomechanical resonator that can used to create a low-frequency accelerometer. We perform preliminary characterization measurements to demonstrate its acceleration sensing capabilities and compare the results to simulated values. The work presented in this chapter represents the starting point of this low-frequency optomechanical accelerometer project which later developments stem from. The work shown in this chapter was done in collaboration with Dr. Felipe Guzmán, Dr. Logan Richardson, and Hayden Wisniewski who all contributed to the experimental design. Furthermore, the fused silica resonator used in this chapter was designed by Dr. Guzmán. My contributions to this work include the construction of the experimental setup, data collection and analysis, and writing an article for journal publication.

We present a performance analysis of compact monolithic optomechanical inertial sensors that describes their key fundamental limits and overall acceleration noise floor. Performance simulations for low frequency gravity-sensitive inertial sensors show attainable acceleration noise floors

---

[*] Reprinted with permission from "Optomechanical inertial sensors" by Adam Hines, Logan Richardson, Hayden Wisniewski, and Felipe Guzman, 2020. Applied Optics, Vol. 59, pp. G167-G174, Copyright 2022 by Optica Publishing Group.

of the order of $1 \times 10^{-11}\,\mathrm{m/s^2/\sqrt{Hz}}$. Furthermore, from our performance models, we devised an optimization approach for our sensor designs, sensitivity, and bandwidth trade space. We conducted characterization measurements of these compact mechanical resonators, demonstrating mQ-products at levels of $250\,\mathrm{kg}$, which highlight their exquisite acceleration sensitivity.

2.1 Introduction

Commercially available high-sensitivity inertial sensors are typically massive systems that are not easily transportable and deployable due to their total mass and dimensions. Conversely, compact commercial systems, while easily transportable and field capable, exhibit comparatively higher acceleration noise floors, especially at low frequencies.

Spring gravimeters and relative gravimeter technologies [24, 25, 26] tend to be large, expensive, and offer limited sensitivity. These systems use a mass-spring system, which measures the local acceleration by tracking the spring extension [27, 28], usually with electrostatic measurement techniques. One such example is the Scintrex CG-6 gravimeter that can achieve acceleration sensitivities of $10^{-9}\,\mathrm{g/\sqrt{Hz}}$ over a bandwidth of up to $10\,\mathrm{Hz}$ [29]. Superconducting relative gravimeters create ideal springs by levitating a superconducting niobium sphere in a non-uniform magnetic field [30, 31]. In this way, one can measure the local gravity with a sensitivity of $10^{-9}\,\mathrm{m/s^2\sqrt{Hz}}$ over a bandwidth of $250\,\mathrm{mHz}$ [32]. However, due to the intensive operation requirements and maintenance, these systems are not suitable for deployment, since exposure to large accelerations, as usual in the field, can cause jumps in the data. Micro-electromechanical systems (MEMS) are typically small and low-cost in comparison to other types of gravimeters and utilize small mass-spring systems that are read out electrostatically. Recent development in MEMS devices have demonstrated sensitivities at levels of $30\,\mathrm{ng/\sqrt{Hz}}$ over a bandwidth of $1\,\mathrm{Hz}$ [17, 33, 18], however, these sensitivity levels are comparatively lower by one to two orders of magnitude with respect to other commercial systems.

Absolute gravimeters, such as the Micro-G Lacoste FG5 and atom interferometers, offer long term stability in gravitational measurements [34, 35, 2]. When operated alone, however, they are susceptible to external vibrations, which obscure the acceleration measurement and ultimately limit the performance and their deployment capabilities for field operation [34, 36]. Furthermore, the Micro-G Lacoste FG5 require cost-intensive and frequent calibrations, and the aging of the springs causes drift over time.

Advances in optomechanics over the past decade and research into their fundamental limits have paved the way for the development of novel compact and highly sensitive inertial sensors operating at low frequencies [37]. The thermal acceleration noise floor and mechanical losses have been studied extensively, for example, in the context of suspensions and mechanical systems for ground-based gravitational wave observatories, such as the Laser Interferometer Gravitational-Wave Observatory (LIGO)[38, 39].

In this dissertation, we present the results of investigations regarding compact optomechanical inertial sensors that consist of monolithically micro-fabricated fused silica mechanical resonators and experimentally demonstrate high acceleration sensitivities and measure mQ-products above $240\,\mathrm{kg}$. Furthermore, we studied the mechanics of compact mechanical resonators using computational simulations, particularly on various loss mechanisms that would impact their sensitivity and conducted a trade-off analysis to determine resonator topologies that exhibit the best performance. These results inform our efforts to develop novel compact and highly sensitive optomechanical inertial sensors, as presented in this dissertation.

Our optomechanical sensors provide numerous advantages over traditional acceleration sensing technologies due to their comparatively compact size and low mass, as well as their inherent vacuum compatibility, optical readout, and monolithic composition. Here, we present an optomechanical resonator, capable of achieving acceleration noise floors at levels of $1 \times 10^{-11}\,\mathrm{m/s^2/\sqrt{Hz}}$ with a footprint of $48\,\mathrm{mm} \times 92\,\mathrm{mm}$ and a mass of $26\,\mathrm{g}$, making it small and transportable. The optical laser-interferometric readout of our sensor provides a significantly higher sensitivity than typical electrostatic techniques, and is insensitive to external electro-magnetic fields. Moreover, our sensors are monolithically fabricated from very low loss materials, such as fused silica, allowing us to achieve high mechanical quality factors. This oscillator is intended to be installed and operated inside a compact and portable vacuum package with a miniaturized high-sensitivity laser displacement interferometer that is currently under development [40].

Similar compact, monolithic, optomechanical sensors with high resonant frequencies have already shown by Guzmán *et al.* to have excellent acceleration noise floors at the nano-g $\sqrt{\mathrm{Hz}}$ level over $10\,\mathrm{kHz}$, as well as laser-interferometric displacement sensitivites of $1 \times 10^{-16}\,\mathrm{m}/\sqrt{\mathrm{Hz}}$ [22]. However, the sub-Hz regime is an under-explored design space for optomechanical accelerometers.

In this chapter we present a prototype optomechanical sensor with a resonant frequency of $10\,\mathrm{Hz}$ that targets high acceleration sensitivities at low frequencies. Lowering the resonant frequency of the sensor increases the acceleration sensitivity and greatly expands the utility, especially for space applications. The portability, comparatively low cost, and monolithic composition of our devices make them excellent candidates for a broad spectrum of applications, including gravimetry and gravity gradiometry, geodesy, seismology, inertial navigation, vibration sensing, metrology, as well as other applications in geophysics. The sensor design and performance modelling presented in this dissertation allow us to understand how we can use optomechanical sensors as low frequency accelerometers, and to understand their sensitivity limits.

2.2 Sensitivity and losses in optomechanical inertial sensors

Our sensor consists of monolithic fused silica resonators based on a parallelogram dual flexure design that supports the oscillating acceleration-sensitive test mass (Figure 2.1). We use a displacement readout laser interferometer to measure the dynamics of the test masses (Section 2.5). The total mass of our resonator head is approximately $26\,\mathrm{g}$ with an oscillating test mass of $0.95\,\mathrm{g}$. The spring flexures supporting the test mass are $0.1\,\mathrm{mm}$ thick by $60\,\mathrm{mm}$ long which yields a resonance frequency of about $10\,\mathrm{Hz}$. We place an aluminum-coated fused silica mirror on top of the test mass with no adhesive for the laser interferometer, which reduces the measured resonant frequency to $3.8\,\mathrm{Hz}$ due to the added $1.25\,\mathrm{g}$ mass. Micro-fabricated by laser-assisted dry-etching, the overall resonator is $48\,\mathrm{mm}$ x $92\,\mathrm{mm}$ x $3\,\mathrm{mm}$, making it very compact, and is constructed from a monolithic fused silica wafer for its low-loss properties at room temperature [41], which makes these devices easy to operate and deploy in the field. Low losses in fused silica result in low frequency-dependent damping, high mechanical quality factors, and low thermal noise.

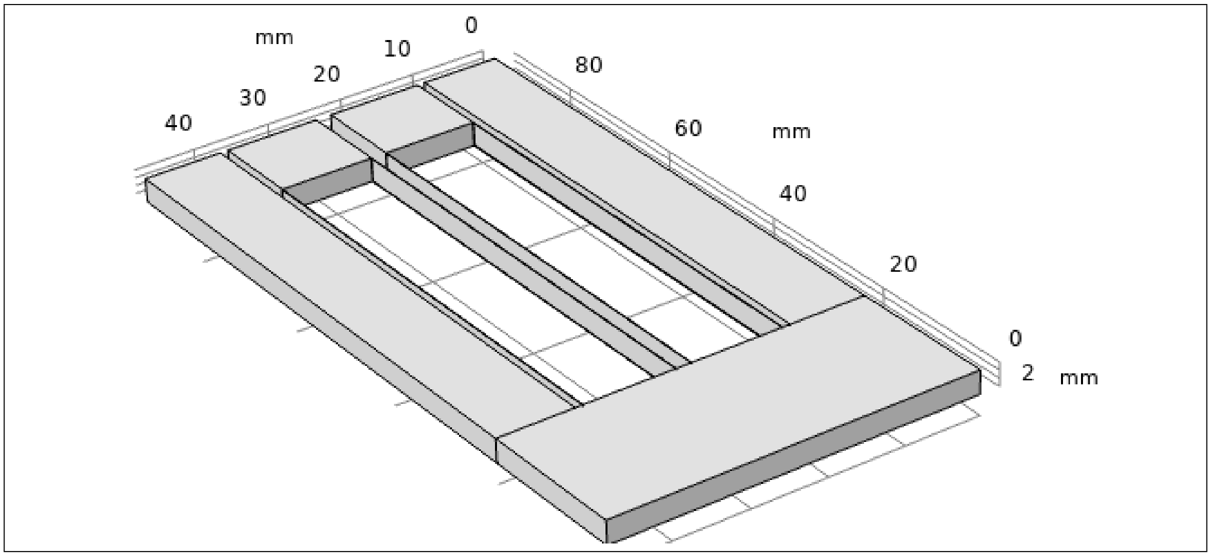

Figure 2.1: Geometry of our optomechanical resonator generated in COMSOL. From this model, we calculate the mechanical properties of our sensor, including the resonant frequency and energy loss mechanisms. The sensor described in this work has overall dimensions of $48\,\mathrm{mm} \times 92\,\mathrm{mm} \times 3\,\mathrm{mm}$ and mass of $26\,\mathrm{g}$. Two oscillating test masses each with a mass of $0.95\,\mathrm{g}$ are supported by two flexures each with a thickness of $100\,\mu\mathrm{m}$.

The acceleration sensitivity of the optomechanical sensors is limited by the thermal noise floor of its oscillating test mass and the sensitivity of the test mass displacement sensor. Thermal noise has been experimentally observed in optomechanical systems for frequencies on the order of 3-$100\,\mathrm{Hz}$ [42]. However, our inertial sensor is intended to measure signals in the sub-Hz regime, which requires the analysis of the behavior of loss mechanisms and potentially limiting effects at low frequencies.

Within an optomechanical resonator, there are various mechanisms that dissipate energy. These mechanisms can be separated into two categories: external velocity damping (*eg.* gas damping) and internal damping (*eg.* surface damage). Therefore, we treat the resonator as a mass-spring system with a velocity damping term and a complex spring constant. The equation of motion of such a system is given by [43]:

$$F = m\ddot{x} + m\Gamma_v\dot{x} + m\omega_0^2(1 + i\phi(\omega))x, \tag{2.1}$$

where m is the resonator's mass, Γ_v is the velocity damping rate, ω_0 is the resonant frequency, and $\phi(\omega)$ is the loss coefficient for internal losses. The thermal motion of the resonator is derived from Equation 2.1 via the Fluctuation-Dissipation Theorem [43]. Using this technique, we find the power spectral density of the thermal motion to be:

$$x_{th}^2(\omega) = \frac{4k_BT}{m\omega}\frac{\omega\Gamma_v + \omega_0^2\phi(\omega)}{(\omega_0^2-\omega^2)^2 + (\omega\Gamma_v + \omega_0^2\phi(\omega))^2}, \tag{2.2}$$

where k_B is Boltzmann's constant, T is temperature, and ω is angular frequency. Furthermore, from Equation 2.1 we also note that the transfer function relating displacement to acceleration is given by:

$$\frac{x(\omega)}{a(\omega)} = \frac{-1}{\omega_0^2 - \omega^2 + i(\omega\Gamma_v + \omega_0^2\phi(\omega))}. \tag{2.3}$$

Using Equation 2.2 and Equation 2.3, we immediately find that the thermal acceleration noise is given by:

$$a_{th}^2(\omega) = \frac{4k_BT}{m\omega}(\omega\Gamma_v + \omega_0^2\phi(\omega)). \tag{2.4}$$

By inspection, we see that in the high-frequency regime ($\omega\Gamma_v >> \omega_0^2\phi(\omega)$), Equation 2.4 is dominated by velocity damping and asymptotically approaches a constant. This is consistent with observations of uniform thermal noise at high frequencies. At low frequencies, however, the thermal acceleration noise is dominated by internal losses and has a ω^{-1} dependence.

In order to predict the thermal motion of our optomechanical resonator, we need to know the velocity damping rate and the mechanical loss coefficient. The velocity damping is dominated by gas damping, which is determined computationally and is discussed further in Section 2.42.4.1. The mechanical loss coefficient originates from four main loss mechanisms in our resonators: bulk losses, surface losses, thermoelastic losses, and anchor losses. Thus, the total mechanical loss in the resonator is given by [38, 39]:

$$\phi(\omega) = \phi_{surface} + \phi_{bulk}(\omega) + \phi_{thermo}(\omega) + \phi_{anchor}(\omega). \tag{2.5}$$

In our analysis, we assume negligible variation in flexure thickness, which was experimentally verified by microscope measurements to be less than $10\,\mu\mathrm{m}$ along the full length. Furthermore, since elastic energy is stored in the flexures, we do not consider the test mass geometry in our analysis. We further discuss this point in Section 2.3.

2.2.1 Bulk and Surface Losses

Bulk losses are a result of energy losses intrinsic to the material. We use the model experimentally determined by Penn *et al.* [44] to determine the contribution from bulk losses in our resonator:

$$\phi_{bulk}(\omega) = 7.6 \times 10^{-10}\left(\frac{\omega}{2\pi}\right)^{0.77}. \tag{2.6}$$

Surface losses encapsulate the intrinsic losses at the surface of the material resulting from damage, or surface imperfections from manufacturing process. We can model surface losses for an arbitrary flexure shape as[45]:

$$\phi_{surface} = \mu h \phi_s \frac{S}{V}, \tag{2.7}$$

where μ is a constant dependent on the shape of the flexure, h is the skin-depth of the surface, ϕ_s is the intrinsic loss at the surface, S is the surface area of the flexure, and V is its volume. The fabrication of our resonator could lead to a substantial amount of surface losses if the surface quality is non-ideal. However, the surface losses for ideal fused silica is better documented than that for non-pristine samples. To determine the surface losses for ideal flexures in a given geometry, we model the surface losses of ideal fused silica fibers; such as those which are flame or laser-pulled and exhibit high surface quality. For such fibers, Gretarsson *et al.* experimentally determined $h\phi_s$ to be $6.15\,\mathrm{pm}$. For a flexure with a rectangular cross section, Equation 2.7 becomes:

$$\phi_{surface} = \frac{3+A}{1+A} h \phi_s \frac{2(x+y)}{xy}, \tag{2.8}$$

where x and y are the flexures cross-section dimensions, and A is the aspect ratio of the rectangular cross-section [45]. Our flexures have $0.1\,\mathrm{mm} \times 3\,\mathrm{mm}$ cross-section and an aspect ratio of 30.

Mechanism	Expected Value at $10\,\mathrm{mHz}$
Surface	1.3×10^{-7}
Thermoelastic	2.9×10^{-10}
Bulk	2.2×10^{-12}

Table 2.1: A summary of the intrinsic loss mechanisms and their expected values for frequencies at $10\,\mathrm{mHz}$. These values were obtained by evaluating Equations 2.6, 2.8, and 2.9 using the material properties of fused silica.

2.2.2 Thermoelastic Losses

Thermoelastic losses describe bending of the flexures due to spontaneous temperature fluctuations and can be theoretically derived from:

$$\phi_{thermo}(\omega) = \frac{YT\alpha^2}{\rho C}\frac{\omega\tau}{1+\omega^2\tau^2}, \tag{2.9}$$

where Y is the Young's modulus, ρ is the mass density, C is the specific heat capacity, and α is the coefficient of thermal expansion [38, 39]. For fused silica, these values are $Y = 72\,\mathrm{GPa}$, $\rho = 2.2 \times 10^3\,\mathrm{kg\,m^{-3}}$, $C = 6.7 \times 10^2\,\mathrm{J\,kg^{-1}}$, and $\alpha = 5.5 \times 10^{-7}\,\mathrm{K^{-1}}$. In our simulations we assume operation at room temperature, $T = 293\,\mathrm{K}$. The term τ is the characteristic time needed for heat to travel across the cross section of the flexure. For rectangular cross sections, this time is given by:

$$\tau = \frac{\rho C t^2}{\pi^2 \kappa}, \tag{2.10}$$

where t is the thickness of the flexure and κ is the thermal conductivity [38, 39]. The thermal conductivity of fused silica is taken to be $\kappa = 1.4\,\mathrm{W\,m^{-1}\,K^{-1}}$.

A summary of the different intrinsic loss mechanisms is shown in Table 2.1, outlining the expected losses at $10\,\mathrm{mHz}$. We find that at this frequency, surface losses are the main dominant factor by nearly three orders of magnitude.

2.3 Optomechanical Inertial Sensor Performance

From Equation 2.2 and Equation 2.4, we can calculate the individual contributions from each loss mechanism to compute the expected displacement and acceleration amplitude spectral densities for a given resonator. Assuming operation at sufficiently low pressures for the velocity damping rate to be negligible with respect to other loss mechanisms, we show the computed linear spectral densities in Figures 2.2 and 2.3. For an oscillator with a resonant frequency of $3.8\,\mathrm{Hz}$ and a test mass $m = 2.2\,\mathrm{g}$, surface losses dominate the spectrum at low frequencies with thermoelastic losses only becoming relevant near resonance. We observe that bulk losses are a much smaller contribution compared to the other mechanisms for the bandwidth of interest. This is consistent with Equations 2.6, 2.7, and 2.9, which suggest that the bulk losses are several orders of magnitude smaller than those from the other loss mechanisms.

2.4 Computational analysis

2.4.1 Simulated gas damping

To better understand how the flexure and test mass geometry affect loss mechanisms, we utilized finite element analysis and modeled our resonator in COMSOL 5.4 (see Figure 2.1). We used the Solid Mechanics module to calculate the eigenfrequencies of the resonator, and the Creeping Flow fluid dynamics module to estimate the quality factor of this resonator at atmospheric pressure. We modeled the mechanical oscillator assuming a large airbox surrounding the test mass and its flexures. The inlet and outlet of the air box were given a pressure differential that generated a $1\,\mathrm{\mu m\,s^{-1}}$ air current at the test mass position. We used COMSOL to calculate the steady-state solution to this airflow, and we found the net force acting on the test mass by integrating the pressure over its surface (Figure 2.4). From the calculated force, we found the linear drag coefficient, and then we applied the air resistance to the test mass as a boundary load. Performing an eigenfrequency analysis, this time without the air box, COMSOL produced the mechanical quality factor of the resonator in air. For our $10\,\mathrm{Hz}$ resonator, we found this Q to be $\approx 7.0 \times 10^2$ with a damping rate of $9.0 \times 10^{-2}\,\mathrm{s^{-1}}$.

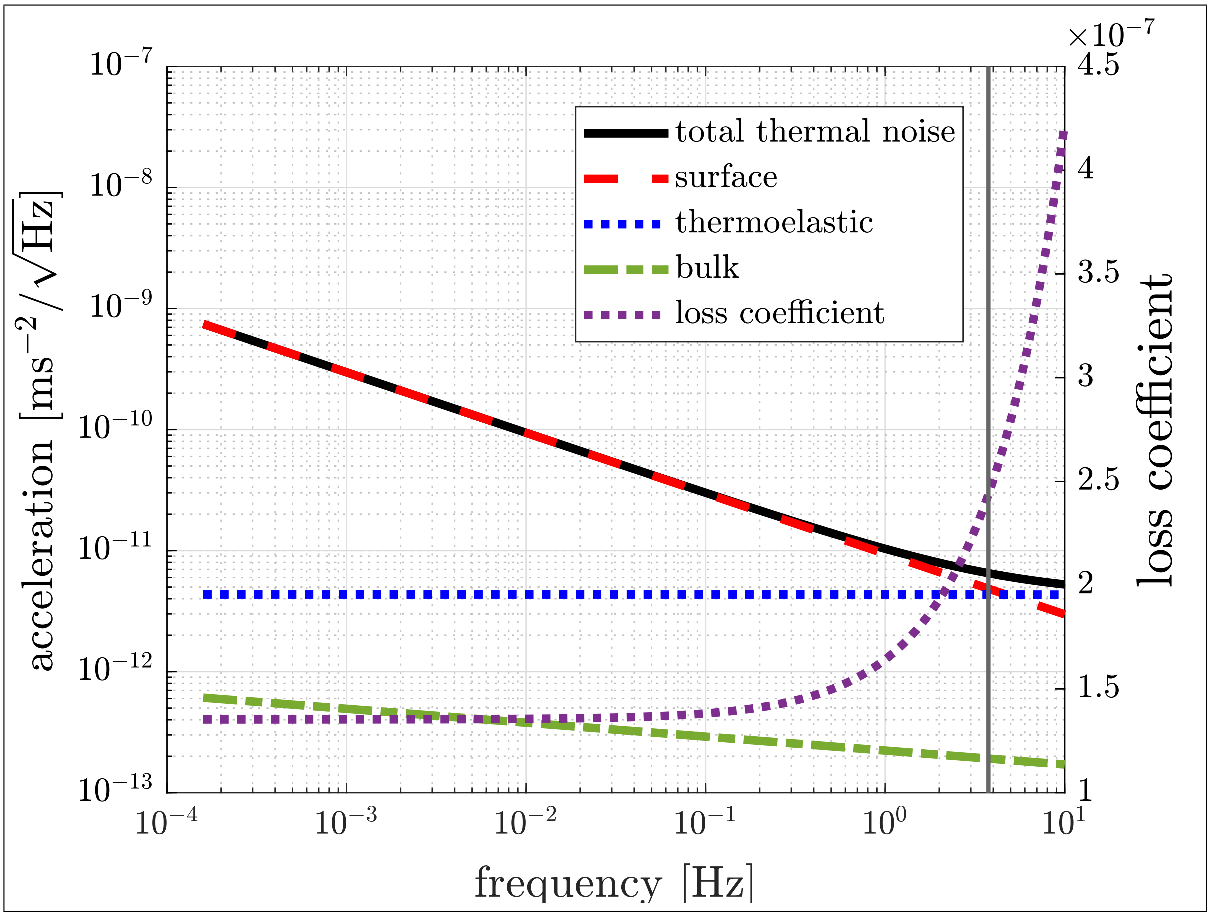

Figure 2.2: The calculated linear spectral density of acceleration thermal noise for a $3.8\,\mathrm{Hz}$, $2.2\,\mathrm{g}$ test mass is plotted on the left axis. The resonant frequency is denoted by a vertical line. We also plotted the contribution from each loss mechanism, from which we can see that surface losses are the dominant noise source for frequencies below resonance. On the right axis, the loss coefficient is plotted as a function of frequency.

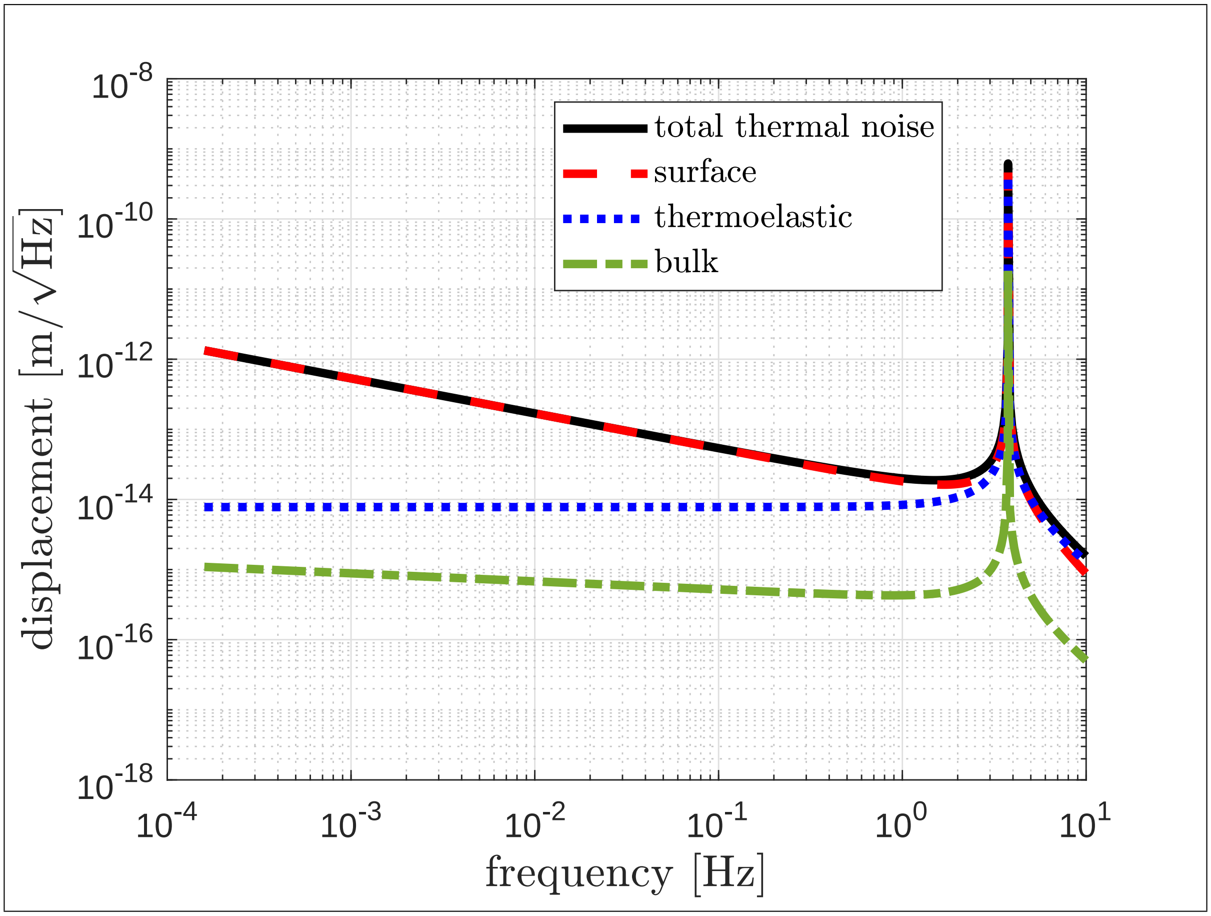

Figure 2.3: Calculated linear spectral density of displacement thermal noise floor for a $3.8\,\mathrm{Hz}$, $2.2\,\mathrm{g}$ test mass. Each loss mechanism's contribution is included. As shown, a read-out system would need to have a displacement sensitivity on the order of $1 \times 10^{-14}\,\mathrm{m}/\sqrt{\mathrm{Hz}}$ to resolve the thermal noise floor.

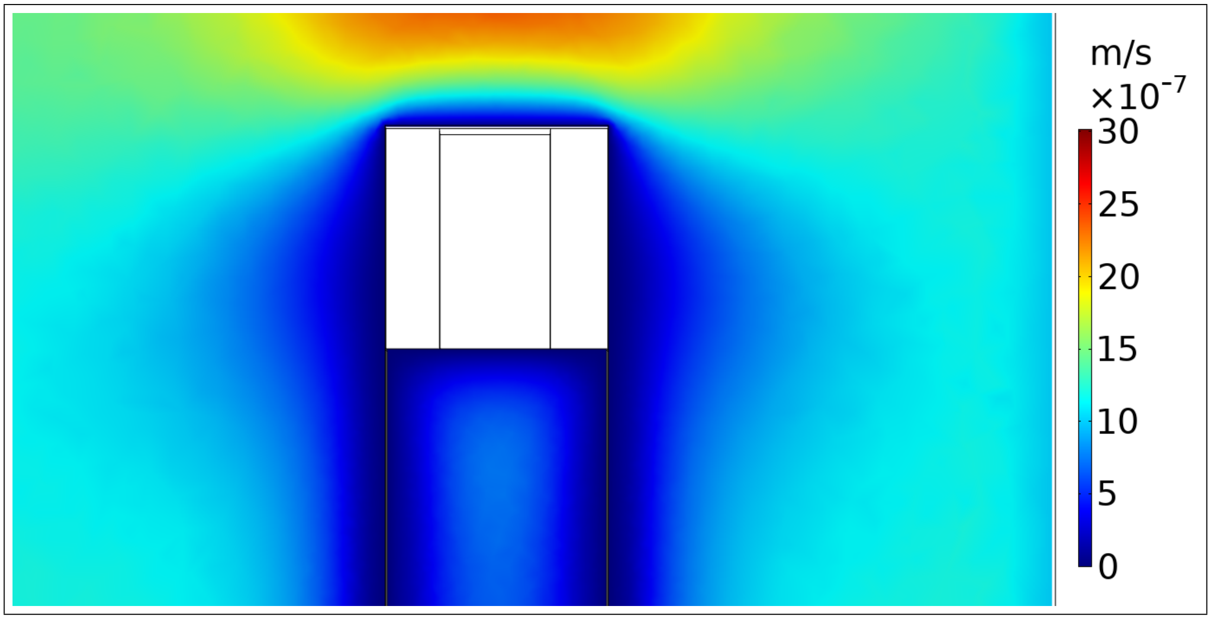

Figure 2.4: Simulated airflow around an optomechanical resonator. Lighter colors indicate higher airflow speed, whereas darker colors indicate a lower velocity. The inlet of the airflow is the left of the test mass, causing the air to move to the right. By integrating the pressure along the surface of the test mass and flexure, we compute the air drag force and mechanical quality factor of the resonator at atmospheric pressures.

2.4.2 Simulated elastic energy distribution

To support the claim that we only need to consider the flexure geometry to calculate the mechanical losses, we use COMSOL to calculate the elastic energy density throughout the resonator. When performing an eigenfrequency analysis of the resonator, COMSOL outputs the distribution of elastic energy. From this, we calculate that over 99% of the elastic energy is located within the flexures, 0.14% is within the test mass, and 0.09% is within the remainder of the fused silica wafer. We depict the elastic energy density in Figure 2.5. Evaluation of the bulk, surface, and thermoelastic losses for the test mass yields a mechanical loss coefficient of 2.0×10^{-7}. However, when weighted by the amount of elastic energy stored in the test mass, this gives a net mechanical loss coefficient of 2.9×10^{-10}. This value is negligible since it is more than three orders of magnitude lower than the losses in the flexures ($\approx 4.8 \times 10^{-7}$). Furthermore, the fraction of the energy stored in the mirror on the test mass was found to be 6.9×10^{-8}, suggesting that the losses from the mirror are negligible as well.

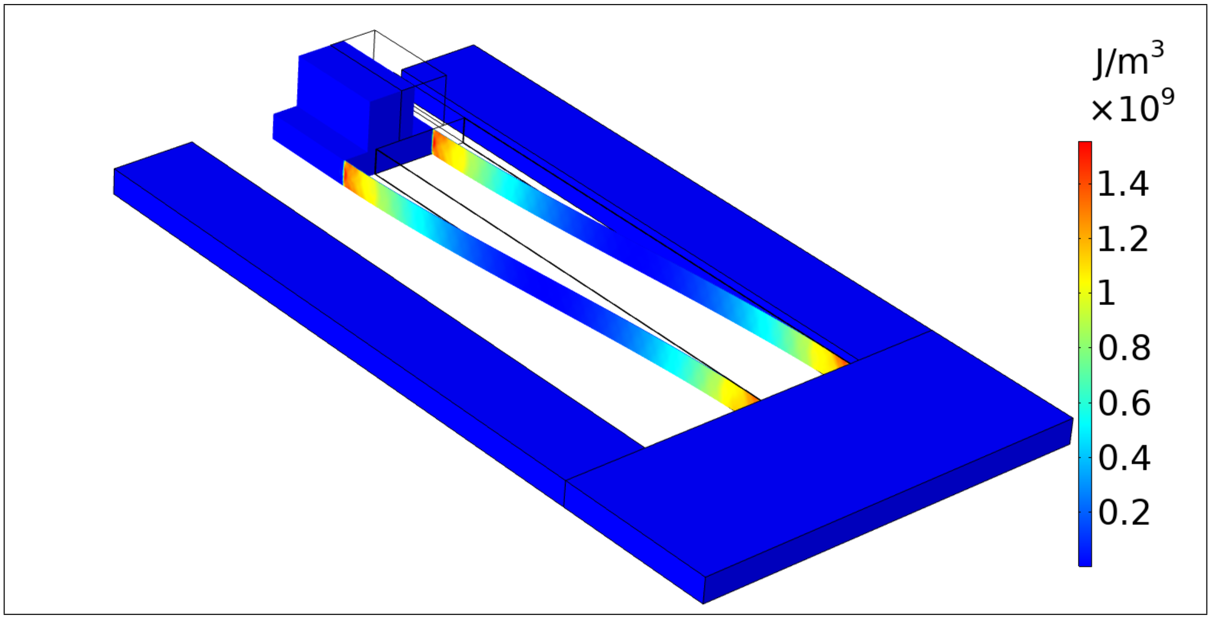

Figure 2.5: A COMSOL simulation of the elastic energy density in our inertial resonator at its resonant frequency with a mirror on top of the test mass. The units on the legend are arbitrary. In this figure, red represents a greater energy density, and blue indicates a low energy density. The outline represents the equilibrium position of the test mass. From this simulation, we confirm that mechanical losses in our resonator are mostly located within the flexures, as opposed to within the test mass.

2.4.3 Simulated anchor losses

We can extend this exercise to estimate anchor losses by modeling the mounting apparatus. To mitigate anchor losses, and for the purpose of testing and characterizing our optomechanical inertial sensor, we fabricated a mount for the resonator that reduces the contact area between the fused silica and the rough aluminum surface of the mount with higher losses. This mount holds the resonator in place using thirteen $3/32\mathrm{inch}$ diameter aluminum ball bearings, which limits the amount of energy lost to the mounting apparatus, and allows us to tilt the sensor vertically. Figure 2.6 depicts a computer rendering of this mount. The eigenfrequency analysis tells us that the fraction of the elastic energy contained within the ball bearings is 3.4×10^{-7}. The internal

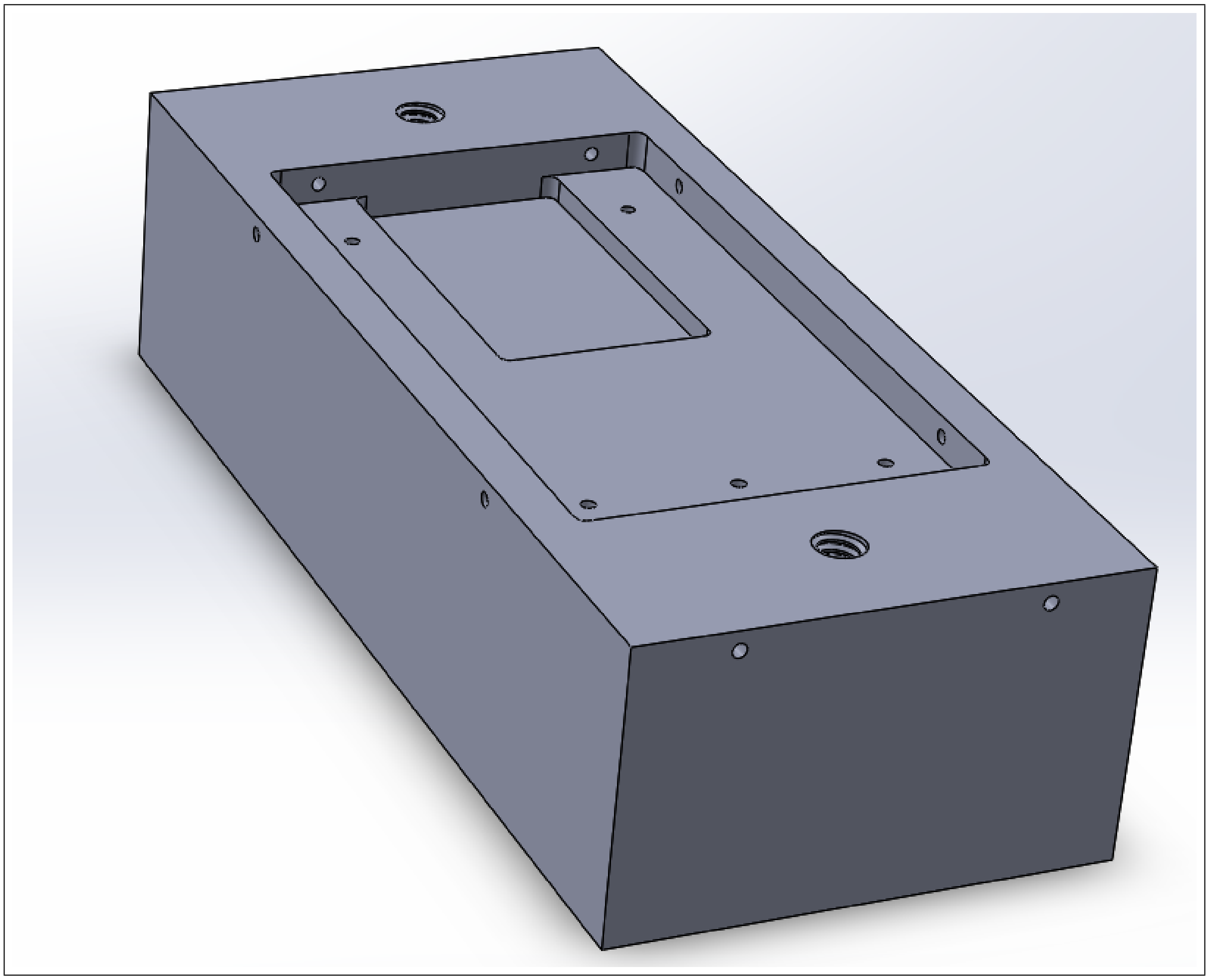

Figure 2.6: Model of resonator mount. The small holes in the walls and bottom of the mount hold ball bearings, which prevent the fused silica from contacting the aluminum mount. The larger holes are threaded to place a lid over the resonator. This mount also secures the resonator so that it can measure in the vertical orientation.

losses of aluminum are on the order of 1×10^{-2} [46]. Therefore, we can safely expect the losses from the mounting apparatus to be several orders of magnitude lower than the losses from the flexures, meaning that anchor losses are not the dominant loss mechanism in our current setup.

2.4.4 Optimization of flexure dimensions

In addition to calculating the mechanical quality factor, Equation 2.5 allows us to compute the flexure dimensions that optimize the resonator sensitivity. By noting that the mechanical quality factor of a resonator is related to the loss coefficient by:

$$Q = \frac{1}{\phi(\omega_0)}, \tag{2.11}$$

we evaluate Equations 2.5, 2.6, 2.7, and 2.9 for a given resonance and range of flexure thicknesses. In doing so, we determine the quality factor as a function of the flexure dimensions. We then optimize the dimensions by finding the thickness and length combination that produces the desired resonance with the largest mQ/ω value, ensuring that the optimized dimensions produce the lowest acceleration noise floor possible. The optimization of a $3.8\,\mathrm{Hz}$, $2.2\,\mathrm{g}$ test mass is depicted in Figure 2.7. We see that there is a local mQ/ω_0 maximum when the flexure thickness is approximately $t = 83\,\mu\mathrm{m}$. At this thickness, $mQ/\omega_0 = 3.9 \times 10^2\,\mathrm{kg \cdot s}$ and $Q \approx 4.2 \times 10^6$. Such a resonator would have a thermal noise floor of approximately $1.0 \times 10^{-11}\,\mathrm{m/s^2/\sqrt{Hz}}$. In principle, we can potentially achieve even larger mQ/ω_0-values for thicker (>$1\,\mathrm{mm}$ as opposed to $0.1\,\mathrm{mm}$) flexures; however, the flexure length in such a resonator would be much larger for the same resonant frequency. For instance, COMSOL simulations suggest that $1\,\mathrm{mm}$ thick flexures would need to be >$0.5\,\mathrm{m}$ long to retain a resonance of $3.8\,\mathrm{Hz}$. Such long flexures do not follow our development goals of compact and portable optomechanical inertial sensors.

Note that the theoretical basis for this optimization is laid out in Section 2.2, and can be applied to other topologies with a test mass supported by flexures or fibers with uniform thickness. Other topologies are not considered in this optimization because the relevant topology is highly dependent on application. Parallelogram optomechanical oscillators have demonstrated excellent performance as accelerometers [37, 22] and force sensors [19]. The analysis of mechanical losses presented here for thin flexures, has been done for other topologies, including a drum-head resonator to be used for atom interferometry [2].

The width of the flexures was not considered in this optimization, due to the following: a) increasing the width can make the test mass significantly larger, lowering the thermal acceleration and displacement noise; and b) decreasing the width decreases the size of the test mass, but also lowers the frequency of higher order resonator modes.

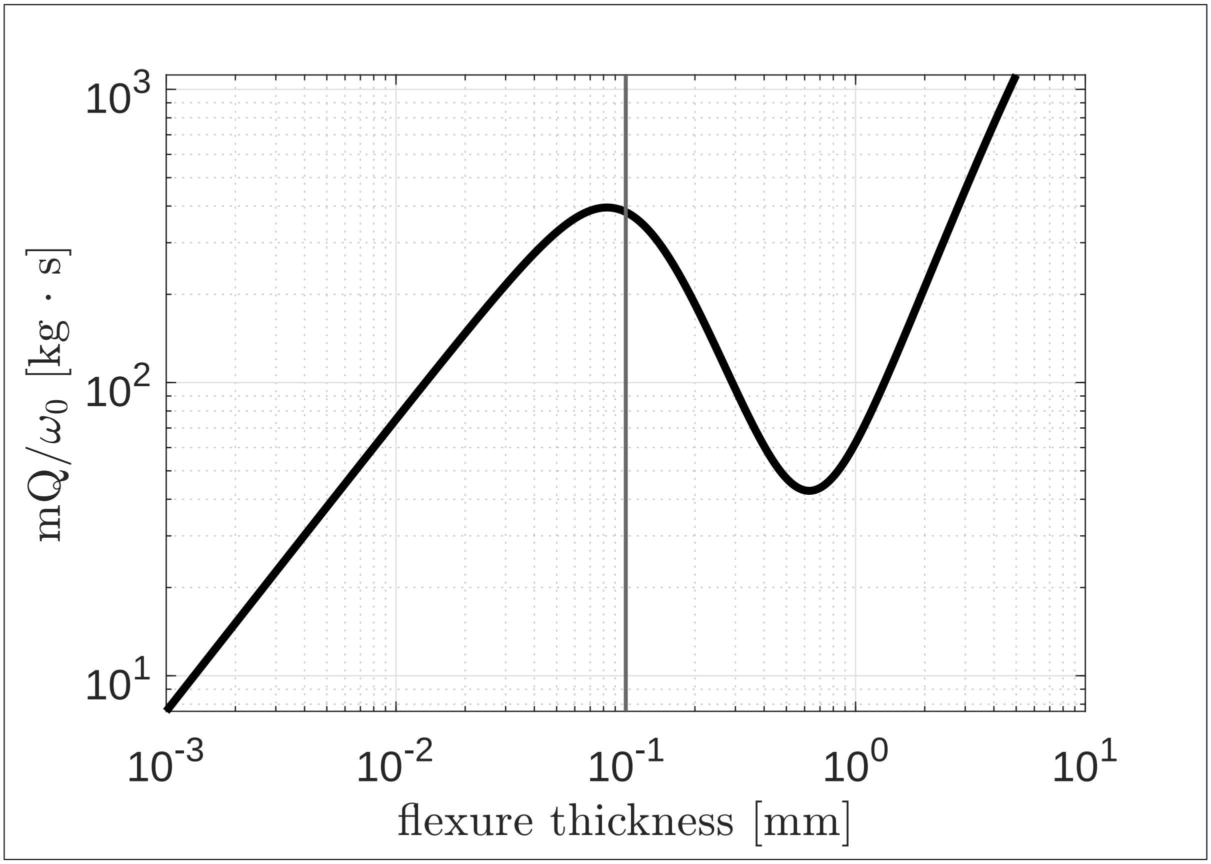

Figure 2.7: An optimization model of mQ/ω_0 for various flexure thicknesses of a $3.8\,\mathrm{Hz}$ resonator. In this simulation, the resonant frequency is held constant. When varying the thickness of the flexures' smallest dimension, we assume the length of the flexures also vary to keep the resonance constant. We evaluated the surface, bulk, and thermoelastic loss models for a range of flexure thicknesses. The local maximum around $8.3 \times 10^{-2}\,\mathrm{mm}$ indicates the optimum flexure thickness which yields the lowest noise floor. For comparison, our current resonator has $0.1\,\mathrm{mm}$ flexures, denoted by a vertical line in the plot.

2.5 Test Mass Displacement Interferometer

In order to verify these models, we need a method for detecting test mass displacement. In this section, we outline the construction of a test read-out system for this purpose. However, this interferometer is used to characterize the resonance and quality factor of the mechanical resonator and is not developed to achieve high sensitivities. In the future, the resonator will be fully integrated with a high-sensitivity displacement readout interferometer [40] to create the final optomechanical sensor. When conducting measurements on our sensor in a laboratory environment, we can expect test mass displacements well over several microns. We therefore require an interferometric readout method that provides a sufficiently large dynamic range and allows for high displacement sensitivity in future developments. To this end, we built a heterodyne laser interferometer (Figure 2.8), which is capable of measuring displacements significantly larger than an interferometer fringe to characterize the mechanical resonator and directly measure its resonant frequency and Q. In order to enable the deployment of these sensor in the field, adequate test mass stoppers that constrain the test mass displacement range should and can easily and monolithically integrated into the future sensor fabrication approach.

To track test mass displacement, we placed an external mirror on top of the test mass and mounted a second mirror on the frame of the resonator to provide an interferometric reference phase that allows for differential measurements. Except for the mirrors reflecting their respective signal arms, the two interferometers share many optical components to facilitate common-mode noise rejection. To reduce gas damping, we placed the optomechanical resonator into a low-pressure chamber that reaches $0.9\,\mathrm{mTorr}$. This chamber contains a viewport for optical access to the two mirrors placed on the resonator. This interferometer is operated in air outside the chamber, except for the mirrors placed onto the resonator.

2.6 Experimental results

From the interferometers described above, we were able to perform preliminary tests of the COMSOL models. We measured the quality factor of the resonator from ringdown measurements,

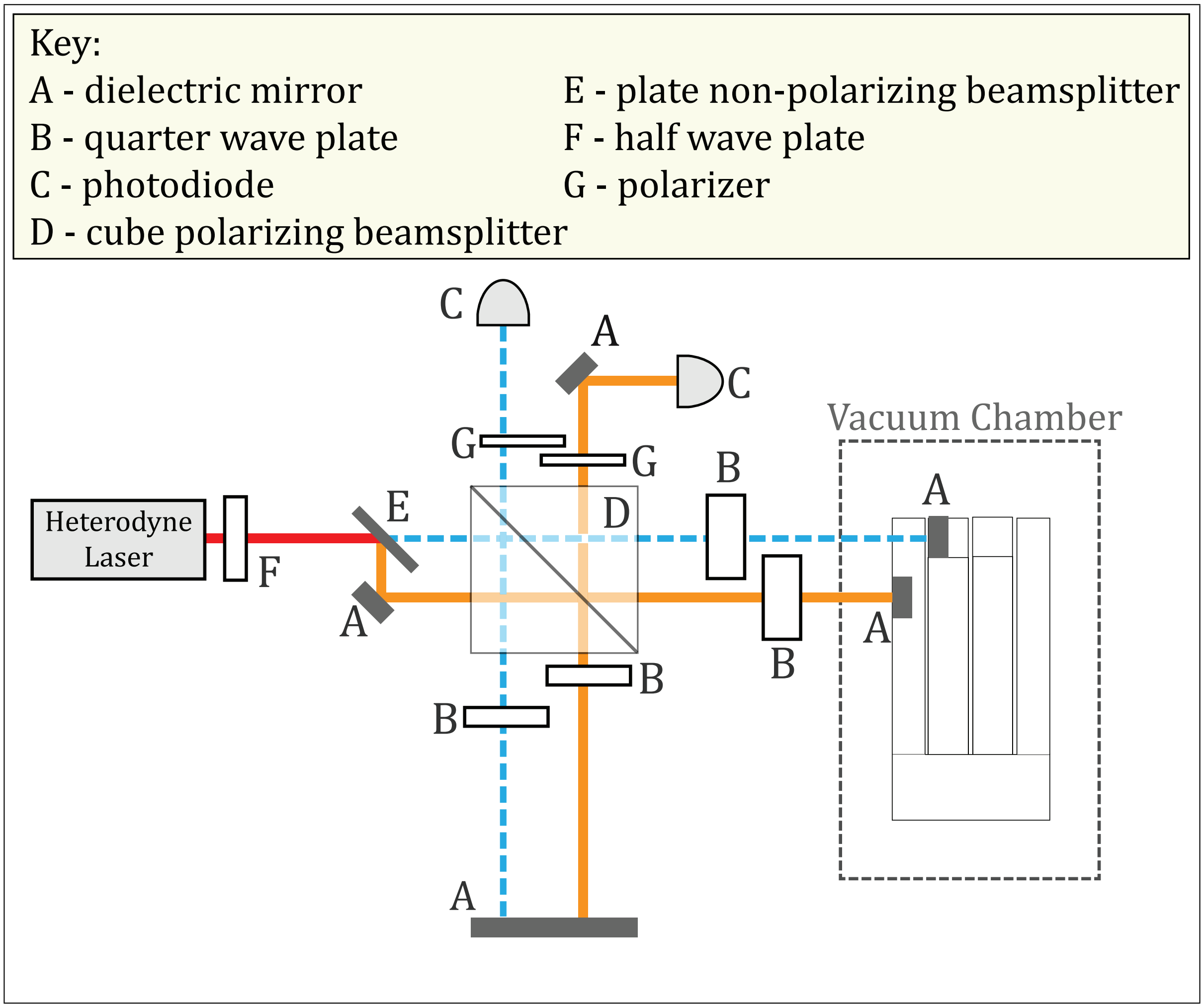

Figure 2.8: Diagram of the interferometers used to measure acceleration and displacement power spectral densities. A heterodyne laser beam consisting of two frequencies is split in two by a non-polarizing beam splitter. The light is equally split between the two interferometers, measurement and reference. The signal arm of measurement interferometer reflects off of the mirror placed on the test mass. The signal arm of the reference arm reflects off a mirror placed on the frame of the resonator. The reference arm of both interferometers reflect off a common mirror. The displacement of the test mass is measured by subtracting the phases of the two interferometers. Using two interferometers allows for the rejection of common-mode noise, lowering the total readout noise.

which analyze the decay envelope of the maximum test mass displacement over time.

Ringdown measurements at atmospheric pressure yielded quality factors of $Q = 600 - 700$, in good agreement with the COMSOL simulations. We then pumped the vacuum chamber down to $0.9\,\mathrm{mTorr}$ and recorded a ringdown of the resonator over one hour. The decay envelope, shown in Figure 2.9, yields a mechanical quality factor of $Q = 1.14 \times 10^5$. This corresponds to an mQ-product of $250\,\mathrm{kg}$ and a thermal noise floor of $a_{\mathrm{th}} = 4.03 \times 10^{-11}\,\mathrm{m/s^2/\sqrt{Hz}}$ at higher frequencies, increasing with a slope of $1/f$ towards low frequencies. In our current experimental setup, we use a heterodyne laser interferometer of limited sensitivity with the purpose of characterizing the mechanical properties of our resonator. This is not intended to directly observe the acceleration noise floor of the device. To this end, an isolated platform such as a torsion balance or similar may be needed to effectively access acceleration noise floors at $1 \times 10^{-11}\,\mathrm{m/s^2/\sqrt{Hz}}$. However, we anticipate that the thermal noise can be resolved when the resonator is coupled to a high-precision laser interferometer [40] and operated on a platform with appropriate seismic isolation.

When studying and measuring the quality factor, we observed that there is a strong dependence on pressure, even when pumping down to the mTorr regime, which is expected. This behavior suggests that Q is still limited by gas damping. Figure 2.10 shows the quality factors we have observed versus pressure. Gas damping losses limit the quality factor of the resonator at this pressure regime to a so-called ballistic regime that can be determined by [47]:

$$Q_{gas} = \frac{a}{P}, \tag{2.12}$$

where a is a parameter dependent on temperature and the properties of the gas. The reciprocals of quality factors add linearly:

$$\frac{1}{Q} = \frac{1}{Q_{gas}} + \frac{1}{Q_0}, \tag{2.13}$$

where Q_0 is the quality factor due to other loss mechanisms. By fitting the data in Figure 2.10 we obtain that $a = 205\,\mathrm{Torr}$ and $Q_0 = 2.17 \times 10^5$. The Q vs. pressure data points on the plot clearly follow a trend in agreement with gas damping, indicating that this the current dominant

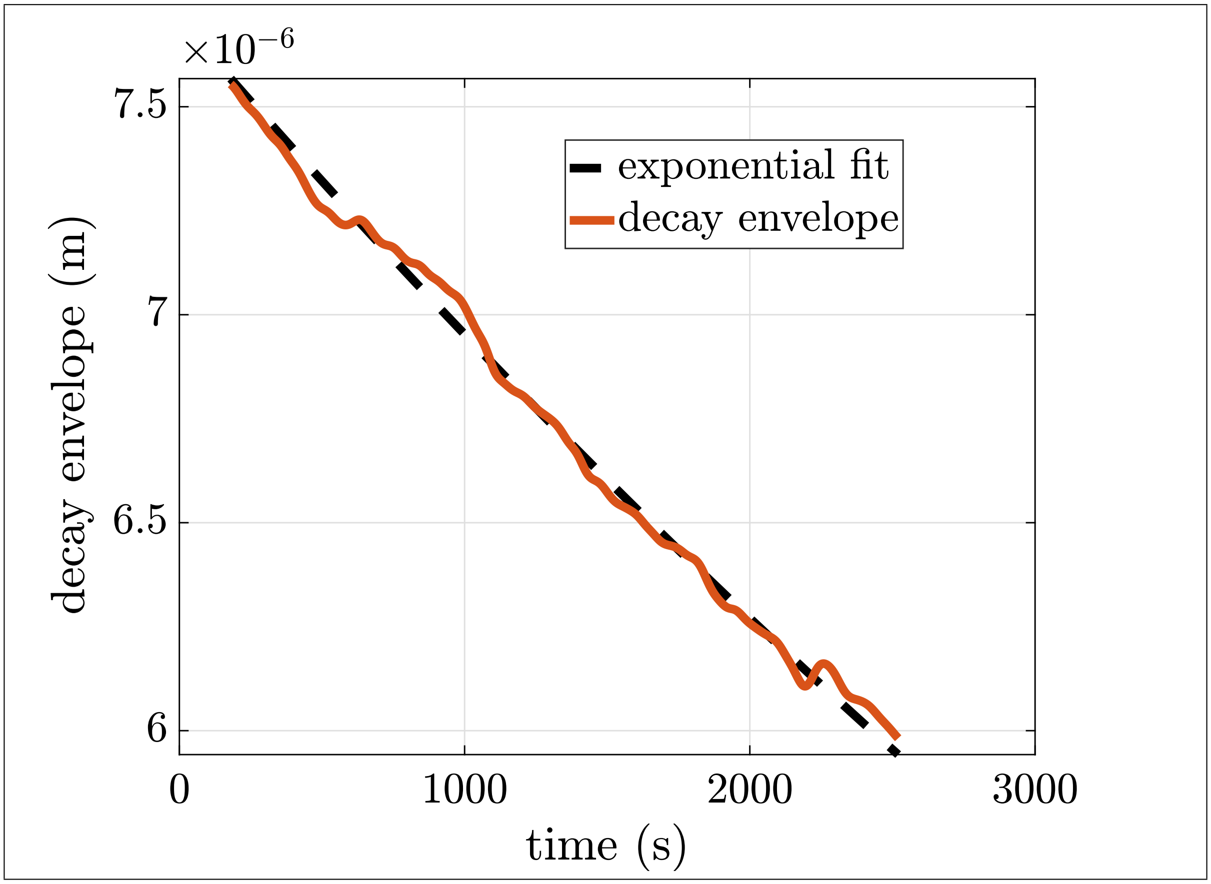

Figure 2.9: Decay envelope of the test mass oscillations during a ringdown. Fitting to an exponential decay, we find $Q = 1.14 \times 10^5$. This fit has an r^2 value of 0.989.

loss mechanism in our system for pressures at the mTorr level.

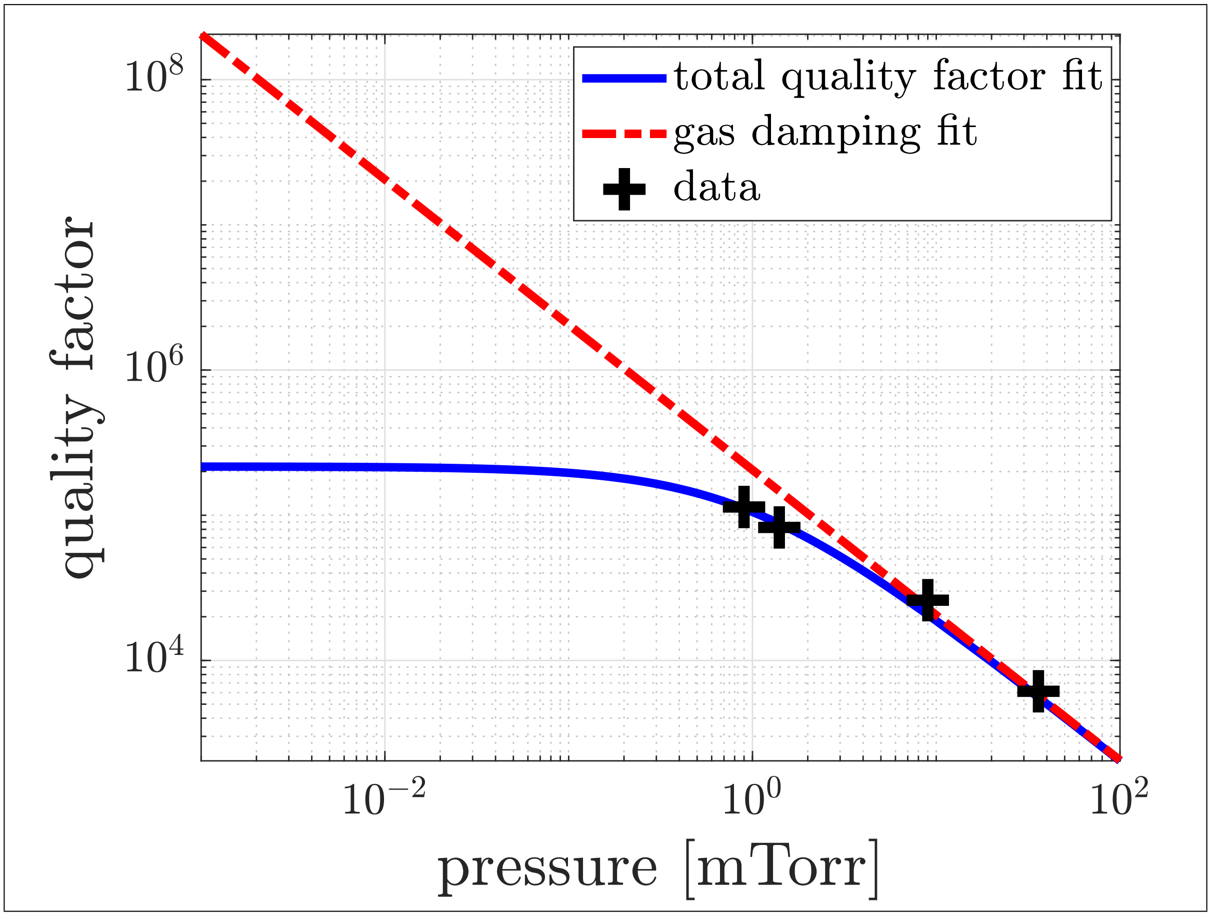

Figure 2.10: Quality factors obtained from ring-downs are plotted versus the pressure in the vacuum chamber. From the fit, we infer that the quality factor of the resonator in our test setup is limited by gas damping at the pressures we can achieve.

2.7 Outlook

In this work, we modeled the energy loss mechanisms limiting the sensitivity of a novel 10 Hz optomechanical inertial sensor. In contrast to previous work in optomechanical accelerometers over kHz frequencies [22], the low-frequency resonance of this sensor allows for better sensing of low-frequency signals. Using two heterodyne interferometers as displacement sensors, we presented preliminary measurements of the resonator's quality factor at various pressure levels. Improvements to our low-pressure and vacuum facilities are currently under commissioning, and we expect that these improvements will lead to significantly lower gas damping losses, laser-interferometric displacement and acceleration noise floors in our optomechanical inertial sensors. We have demonstrated that our mechanical resonator can achieve a mQ-product of $250\,\mathrm{kg}$ under our current experiment conditions, leading to acceleration noise floors at levels of $4 \times 10^{-11}\,\mathrm{m/s^2/\sqrt{Hz}}$ for frequencies above resonance. However, we anticipate to achieve higher mQ-products as we improve our vacuum systems.

These investigations show that our sensor's compact dimensions, magnetic field insensitivity, and high mechanical quality factor make low-frequency optomechanical inertial sensors promising candidates for field high sensitivity acceleration measurements.

3. RESONATOR TOPOLOGY OPTIMIZATION

The work presented in Chapter 2 highlighted a significant drawback to our first resonator design: the inability to integrate the optical readout onto the wafer of the resonator. In addition to the surface area of the wafer being insufficient to hold a laser interferometer, the test mass could only be tracked by placing a mirror on top of the test mass. If rotated vertically, the lever arm of the mirror changes the mechanics of the test mass' rectilinear motion, potentially introducing significant acceleration noise through the tilting of the test mass. To ensure our optomechanical accelerometer can operate along any axis, we desire want the test mass mirror to be flush with the surface of the test mass, which required a redesign of the resonator.

Redesigning the resonator so it can appropriately hold optical hardware is straightforward, requiring only a larger wafer and a test mass cutout which can house a mirror. However, designing a new resonator allows us to leverage the models developed in Chapter 2 to optimize the performance of our optomechanical accelerometer. In this chapter, we detail this optimization process that we utilized to design novel fused silica resonators.

Recall that this project targets the sub-Hz regime as its acceleration detection bandwidth. We therefore require a mechanical resonator whose stiffness is conducive to the detection of such low-frequency signals. In Chapter 2, we derive the transfer function of external accelerations to test mass motion, as demonstrated in Equation 2.3. The magnitude of this transfer function, plotted in Figure 3.1, informs us how the test mass responds to vibrations at different frequencies. Above the resonant frequency of the test mass, vibrations couple into the resonator motion with an efficiency of $1/\omega^2$. Below resonance, that coupling efficiency approaches $1/\omega_0^2$. Therefore, for any desired detection bandwidth the frequency of the mechanical resonator should be just larger than the highest-frequency signal you want to measure. A higher frequency resonator would diminish the sensitivity to the desired signals whereas a lower frequency resonator would leave the resonant peak of the test mass in the bandwidth of interest, obscuring a portion of the signal. In the case of a sub-Hz detection bandwidth, it is therefore appropriate to use a mechanical resonator with a

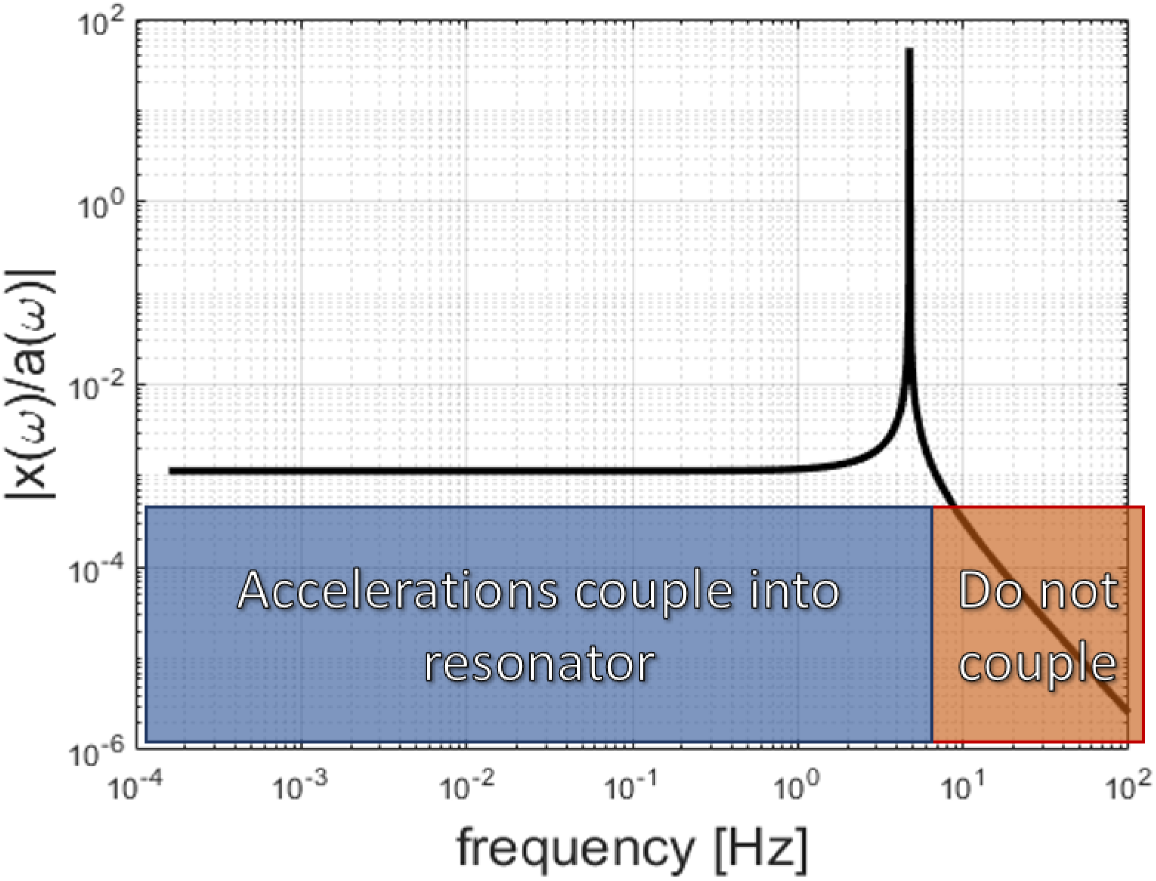

Figure 3.1: The transfer function of external acceleration to test mass displacement. Above the resonant frequency of the test mass, vibrations do not strongly couple into the test mass motion. Below resonance, vibrations are imprinted into the test mass oscillations with a coupling factor of approximately $1/\omega_0^2$. This plot informs us what resonant frequency is appropriate for detection of noise in the sub-Hz regime.

frequency on the order of $1\,\mathrm{Hz}$, and for the remainder of this chapter we select a target resonance of $5\,\mathrm{Hz}$.

As the resonator oscillates, it gives up energy to various mechanical loss mechanisms. The energy dissipated creates thermal motion in the flexures which in turn contributes to the acceleration noise floor of the accelerometer it constitutes. These loss mechanisms can be categorized into external and internal losses based on the cause of the energy dissipation and way the mechanism is mathematically modeled. External losses primarily include gas damping, modeled as a velocity-damping term in the equation of motion of the test mass. Internal losses on the other hand are modeled as a complex spring constant and are comprised of mechanisms that happen through the material of the resonator. Both damping categories depend on the material choice and topology of the resonator, however gas damping is mitigated by operating in a vacuum. Internal losses cannot be muted by changing the testing environment. Because of this, it is natural to optimize the topology of our resonator to minimize the internal energy dissipation. These mechanisms include losses through the bulk material, through the surface of the material, and through temperature fluctuation-induced bending. Equations for the bulk [44], surface [45], and thermoelastic [38, 39] losses that happen within the fused silica resonator are given by:

$$\phi_{bulk}(\omega) = 0.76 \times 10^{-10} \times (\frac{\omega}{2\pi})^{0.77} \tag{3.1}$$

$$\phi_{surface} = \frac{3+a}{1+a}(6.15\,\mathrm{pm})\frac{2(w+t)}{wt} \tag{3.2}$$

$$\phi_{te}(\omega) = \frac{YT\alpha^2}{\rho C}\frac{\omega\tau}{1+\omega^2\tau^2} \tag{3.3}$$

where w and t are the dimensions of the cross-section for a rectangular flexure, a is the aspect ratio of that cross-section, Y is Young's Modulus, T is temperature, α is the coefficient of thermal expansion, ρ is the mass density, and C is the specific heat capacity. Furthermore, τ is the characteristic time for heat to flow from one side of the flexure to the other, given by [38]:

$$\tau = \frac{\rho C w^2}{\pi^2 \kappa} \tag{3.4}$$

where w is the flexure width and κ is the thermal conductivity. The total mechanical loss coefficient for the resonator is simply the sum of Equations 3.1-3.3:

$$\phi(\omega) = \phi_{bulk}(\omega) + \phi_{surface} + \phi_{te}(\omega) \tag{3.5}$$

Note that surface and thermoelastic losses both depend on the flexure dimensions, suggesting that it is possible to minimize these energy dissipation mechanisms by carefully selecting the flexures' width and thickness. As demonstrated in Section 4.1.2, thermal acceleration noise goes like the square root of the loss coefficient and so lowering the losses in the resonator will lower the thermal noise floor. However, we must also ensure the flexure size allows us to meet our other design constraints. We summarize the objectives of our topology optimization below:

- Minimize the mechanical losses.
- Maximize the test mass.
- Achieve the target resonant frequency.
- Have higher-order modes have frequencies $10\times$ larger than the
- Maintain a compact resonator footprint of approximately $100\times100\,\mathrm{mm}$.
- Prevent the flexures from snapping under typical handling and operating conditions.

These objectives are evidently in competition. Rather than a formal optimization, we utilize models and simulations to gain sufficient insight to make informed design choices. In Equations 3.2 and 3.4, t is the thickness of the flexure and is identical to the thickness of the wafer from which the resonator is etched. The flexure width w represents the shorter dimension of the flexure cross-section that allows the resonator to oscillate. The test mass is first maximized by selecting the thickest wafer that can be etched, t=6.6 mm in the case of fused silica. As a starting point for our calculations, we also assume the test mass is $15\,\mathrm{mm}$ wide × $12\,\mathrm{mm}$ tall for a total mass of $2.6\,\mathrm{g}$. With this value of t and a predetermined target resonance of $\omega_0 = 2\pi \times 5\,\mathrm{Hz}$, Equations 3.1-3.5 are used to find an optimal width w that minimizes the mechanical losses. Because the loss coefficient is frequency dependent, we chose to optimize the losses at $\omega = \omega_0$. Specifically, by inspecting Equation 2.4 we select the quantity $\frac{mQ}{\omega_0^2}$ to be optimized because Q contains the desired loss coefficient and scaling by $\frac{m}{\omega_0^2}$ readily allows for comparing the thermal noise in resonators with different topologies, test masses, and resonant frequencies. Evaluating this quantity for a range of flexure widths produces the plot in Figure 3.2.

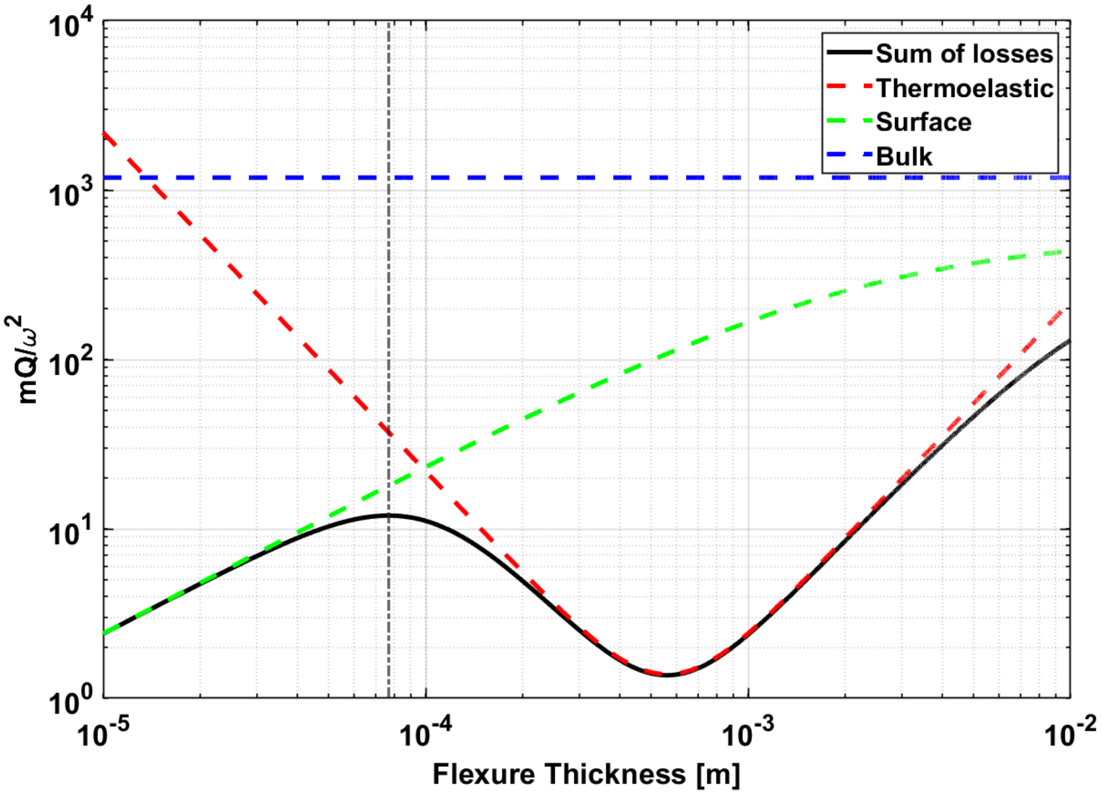

Figure 3.2: The optimization curve of our $5\,\mathrm{Hz}$ resonator as a function of flexure width as well as the contributions from bulk, surface, and thermoelastic losses. Maximizing $\frac{mQ}{\omega_0^2}$ results in lower thermal acceleration noise. The grey vertical line indicates the calculated optimum flexure size.

We find that a $2.6\,\mathrm{g}$ fused silica resonator with a natural mode of $5\,\mathrm{Hz}$ has a local maximum of $10.4\,\mathrm{kgs}^2$ in the optimization parameter at w=$75\,\mathrm{\mu m}$, but higher values can be achieved by increasing the flexure width to several millimeters or thicker. However, in performing this exercise, there is an implicit assumption that when changing the flexure width, the flexure length is also modified in order to keep the resonant frequency constant. Using COMSOL's Solid Mechanics module, we find that without changing the size of the $2.6\,\mathrm{g}$ test mass, $1\,\mathrm{mm}$ wide flexures would need to be approximately $480\,\mathrm{mm}$ long to keep the resonant frequency at $5\,\mathrm{Hz}$, $5\times$ larger than the size constraint previously defined. Furthermore, the out-of-plane motion of the test mass for a resonator this size would have a resonant frequency under $20\,\mathrm{Hz}$, going against the constraint imposed on higher-order modes. In principle, the frequency of the out-of-plane motion could be increased by making the flexures and test mass thicker. However, this solution is not practical as we have already chosen the maximum fused silica wafer thickness that can reliably be etched. Because of these issues, we instead chose a flexure width near the local maximum at $75\,\mathrm{\mu m}$.

Yet, smaller flexures encounter the problem of having too much stress in them under normal loads. The bending strength of fused silica samples is known to be $67\,\mathrm{MPa}$ [48]. Our COMSOL simulations suggest that a $2.6\,\mathrm{g}$ test mass with $53 \times 0.075 \times\ 6.6\,\mathrm{mm}$ flexures would have a resonant frequency of $5.1\,\mathrm{Hz}$, but the stress in the device when gravity is pointed along the axis of test mass motion would be as high as $50\,\mathrm{MPa}$. While still 25% under the bending strength of the material, this design would not afford much room for error while handling the device and is not ideal for our purposes.

Instead, we choose a width of w =$100\,\mathrm{\mu m}$ which has been previously demonstrated in past resonator designs [23]. The maximum stress in the flexures in this scenario is estimated to be $35\,\mathrm{MPa}$ when gravity is along the axis of the test mass motion, which is comfortably below the material bending strength. Table 3.1 summarizes our the different flexure widths we simulated to identify the optimum design for our resonator. The different simulated resonators are also visualized in Figure 3.3. The final redesign of the resonator is presented in the next chapter.

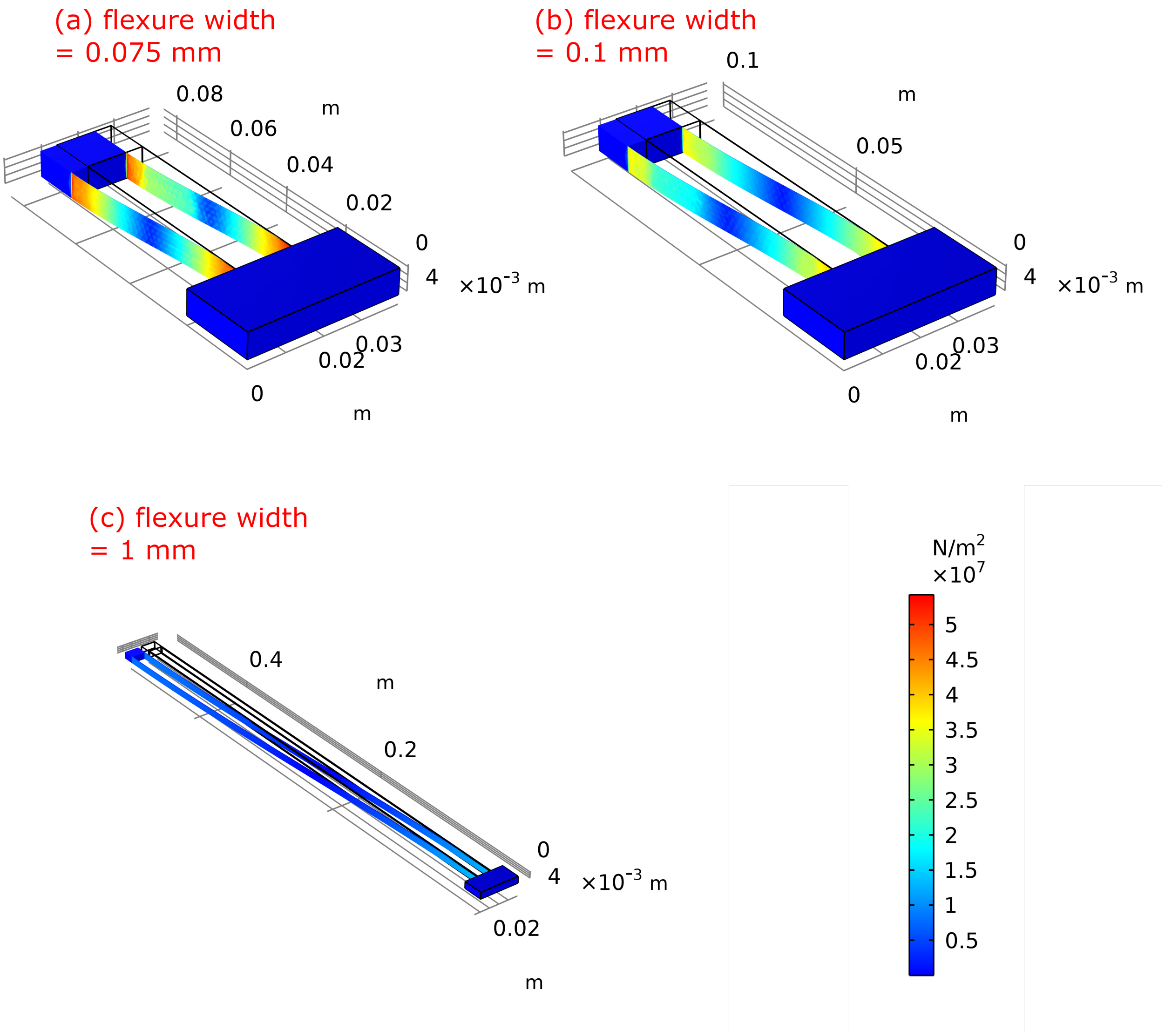
(a) flexure width = 0.075 mm

(b) flexure width = 0.1 mm

(c) flexure width = 1 mm

Figure 3.3: A comparison of fused silica resonators with different flexure widths. Color indicates the Von Mises stress with the flexures under a $1\,\mathrm{g}$ acceleration along the axis of the resonator's natural frequency. All three designs have resonance frequency of approximately $5\,\mathrm{Hz}$. We observe that thinner flexures, while more compact, experience greater stresses which make them more likely to break. Wider flexures experience the least amount of stress, but must be much longer to maintain a low resonance.

width	length	stress	higher-order frequency
75 µm	53 mm	50 MPa	163 Hz
100 µm	68 mm	35 MPa	130 Hz
1 mm	480 mm	13 MPa	19 Hz

Table 3.1: A table summarizing our simulations of resonators with different flexure widths. The flexure length is the length needed to create a resonant frequency of approximately 5 Hz, the stress is the maximum von Mises stress in the flexures when gravity is pointed in the plane of motion, and the higher-order frequency is the frequency is the second-lowest mode. This data is used to evaluate what size ribbon allows the resonator to meet our experimental constraints.

4. SECOND ITERATION LOW-FREQUENCY OPTOMECHANICAL ACCELEROMETER*

The topology optimization work presented in Chapter 3 resulted in a new resonator design for our optomechanical accelerometer. This design featured a thicker wafer and larger test mass, which is anticipated to exhibit lower thermal motion and produce a more sensitive accelerometer. Moreover, the design is novel in that it has cutouts on the wafer and test mass, intended to hold optical hardware for laser interferometric displacement readout. Integrating the readout scheme onto the fused silica resonator is advantageous because it results in a more compact accelerometer, which is lighter, more portable, and less susceptible to noise originating from thermal expansion. At the time of fabricating this new resonator, the compact laser interferometer was not ready to be bonded to the wafer. Rather, the first task carried out with this design was to characterize its resonant frequency and mechanical quality factor, and to demonstrate its ability to detect seismic motion. Furthermore, preliminary measurements allow us to identify several noise sources that limit our sensitivity below $100\,\mathrm{mHz}$ and estimate the temperature stability and laser frequency stability requirements to achieve a thermally-limited acceleration measurement. This chapter, based on the 2022 Remote Sensing article [7], discusses our work to characterize this new resonator. The work presented in this chapter was done in collaboration with Dr. Felipe Guzmán, Dr. Guillermo Valdes, Dr. Jose Sanjuan, Dr. Yanqi Zhang, Andrea Nelson, and Jeremiah Stoddart who all contributed to the experimental design and analysis. In particular, Dr. Yanqi Zhang aided in the development of our heterodyne laser interferometer and Dr. Jose Sanjuan provided valuable insight regarding data correction techniques. My contributions to this work include the construction of the experimental setup, the design of the fused silica resonator, data collection and analysis, and writing an article for journal publication.

We present a novel optomechanical inertial sensor for low-frequency applications and corresponding acceleration measurements. This sensor has a resonant frequency of $(4.715 \pm 0.001)\,\mathrm{Hz}$,

---

[*] Reprinted with permission from “Optomechanical Accelerometers for Geodesy” by Adam Hines, Andrea Nelson, Yanqi Zhang, Guillermo Valdes, Jose Sanjuan, Jeremiah Stoddart and Felipe Guzmán, 2022. Remote Sensing, Vol. 14, Copyright 2022 by MDPI.

a mechanical quality factor of $(4.76 \pm 0.03) \times 10^5$, a test mass of $2.6\,\mathrm{g}$, and a projected noise floor of approximately $5 \times 10^{-11}\,\mathrm{ms^{-2}}/\sqrt{\mathrm{Hz}}$ at $1\,\mathrm{Hz}$. Such performance, together with its small size, low weight, reduced power consumption, and low susceptibility to environmental variables such as magnetic field or drag conditions makes it an attractive technology for future space geodesy missions. In this chapter, we present an experimental demonstration of low-frequency ground seismic noise detection by direct comparison with a commercial seismometer, and data analysis algorithms for identification, characterization and correction of several noise sources.

4.1 Methods

4.1.1 Optomechanical accelerometers

Our optomechanical accelerometer is composed of two main components: the mechanical resonator and the laser interferometric readout. In this section we discuss the design of both parts and present characterization measurements which can be used to project the acceleration noise floor of our device.

4.1.1.1 Resonator - design and characterization

We have designed a resonator intended to be used for 1D acceleration measurements, though a triaxial device would be a straightforward extension of the topology presented here. This resonator is laser-assisted dry-etched from a single monolithic fused silica wafer and is $90\,\mathrm{mm} \times 80\,\mathrm{mm} \times 6.6\,\mathrm{mm}$ in volume with a total mass of $58.2\,\mathrm{g}$. Our accelerometer has a smaller form and lighter weight than the GRACE-FO accelerometer, representing a major advantage for satellite missions. An image of our resonator is shown in Figure 4.1. Our design consists of a $2.6\,\mathrm{g}$ parallelogram test mass supported by two $100\,\mathrm{\mu m}$ thick leaf-spring flexures.

Finite Element Analysis (FEA) simulations performed in COMSOL predict a $5.5\,\mathrm{Hz}$ resonant frequency, which makes our resonator suitable for measuring non-inertial disturbances below $1\,\mathrm{Hz}$. At frequencies below resonance, the test mass response x to an external acceleration a is approximately given by:

$$x \approx \frac{a}{\omega_0^2} \tag{4.1}$$

Figure 4.1: A diagram of our $5\,\mathrm{Hz}$ resonator. A penny is added for reference.

where ω_0 is the angular resonant frequency. There is a trade-off between the required displacement sensitivity, how low the resonance can be in a practical resonator, and its final dimensions. Therefore, a resonance on the order of $1\,\mathrm{Hz}$ allows this low-frequency noise to couple into the test mass motion better than a high resonance device, which in turn relaxes the required test mass readout precision. Conversely, a lower resonance device requires a larger resonator, which quickly becomes more difficult to work due to the low-stiffness.

Furthermore, our simulations predict that all higher-order modes have frequencies above $130\,\mathrm{Hz}$, significantly higher than the lowest resonance by a over an order of magnitude. This is desired for mitigating the cross-talk between modes that appears in our measurements, which in turn reduces the noise in our data. Figure 4.2 shows the first two modes of this resonator: the first being the translational mode of the test mass and the second being a violin mode of the flexures with a significantly higher frequency.

The acceleration experienced by the resonator is recovered by applying a transfer function,

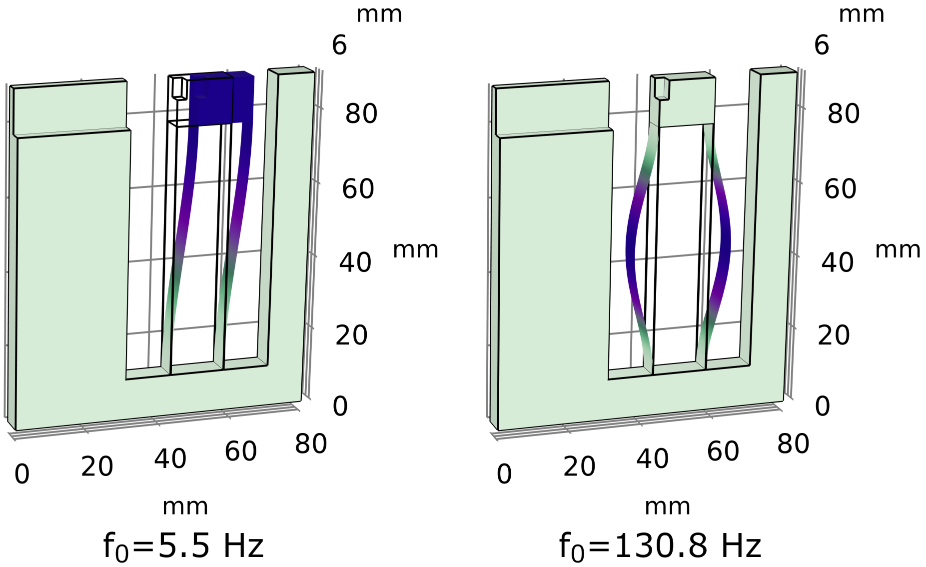

Figure 4.2: The first two eigenmodes of our $5\,\mathrm{Hz}$ resonator modeled in COMSOL. Note that the second mode is larger than the first by more than a factor of 10. Having higher order modes that are substantially higher than the first mode is desired for minimizing the cross-talk between modes observed in measurements.

which is defined by the resonance and quality factor, to the test mass displacement data. This transfer function is given by [23]:

$$\frac{\tilde{x}(\omega)}{\tilde{a}(\omega)} = \frac{-1}{\omega_0^2 - \omega^2 + i\omega_0\omega/Q} \tag{4.2}$$

where $\tilde{x}(\omega)$ is the test mass motion, $\tilde{a}(\omega)$ is the acceleration coupling into the resonator, ω_0 is the resonant frequency, and Q is the mechanical quality factor. Note that when $\omega << \omega_0$, Equation 4.2 simplifies to Equation 4.1. To characterize the acceleration sensing capabilities of our resonator, we experimentally determine these parameters using a ringdown test where we deliberately excite the test mass motion and track its oscillations. In the absence of other perturbations, the oscillation amplitude will exponentially decay, allowing for an easy calculation of Q. Figure 4.3 depicts the decay envelope of our ringdown measurement, which was performed over 14 hours at a vacuum pressure of $10\,\mu\mathrm{Torr}$. From this measurement we find a Q-factor of $(4.76 \pm 0.03) \times 10^5$ and an mQ-product larger than $1250\,\mathrm{kg}$. Furthermore, taking the Fast Fourier Transform (FFT) of the raw data yields a resonant frequency of $f_0 = (4.715 \pm 0.001)\,\mathrm{Hz}$, in good agreement with our simulated value of $5.5\,\mathrm{Hz}$. The transfer function in Equation 4.2 can then be evaluated using our experimentally determined parameters. We apply this transfer function to the displacement measurements in the frequency domain to convert the signal to acceleration noise.

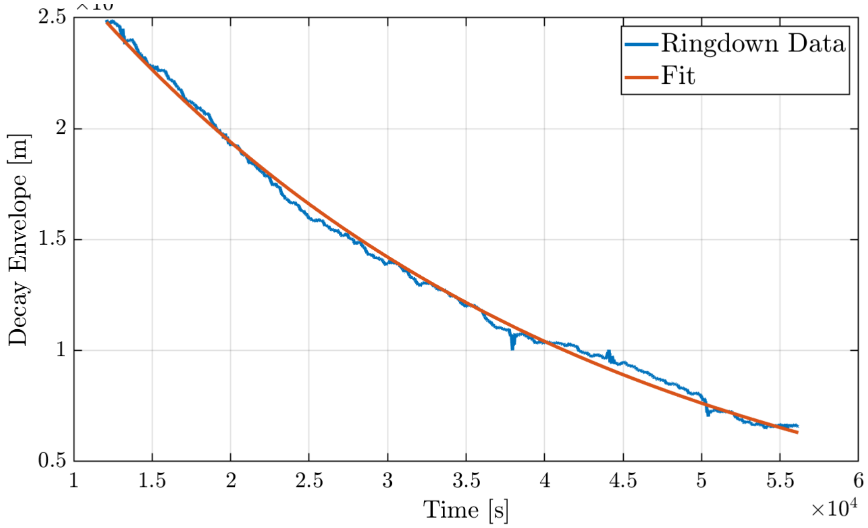

Figure 4.3: Decay envelope of our ringdown measurement fitted to an exponential. The resonant frequency is removed with a low-pass filter, allowing us to calculate the Q-factor to be $(4.76 \pm 0.03) \times 10^5$.

4.1.1.2 Laser interferometer - design and characterization

In order to measure the local acceleration noise we must measure the displacement of the test mass from its equilibrium. For this, we constructed a heterodyne displacement interferometer with a differential phase readout. Cutouts on the test mass and the u-shaped frame of our resonator, shown in Figure 4.1, allow for easy implementation of mirrors that complete this laser interferometer. The optical methods and noise rejection schemes used for this readout are discussed in greater detail in [49], though an overview of this optical readout is provided in this section. Figure 4.4 contains a diagram of our laser interferometer. A fiber-coupled $1064.181\,\mathrm{nm}$ beam is split and frequency-shifted by two accoustic-optical modulators (AOMs) to create a $5\,\mathrm{MHz}$ heterodyne frequency. The frequency shifted beams are then injected into a series of prisms that create two distinct Mach-Zehnder type interferometers: one that tracks the test mass motion and one that acts as a reference.

The measurement interferometer sends one beam to a mirror on the test mass, M_M, where the displacement information is imprinted on the phase of the reflected beam. Similarly the reference interferometer reflects one beam off a stationary mirror, M_R. The second beams for both interferometers reflect off the same common mirror, M. Common mode noise sources, such as temperature fluctuations in the prisms, will coherently affect both interferometers. Therefore a differential phase measurement rejects some environmental noise and allows for a high-sensitivity displacement sensing.

Furthermore, the laser adds noise to our data in the form of laser frequency noise. To combat this we also introduce a delay-line interferometer to the setup. This interferometer allows us to make independent measurements of the frequency noise by interfering one beam from the laser with a delayed copy of itself. By creating a path-length difference of $2\,\mathrm{m}$ in the delay-line interferometer arms, laser frequency fluctuations becomes the dominant noise source in this fiber interferometer, although its signal-to-noise ratio (SNR) decreases toward lower frequencies due to fiber noise. With this measurement we can remove most of the laser frequency noise from the resonator data in post-processing. However, for example, in future space geodesy missions, a frequency-stabilized laser source will be available, offering enhanced stability than can be achieved through post-correction and therefore eliminating the need for a delay-line interferometer. The readout displacement noise, taken with a stationary mirror in place of the test mass mirror, is shown in Figure 4.5. We find that this interferometer can measure displacement with a sensitivity of $3 \times 10^{-12}\,\mathrm{m}/\sqrt{\mathrm{Hz}}$ at $1\,\mathrm{Hz}$ and $7 \times 10^{-10}\,\mathrm{m}/\sqrt{\mathrm{Hz}}$ at $1\,\mathrm{mHz}$. The peaks near $0.4\,\mathrm{Hz}$ and $1\,\mathrm{Hz}$ are caused by the mechanical resonances of a vibration isolation platform the interferometer was placed on while testing.

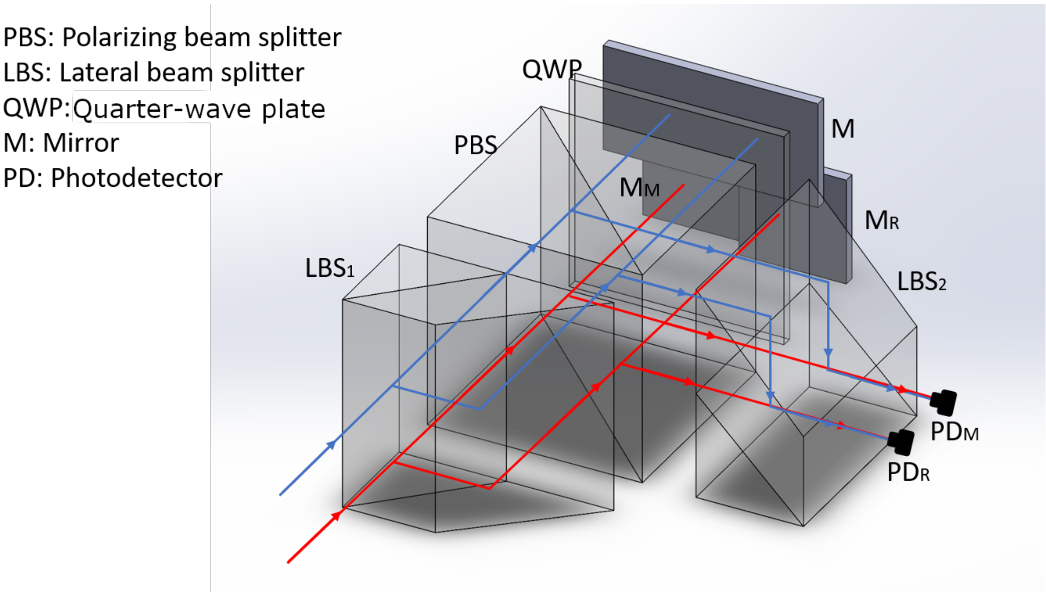

Figure 4.4: A diagram of the heterodyne readout used for our measurements. In this schematic, the mirrors M and M_R are stationary while M_M is the mirror on the test mass.

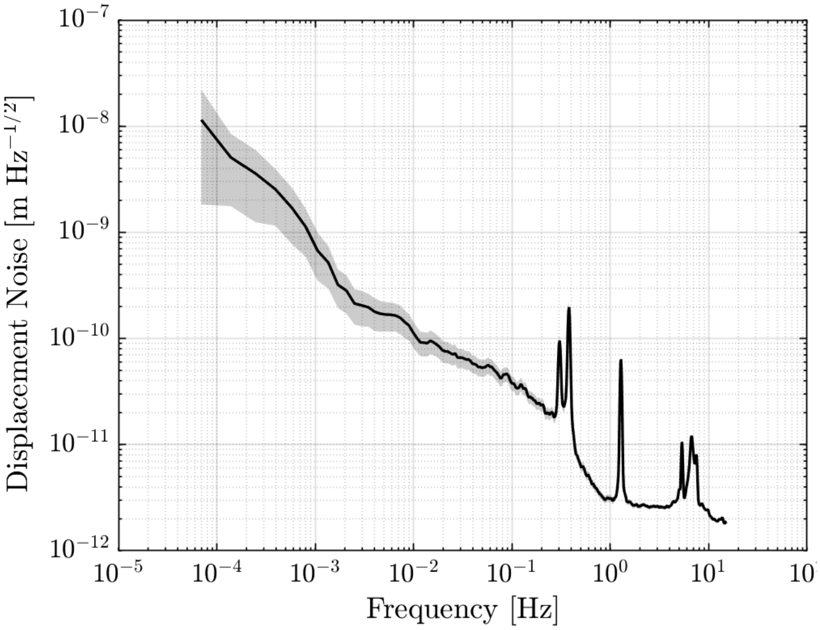

Figure 4.5: A plot of the displacement noise in our heterodyne interferometer. As this measurement was taken without our resonator, seismic noise is not present in the data. The shaded area represents the estimated error bars of the spectrum.

4.1.2 Accelerometer noise floor

The acceleration sensitivity of our optomechanical accelerometer is anticipated to be limited by both the thermal noise of the resonator and the displacement noise from the readout interferometer. In this section we estimate both contributions in order to calculate the acceleration noise floor.

Thermal noise, which represents the ultimate acceleration sensitivity that can be achieved with our resonator, is caused by gas damping and internal loss mechanisms within the fused silica. These loss mechanisms include bulk losses, surface losses, and thermoelastic losses. The thermal acceleration noise can be derived from theory starting from the equation of motion for a resonator, given by [23, 50]:

$$ma = m\ddot{x} + m\Gamma\dot{x} + m\omega_0^2(1 + i\phi(\omega))x \tag{4.3}$$

where m is the test mass, Γ is the gas damping rate, and $\phi(\omega)$ is the internal loss coefficient of our fused silica oscillator. Converting to the frequency-domain and applying the Fluctuation-Dissipation Theorem [50], we find that the thermal acceleration noise is given by:

$$\tilde{a}_{\mathrm{th}}^2(\omega) = \frac{4k_{\mathrm{B}}T}{m\omega}(\omega\Gamma + \omega_0^2\phi(\omega)) \tag{4.4}$$

where T is the temperature of the test mass and k_B is Boltzmann's constant. In general, both gas damping and internal losses contribute to the thermal noise. However, because our testing environment can reach $\mu\mathrm{Torr}$ pressures, we operate under the assumption that gas damping is negligible in comparison to internal losses. Previous work on a similar resonator estimated that the a vacuum pressure of $10\,\mu\mathrm{Torr}$ would be sufficient for making gas damping negligible compared to other mechanical losses, which is achieved both in laboratory environments, portable vacuum enclosures, and certainly space geodesy missions. Therefore, for the remainder of the paper we let $\Gamma = 0$.

We can calculate $\phi(\omega)$ using known equations for the different loss mechanisms [38, 39, 44, 45], but this is not ideal for our purposes. The mechanical losses of fused silica have been studied intensively by the gravitational wave community for use in low-thermal noise test mass suspensions. The models developed by these investigations are useful for optimizing a fused silica sensor's topology, but the only information we can experimentally obtain for $\phi(\omega)$ is the Q-factor. Therefore, we want an equation for the thermal noise in terms of Q rather than $\phi(\omega)$. For this we assume that the internal losses are constant in the bandwidth of interest and are given by:

$$\phi(\omega) = \frac{1}{Q} \tag{4.5}$$

Using these assumptions, we simplify Equation 4.4 to:

$$\tilde{a}_{\mathrm{th}}^2(\omega) = \frac{4k_{\mathrm{B}}T\omega_0^2}{mQ\omega} \tag{4.6}$$

This is the final equation we use to calculate the thermal acceleration noise. Note that larger Q-factors lead to lower thermal noise, highlighting the importance of fused silica as a material choice. Fused silica is known to have very low internal losses at room temperature, with Q-factors well above 1×10^6 for high-frequency resonators [14, 15, 51, 52, 53] and above 1×10^5 for low-frequency devices [23]. Research into the material properties of fused silica at cryogenic temperatures has shown that the mechanical losses ϕ of this material increases substantially as temperature decreases [54]. At $30\,\mathrm{K}$ these losses can increase by as much as four orders of magnitude, which would in turn increase the thermal acceleration noise of our optomechanical accelerometer by a factor of 100. Moreover, this work suggested a fused silica resonator could be operated at temperatures as low as $225\,\mathrm{K}$ with minimal quality factor degradation of at most a few percent. Hence, we adopt $225\,\mathrm{K}$ as the minimum operating temperature of our accelerometer, which is not anticipated to impede our device's performance in the context of space geodesy, as such systems typically operate near room temperature.

In addition to thermal motion, displacement readout noise from the laser interferometer contributes significantly to the acceleration noise floor of our optomechanical accelerometer. For this section, we note that the Laser Interferometer Space Antenna (LISA) Pathfinder mission has demonstrated an optical readout with a sensitivity reaching $35\,\mathrm{fm}/\sqrt{\mathrm{Hz}}$ [3], representing an excellent sensitivity level that can be used to model our own projected noise floor. To convert this displacement noise to acceleration, we simply apply the transfer function in Equation 4.2. This readout noise is assumed to be incoherent with the thermal motion of the resonator, so the two noises add in quadrature:

$$\tilde{a}_{\text{floor}}^2(\omega) = \tilde{a}_{\text{th}}^2(\omega) + \left|\frac{\tilde{a}(\omega)}{\tilde{x}(\omega)}\right|^2 \tilde{x}_{\text{int}}^2(\omega) \tag{4.7}$$

Equation 4.7 is plotted in Figure 4.6a, where we observe the acceleration sensitivity is anticipated to be $5 \times 10^{-11}\,\mathrm{ms}^{-2}/\sqrt{\mathrm{Hz}}$ at $1\,\mathrm{Hz}$ and increases towards low frequencies as $f^{-1/2}$. Above resonance, the noise floor increases rapidly, dominated by readout noise, while below resonance the thermal motion is sufficiently low that the noise floor is $1 \times 10^{-9}\,\mathrm{ms}^{-2}/\sqrt{\mathrm{Hz}}$ at $1\,\mathrm{mHz}$.

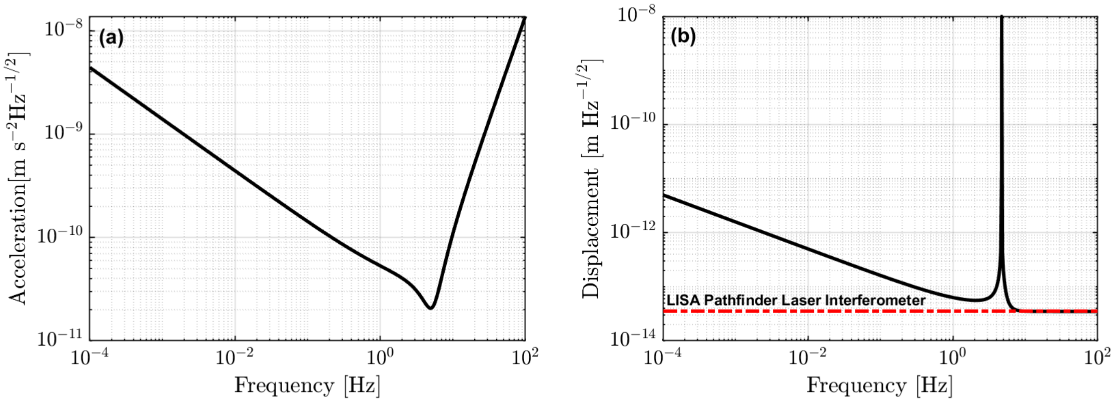

Figure 4.6: (a) The acceleration noise floor of our optomechanical accelerometer including thermal motion from the resonator and readout noise from the laser interferometer. (b) The corresponding displacement readout noise floor required to observe this acceleration noise level. Both plots assume a mechanical Q-factor of $(4.76 \pm 0.03) \times 10^5$ and a readout noise consistent with that achieved by LISA Pathfinder [3].

4.2 Results

To demonstrate the acceleration sensing capabilities of our device we take simultaneous measurements with the optomechanical accelerometer and a Nanometrics Trillium Horizon 120-2 (T120H) seismometer [13]. The T120H seismometer is placed on top of the vacuum chamber that houses the resonator to ensure seismic noise couples into both accelerometers coherently. Moreover, the axis of motion for the resonator has been set up to coincide with the x-axis of the seismometer, allowing for an easy comparison of the two sensors. Photos of this setup are shown in Figure 4.7. In this section, we present preliminary measurements taken with our optomechanical accelerometer and describe correction methods we use to remove various noise sources.

4.2.1 Measuring seismic noise

Data was taken for 60 hours allowing us to observe frequencies as low as $4.6\,\mu\mathrm{Hz}$. The acceleration noise observed by both devices are shown in Figure 4.8, where we note agreement in the micro-seismic band between $100\,\mathrm{mHz}$ and $500\,\mathrm{mHz}$. The seismometer detected less noise at frequencies below this bandwidth, indicating that our optomechanical accelerometer was limited by environmental noise below $100\,\mathrm{mHz}$. Even though our optomechanicl accelerometer's observed noise is significantly higher than the measured optical readout noise in Figure 4.5, the laser path length difference between the measurement and reference interferometers when the resonator is incorporated in the setup is greater than $1\,\mathrm{cm}$. This in turn enlarges the laser frequency noise in comparison to what was observed in the interferometer stability test.

4.2.2 Data Post-Correction

The data taken with our optomechanical accelerometer presented in Section 4.2.1 was initially unable to observe the same acceleration noise as our T120H seismometer below $100\,\mathrm{mHz}$ due to a combination of signals originating from the environment and the optical readout. However, with careful environmental monitoring some of this noise can be removed in post-correction. In this section we discuss the different noise removal methods we utilize in our data to achieve a better acceleration sensitivity, and correspondingly better agreement with the commercial seismometer.

4.2.2.1 Time Domain Linear Regression

A portion of the environmental noise in our data can be removed by performing linear fittings to different sets of environmental data taken at the same time as the acceleration measurement. In addition to the previously discussed delay-line interferometer, this environmental data includes the

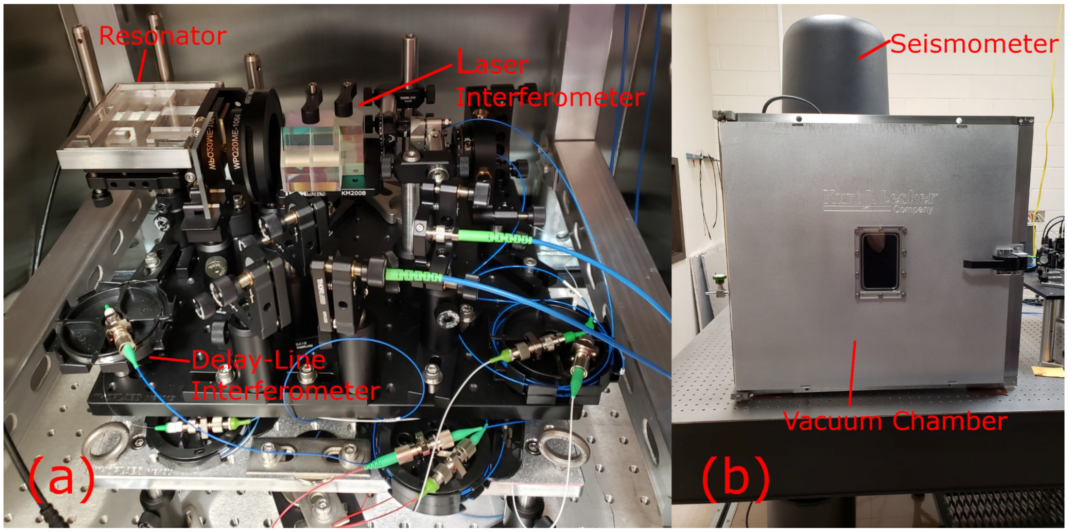

Figure 4.7: (a) An image of our experimental setup, including our fused silica resonator, heterodyne laser interferometer, and delay-line interferometer. (b) An image of the commercial seismometer's setup relative to our vacuum chamber, which houses the items shown in (a).

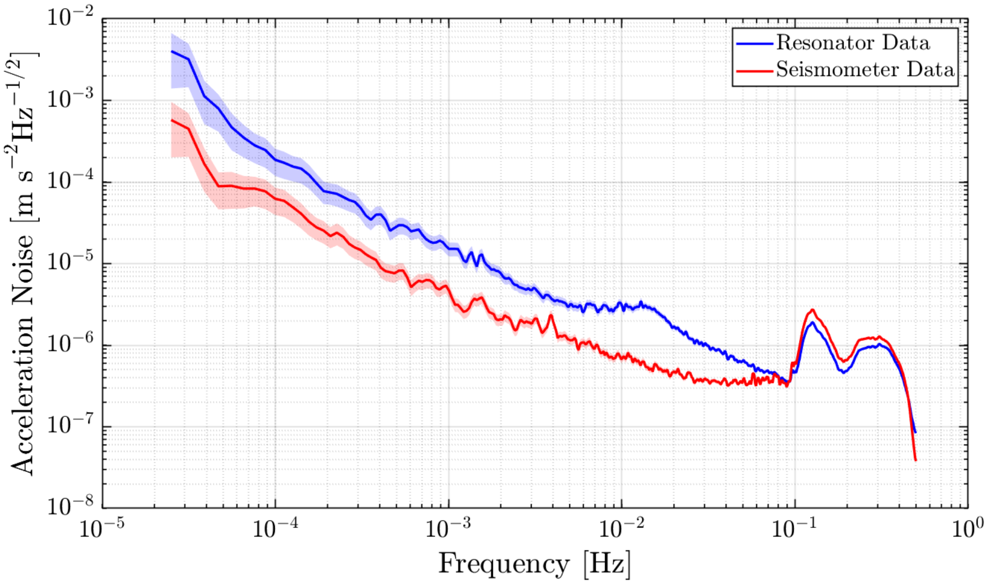

Figure 4.8: The acceleration noises measured by our optomechanical accelerometer and Trillium Horizon 120 seismometer. We observe good agreement between $100\,\mathrm{mHz}$ and $500\,\mathrm{mHz}$. The shaded areas represent the estimated error bars of the spectra.

room temperature, vacuum chamber temperature, vacuum pressure, and the heterodyne signal amplitudes of the measurement, reference, and delay-line interferometers. Furthermore, we retrieved data on the ambient weather conditions from Texas A&M University's Research Farm [55] as the changing barometric pressure can induce tilting in our optical bench which causes a projection of the local gravity into the resonator's axis of motion.

For frequencies below $100\,\mu\mathrm{Hz}$ we find that the barometric pressure dominates the resonator's acceleration noise, with a coupling coefficient of $-29.24\,\mathrm{mm\,s^{-2}\,Bar^{-1}}$ found by linear regression in the time domain. To isolate the frequency band where the pressure noise dominates, this linear regression is performed on bandpass-filtered data. While effective, the efficacy of this post-correction is limited by the data acquisition of the weather station at Texas A&M's Research Farm, which reports hourly averages. The ultra-low Nyquist frequency of $139\,\mu\mathrm{Hz}$ restricts our ability to correct our data for barometric pressure fluctuations above that frequency. As part of our ongoing efforts to develop this technology, we will include in-house measurements of the ambient laboratory air pressure taken with a commercial barometer sampled at a much higher rate to avoid this problem.

The acceleration noise caused by laser frequency noise is found in a similar way. Laser frequency fluctuations appear in our resonator data as a bump around $12\,\mathrm{mHz}$, which can be observed in Figure 4.8. By applying a bandpass filter with corner frequencies of $5\,\mathrm{mHz}$ and $40\,\mathrm{mHz}$ to the resonator and delay-line interferometer data, we find a coupling coefficient of $1.1421\,\mu\mathrm{m\,s^{-2}\,rad^{-1}}$. This coupling coefficient informs us on how stable a laser would need to be in order for our resonator to be thermally limited. The phase of our delay-line interferometer, ϕ_{delay}, is proportional to our laser source's frequency noise, ν_{laser}, by [1]:

$$\phi_{\mathrm{delay}} = \frac{2\pi\Delta L}{c}\nu_{\mathrm{laser}} \tag{4.8}$$

where c is the speed of light and ΔL is the path length difference in the delay-line interferometer, which is $2\,\mathrm{m}$ in our case. This suggests that the coupling factor between our resonator's acceleration, a, and the laser frequency noise ν_{laser} is $4.709 \times 10^{-14}\,\mathrm{m\,s^{-2}\,Hz^{-1}}$. Using our projected thermal acceleration noise shown in Figure 4.6, we anticipate a laser frequency stability of $1.06\,\mathrm{kHz}/\sqrt{f}$ is required for observing the thermal motion of our resonator. This stability is very achievable and the frequency stability of the laser onboard GRACE-FO is much better than this requirement [56].

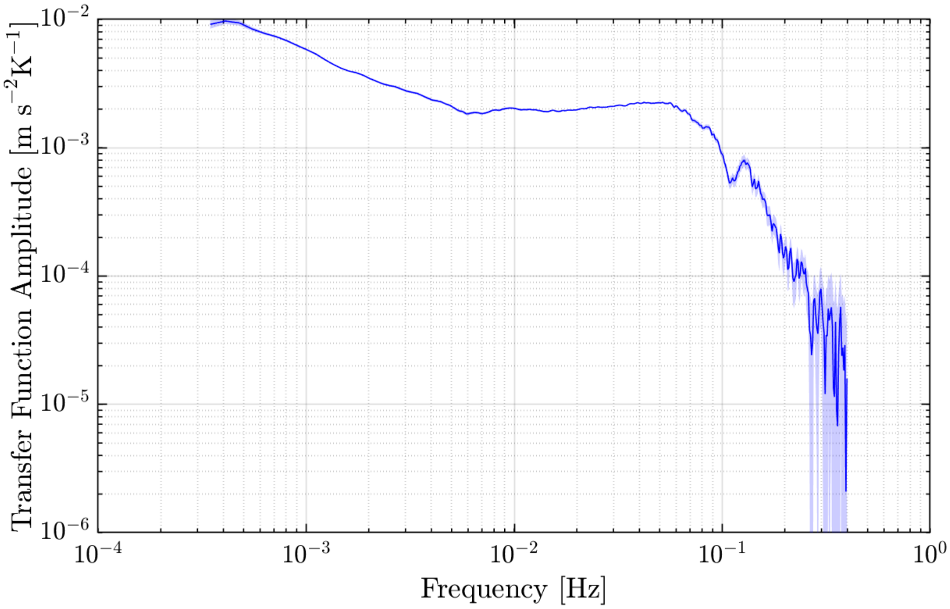

Figure 4.9: (a) The transfer function between vacuum chamber temperature and acceleration. Note that between $300\,\mu\mathrm{Hz}$ and $50\,\mathrm{mHz}$, the amplitude varies by nearly factor of 5, suggesting that a linear regression would not be suitable for this data set. The transfer function is not plotted below $300\,\mu\mathrm{Hz}$ because the low number of averages causes large uncertainties. The shaded area represents the estimated error bars of the spectrum.

4.2.2.2 Transfer Function

The linear regression method of noise subtraction that we use for the barometric pressure and laser frequency corrections assumes that the phase and amplitude of their respective coupling coefficients are uniform over the bandwidths we are correcting. However, noise generally does not couple into a given system uniformly in frequency; both the amplitude and phase of the coupling factor can be frequency dependent. The temperature inside our vacuum chamber for example is a significant source of noise in our experiment, but it does not couple uniformly in frequency. Because of this we must use a different approach to remove temperature effects from our data. We correct for the vacuum chamber temperature by calculating a transfer function, $H_{Ta}(\omega)$, between the temperature and acceleration data [57]. This transfer function is typically estimated by taking the ratio of the cross power spectral density (CPSD)of the acceleration and temperature data, $S_{Ta}(\omega)$, and the power spectral density (PSD) of the acceleration, $S_{aa}(\omega)$ [58]:

$$H_{Ta}(\omega) = \frac{S_{Ta}(\omega)}{S_{aa}(\omega)} \tag{4.9}$$

For this spectral analysis, we use a Nuttall window function and 1.98×10^5 samples. The number of averages increases with frequency. The lowest frequency bin, $5\,\mu\mathrm{Hz}$ has only one average, which increases to over 1100 averages at $0.5\,\mathrm{Hz}$. At $230\,\mu\mathrm{Hz}$, there are 10 averages, and so we adopt this frequency as the approximate cutoff below which the spectral analysis has too few averages to be reliable. This analysis is performed with LTPDA, an open-source MATLAB toolbox for data analysis and signal processing developed and distributed by the LISA Pathfinder community [59].

The amplitude of the transfer function between the vacuum chamber temperature and the resonator's acceleration after removing laser frequency and barometric pressure noise is shown in Figure 4.9. We observe a frequency dependent transfer function amplitude ranging from $2 \times 10^{-3}\,\mathrm{ms^{-2}K^{-1}}$ to $1 \times 10^{-2}\,\mathrm{ms^{-2}K^{-1}}$. Similar to laser frequency noise, the transfer function presented in Figure 4.9 can be used to estimate the temperature stability required for the resonator to be limited by thermal motion. At $10\,\mathrm{mHz}$ the amplitude of this transfer function is on the order of $10\,\mathrm{mm\,s^{-2}\,K^{-1}}$ while the thermal acceleration noise at this frequency is approximately $4 \times 10^{-10}\,\mathrm{m/s^2/\sqrt{Hz}}$. This suggests that a thermally limited acceleration measurement would require an environmental temperature stability of $4 \times 10^{-8}\,\mathrm{K/\sqrt{Hz}}$. This requirement being very improbable to achieve, we instead will investigate the precise mechanism through which temperature couples into our setup and reduce it to relax the temperature stability we need to reach.

The typical transfer function one might expect for temperature coupling is one that resembles a low-pass filter [57], which is not fully observed in our setup. This behavior could be due to the fact that temperature is a ubiquitous effect, present everywhere in the setup. The complicated transfer function could be composed of several thermal effects occurring simultaneously in different parts of the experiment. The exact mechanism causing temperature fluctuations to couple into our setup in this manner is currently under investigation.

We also calculate the uncertainty in the transfer function, which depends on the transfer function amplitude, the coherence between vacuum temperature and acceleration $C_{Ta}(\omega)$, and the number of averages in each frequency bin [58]. In bins where either the coherence between the two time-series is poor or the number of averages is low, the variance in the transfer function will be large. The coherence, shown in Figure 4.10, is estimated by taking the ratio of the magnitude of the cross-spectral density, $|S_{Ta}(\omega)|^2$, and the product of the power spectral densities $S_{aa}(\omega)$ and $S_{TT}(\omega)$ [58]:

$$C_{Ta}(\omega) = \frac{|S_{Ta}(\omega)|^2}{S_{aa}(\omega) S_{TT}(\omega)} \tag{4.10}$$

The coherence between the vacuum chamber temperature and the acceleration data is larger than 0.8 between $300\,\mu\mathrm{Hz}$ and $60\,\mathrm{mHz}$, indicating that temperature fluctuations are a dominant noise source in this frequency band. Above $60\,\mathrm{mHz}$ there is a sharp decrease in the coherence, explaining the corresponding decrease in transfer function amplitude and the increase in the transfer function uncertainty.

The temperature-induced acceleration noise is calculated by taking the FFT of the temperature data, applying the transfer, and then taking the inverse-FFT to return to the time-domain. The inverse transform step of this process, while not strictly necessary if one wants frequency-domain results [58], is useful for visualizing the data and identifying the next limiting noise source.

The noise breakdown for this measurement is shown in Figure 4.11(a) as well as the residual after removing the laser frequency, pressure, and temperature noise. This post-correction is compared to the measured interferometric readout noise, from which we see that the resonator's

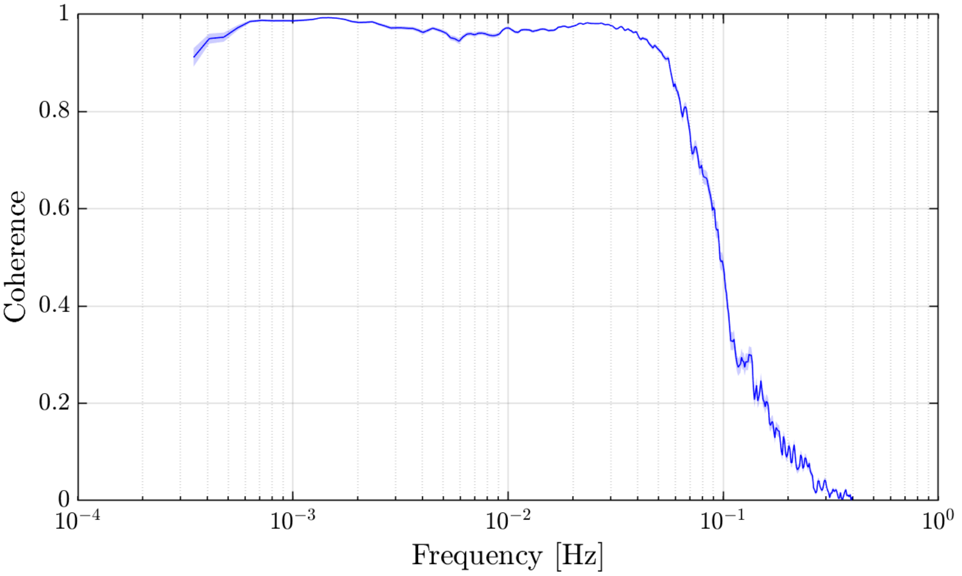

Figure 4.10: The magnitude of the coherence between our vacuum chamber temperature and our resonator's acceleration data. The coherence is greater than 0.8 between $0.3\,\mathrm{mHz}$ and $60\,\mathrm{mHz}$, indicating that temperature is a significant noise source. The coherence function is not plotted below $300\,\mathrm{\mu Hz}$ because the low number of averages causes large uncertainties. The shaded area represents the estimated error bars of the spectrum.

acceleration data is above the acceleration noise of the interferometer. This suggests that the noise we are observing is real signal with seismic or environmental origins. Figure 4.11(b) also shows the difference between our optomechanical accelerometer data and the seismometer data. We observe that this difference is larger than the readout-induced acceleration noise, suggesting that the residual is limited by noise not originating from the optical readout. Our data does not show any more significant coherences between our acceleration and environmental monitoring. As such, we consider the possibility that the residual noise in our accelerometer data was, at least partially, introduced through post-correction. For example, if the self-noise of our temperature sensors is on the order of $100\,\mathrm{\mu K}/\sqrt{\mathrm{Hz}}$ at $10\,\mathrm{mHz}$, that self-noise would be added to our acceleration measurements during post-correction at a level of approximately $2 \times 10^{-7}\,\mathrm{ms^{-2}}/\sqrt{\mathrm{Hz}}$, ultimately restricting our final sensitivity. This highlights the importance of investigating and characterizing these noise sources as reducing their physical coupling into the experiment will offer better results than

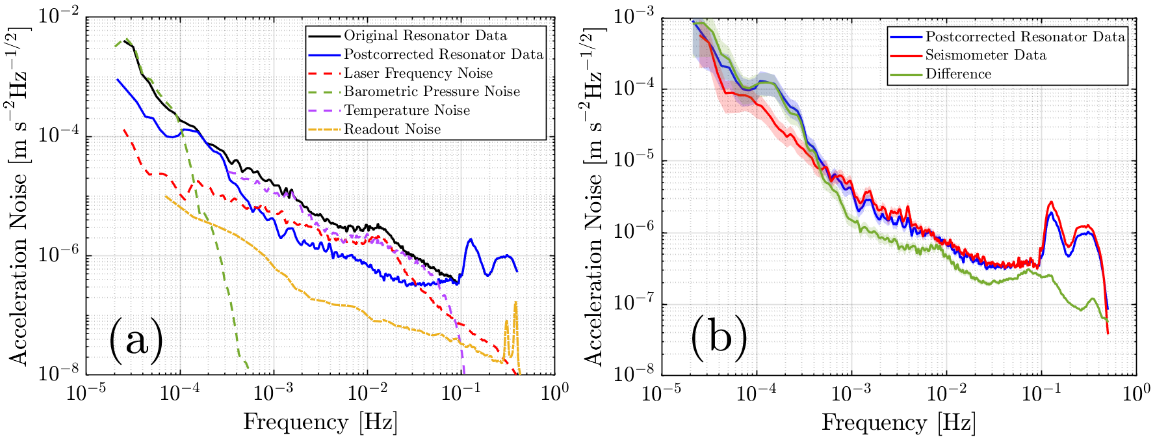

Figure 4.11: (a) The amplitude spectral density of a seismic measurement taken with our optomechanical accelerometer alongside the noise contributions from laser frequency fluctuations, barometric pressure, and vacuum chamber temperature. Also shown is residual after removing all three noise sources, demonstrating a significant reduction in noise from $0.2\,\mathrm{mHz}$ to $100\,\mathrm{mHz}$ and below $100\,\mu\mathrm{Hz}$. (b) A comparison of the post-corrected resonator data to the seismometer data. The good agreement between the two devices now extends down to $1\,\mathrm{mHz}$. The shaded areas represents the estimated error bars of the spectra.

decohering our data in post-corrections.

Furthermore, we find that after removing the temperature and barometric pressure fluctuations, the good agreement between our resonator and seismometer data extends down to $1\,\mathrm{mHz}$, which can be visualized in frequency-space in Figure 4.11a and in the coherence between the two data sets in Figure 4.12. The bump in the post-corrected resonator data between $100\,\mu\mathrm{Hz}$ and $400\,\mu\mathrm{Hz}$ is likely residual barometric pressure noise that could not be removed due to the low Nyquist frequency of the pressure measurement. Moreover, we can visually compare the data from both accelerometers in the time domain to demonstrate the agreement between the sensors. In Figure 4.13 we plot a 1000 second segment of both data streams and in doing so, we observe excellent agreement in both the magnitude and phase of the two devices. These comparisons validate our resonator's ability to detect seismic noise above $1\,\mathrm{mHz}$.

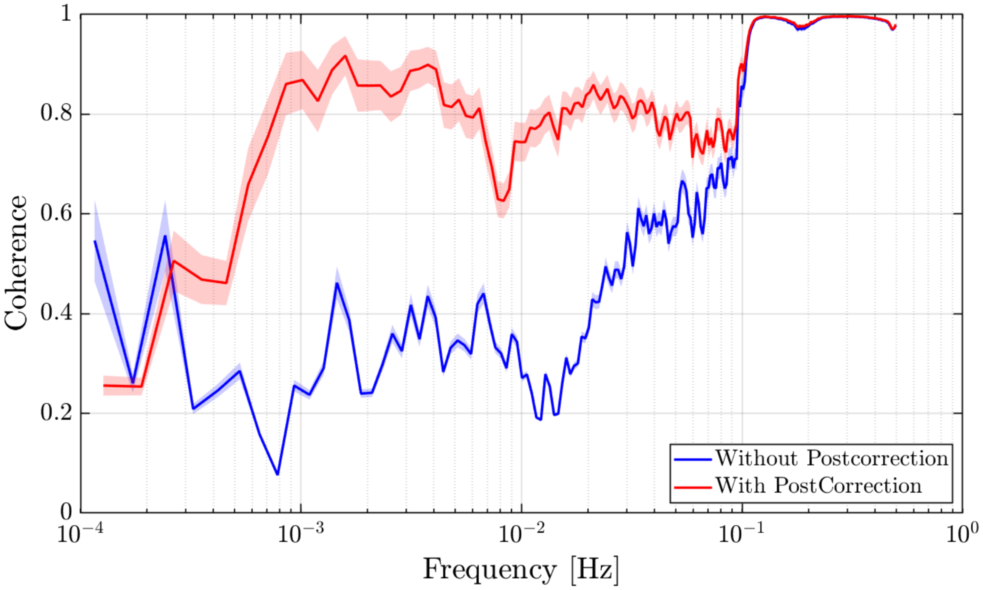

Figure 4.12: The magnitude of the coherence between our post-corrected resonator data and seismometer data both before and after removing environmental noises. It can be seen that by removing temperature, pressure, and laser frequency fluctuations from the resonator data, the coherence above $1\,\mathrm{mHz}$ improves significantly. The shaded areas represents the estimated error bars of the spectra.

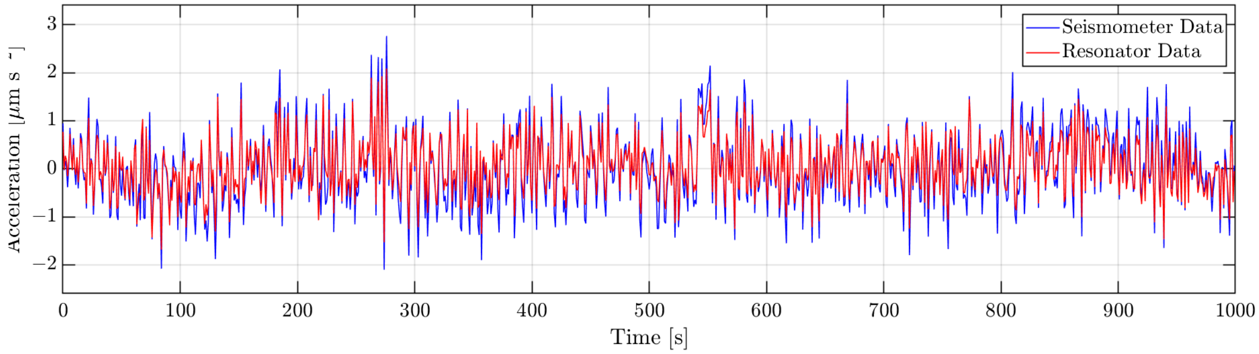

Figure 4.13: A 1000 second-long subset of the acceleration time series obtained by our optomechanical accelerometer and seismometer, in which we see excellent agreement between the two time series. Both traces are high-pass filtered above $0.8\,\mathrm{mHz}$ for better comparison of the frequency band with high coherence.

4.3 Discussion

4.3.1 Comparative Technology Assessment

In Section 4.1.2 we calculated the noise floor of our optomechanical accelerometer using estimates of the optical readout noise and the thermal motion associated with our experimentally measured Q-factor. This noise floor can be compared to existing technologies to assess the viability of our accelerometer for different applications. In Figure 4.14, we plot our estimated noise floor against the GRACE[4] and GRACE-FO[5] accelerometers, as well as several ground-based seismometers including the Geotech S-13, the Nanometrics Trillium 360, and the Nanometrics Trillium 120, which is the one we utilized in our laboratory for the comparison measurements presented in Section 4.2.1[6]. We observe that our accelerometer is anticipated to have a competitive, if not lower, acceleration noise than the ground-seismometers, suggesting that our device will be useful for seismometry and ground-based geodesy studies. Moreover, our accelerometer has a mass of $58.2\,\mathrm{g}$, and we anticipate the realization of a highly compact and lightweight system compared to existing systems. Because of this, our optomechanical accelerometer is more smaller, more portable, and better suited for field work than these commercial technologies.

When compared to the GRACE and GRACE-FO accelerometers, our optomechanical accelerometer is competitive at higher-frequencies around $1\,\mathrm{Hz}$, but is expected to be noisier at lower-frequencies. However, current mass change measurements taken by satellite gravity recovery missions are limited primarily by temporal aliasing errors, not accelerometer noise[60]. Hence, despite this slightly higher noise floor at low frequencies, we expect our optomechanical accelerometers to be able to provide meaningful data for science observations. Rather, with the advantages exhibited by our optomechanical accelerometer, incuding a lower weight, more compact form, and the ability to be tested on-ground, our accelerometer is still valuable for satellite geodesy missions.

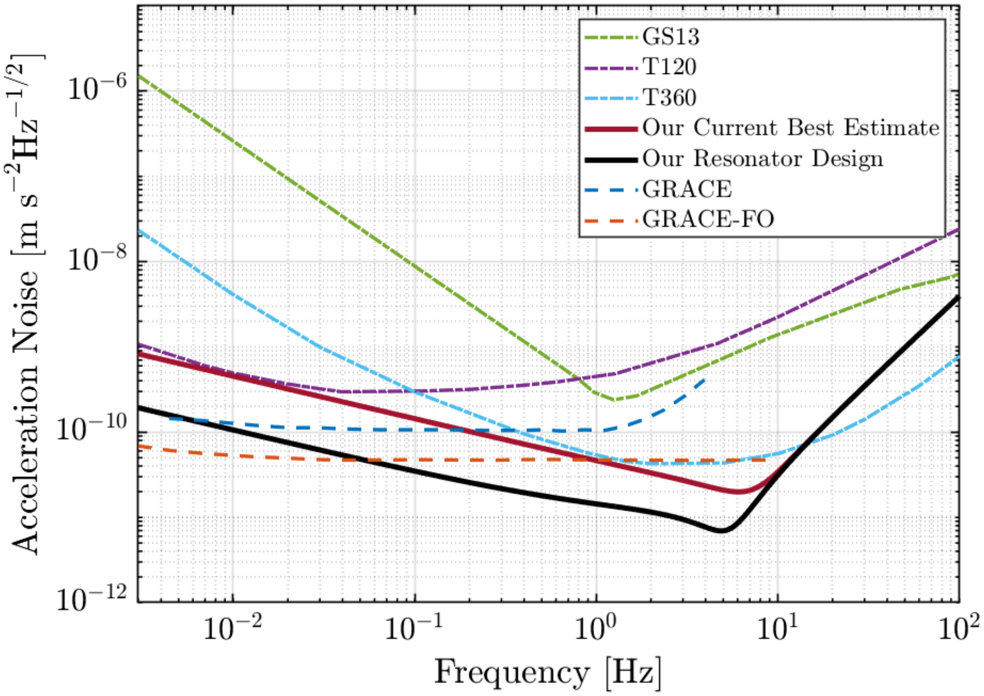

Figure 4.14: The projected noise floor of our optomechanical accelerometer compared to those of other technologies, including the GRACE[4] and GRACE-FO[5] accelerometers and the Geotech S-13, Trillium 120, and Trillium 360 seismometers[6]. Two traces are plotted for the noise floor of our accelerometer: our current best estimate using our experimental value of the Q-factor, and our resonator design using a value of Q calculated using models for the loss mechanisms of fused silica.

4.3.2 Planned Developments

In the measurements presented in this dissertation, we encountered several noise sources, such as instabilities in the laser frequency and the optical readout, limiting our ability to detect low-frequency signals. Future measurements will be conducted with a frequency-stabilized laser and compact quasi-monolithic interferometers to improve our sensor's low-frequency sensitivity. This interferometer operates on the same principles as our current readout. It consists of prisms and beamsplitters bonded together and small enough that they can be integrated onto the wafer of our resonator, miniaturizing our current experimental setup while offering better mechanical stability. A photo of this interferometer is shown in Figure 4.15(a).

Other improvements that can be made to reduce the measurement noise include thermally isolating the system to dampen temperature fluctuations as well as investigating noise due to tilt-to-length coupling and non-linear optical path length differences.

Furthermore, we will experimentally measure the thermal noise floor of our accelerometer by performing a Huddle test. The test consists in placing two identical resonators close to each other. The seismic noise would couple into both devices coherently. After removing that correlated seismic noise, the remaining noise will be the uncorrelated noise originated by the resonators themselves.

These developments and a better understanding of low-frequency environmental noise sources will allow for other tests to characterize our acceleration sensing capabilities, e.g., to monitor the lunar and solar tidal acceleration changes.

Finally, there are several extensions of the work presented in this dissertation that would make this optomechanical accelerometer technology ready for use onboard a space geodesy satellite. Specifically, we are currently developing appropriate mounts and launch-lock mechanisms for the accelerometer that facilitate its deployment and protect the dynamic test mass during installation and launch. This cage should include a method of securing the test mass and flexures to avoid damage while not in use, such as during launch when significantly higher accelerations and shock are expected in contrast to science operation. To this end, the higher-order violin modes of the flexures in our accelerometer should be investigated in greater depth to ensure compatibility with the vibrational loads present during launch.

Moreover, a triaxial optomehanical accelerometer could be constructed from a series of resonators operating along different axes, which is required for observing all non-inertial perturbations while in orbit. A concept design of such a sensor is depicted in Figure 4.15(b), which has a volume of $110 \times 110 \times 22\,\mathrm{mm}$ and a mass of $0.282\,\mathrm{kg}$, not including the masses of the optical readout, which should be low overall as each quasi-monolithic interferometer assembly weighs only $4.5\,\mathrm{g}$. This design is a quasi-monolithic assembly of two layers of fused silica resonators that are separated by spacers. The top layer holds two orthogonal resonators identical to the one presented in Section 4.1.1.1 operating along the x and y axes. Because these resonators share the same topology as the one presented in this paper, they will have the same noise floors shown in Figure 4.6. Also on the top layer is a cutout that houses the optical readouts for all three axes. An interferometer reaches the test mass of the bottom layer through a hole in the top layer covered by a pentaprism.

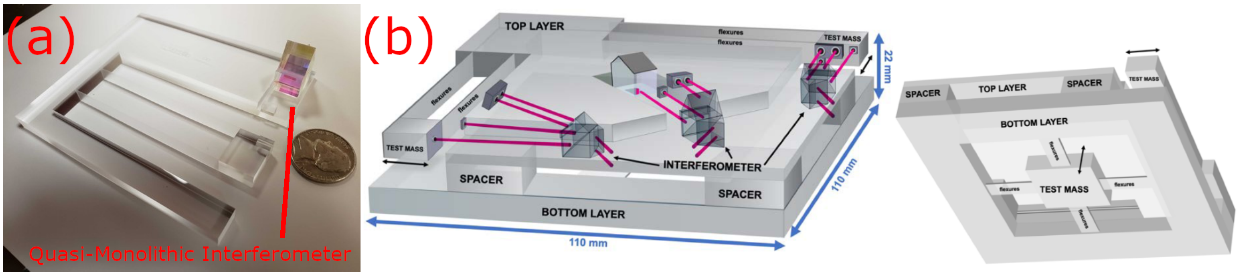

Figure 4.15: (a) A visualization of our quasi-monolithic interferometer integrated onto the wafer of our resonator. A US nickel is included for scale. (b) A rendering of a triaxial accelerometer concept. This design consists of two layers: the top containing resonators oscillating in the x and y-axes and the bottom with a resonator operating along the z-axis.

The bottom layer contains a resonator that measures out-of-plane accelerations along the z-axis. However, due to limitations in fabrication a different topology is required for measuring the out-of-plane motion. To this end, we have developed a preliminary design for the bottom layer resonator which consists of a $12\,\mathrm{g}$ rectangular prism test mass supported by flexures on four sides. These flexures have cross sections of $8 \times 0.1\,\mathrm{mm}$ and are oriented such that the test mass oscillates along the z-axis. Tuning the lengths of the flexures as well as the test mass allows for a natural frequency less than $10\,\mathrm{Hz}$, which improves the resonator's low-frequency sensing capabilities. Like the resonator presented in Section 4.1.1.1, we require all higher order modes to have resonances larger than the natural mode by an order of magnitude. In the topology we have chosen for the bottom layer resonator, however, tip-and-tilt modes can have a low enough frequency to allow cross-talk between the modes of the resonator.

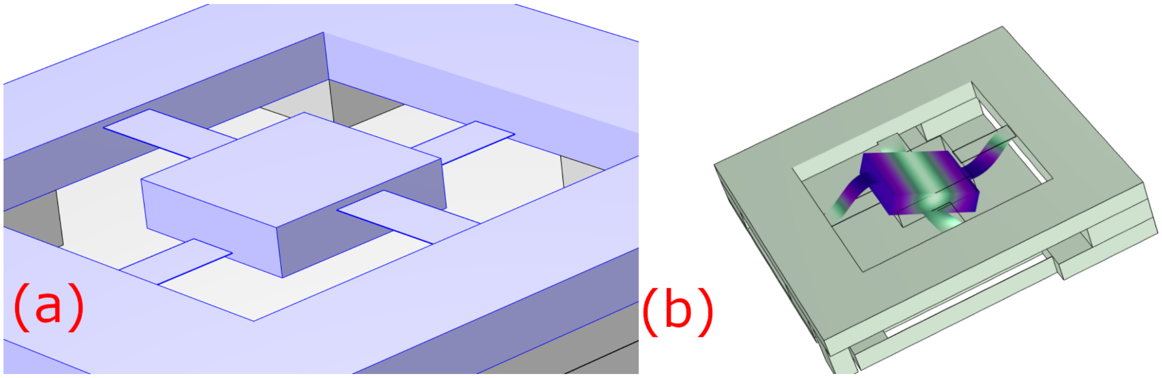

Figure 4.16: (a) A close-up of the z-axis test mass and its flexures. Note that the flexures are not at the mid-point of the wafer, but have different offsets to increase the stiffnesses and frequencies of tip-tilt modes. (b) The tip-tilt mode of the z-axis resonator as seen from the underside of the three-axis resonator. The colors indicate the total displacement, with light green being the stationary and purple being the largest displacement.

Figure 4.16(a) visualizes this tip-and-tilt mode. To combat this, we offset the flexure heights relative to the bottom of the wafer. Two flexures are $1\,\mathrm{mm}$ above the bottom of the wafer and the other two are $1\,\mathrm{mm}$ below the top of the wafer. Having the test mass and flexures connected at multiple points along the z -axis increases the frequency of this tip-tilt mode to above the $10\times$ threshold. Figure 4.16(b) depicts a close-up of the test mass and flexures to show this offset.

With the aim of developing a triaxial accelerometer with equal noise floors along all three axes, an optimization of the bottom layer resonator must be performed to ensure it has comparable noise to the top layer resonators. This optimization includes adjusting the test mass and cross-section to lower its resonance and reduce its thermal motion while keeping the stress in the flexures within a safe operating range.

4.4 Conclusion

In this chapter we demonstrate that a compact and lightweight optomechanical accelerometer etched from a monolithic wafer of fused silica with dimensions of $90\,\mathrm{mm} \times 80\,\mathrm{mm} \times 6.6\,\mathrm{mm}$ can detect seismic noise above $1\,\mathrm{mHz}$ in good agreement with commercial seismometer technologies. This device has a test mass that is suspended mechanically by thin flexures, allowing it to be tested on ground where some electrostatic devices cannot. As such, we propose the use of this technology onboard future space geodesy missions, as well as in ground-based planetary and geodesy applications, for measuring non-inertial disturbances.

Although a direct measurement of the accelerometer's noise floor is not possible due to our testing environment being flooded with signals, there is presently no evidence of noise sources that would prevent us from observing the self-noise of our accelerometer with a sufficiently quiet test bed. The anticipated thermal acceleration noise is approximately $5 \times 10^{-11}\,\mathrm{ms}^{-2}/\sqrt{\mathrm{Hz}}$ at $1\,\mathrm{Hz}$, making this technology competitive with the accelerometers that have flown on space geodesy missions such as GRACE and GRACE-FO. As such, our optomechanical accelerometer is expected to be suitable for satellite geodesy missions, among other applications.

The resonator's displacement is measured optically with a heterodyne interferometer and a $1064\,\mathrm{nm}$ laser that is not currently frequency stabilized. Below $100\,\mathrm{mHz}$ the acceleration data obtained by our resonator is dominated by laser frequency noise as well as temperature and pressure fluctuations. These noise sources can be partially removed by careful environmental monitoring, significantly increasing the coherence between our resonator and a commercial seismometer. Future works will incorporate improvements to our optical readout, laser source, and environmental monitoring to further enhance our acceleration measurements.

5. TEMPERATURE DEPENDENCE OF FUSED SILICA RESONATORS

The performance models for the sensitivity of an optomechanical accelerometer developed in Chapters 2-4 have implicit and explicit dependencies on the temperature of the mechanical resonator, but until now we have assumed that temperature to be stationary in time. Fluctuating temperatures can change the mechanics of the resonator and introduce noise in our measurements. In this chapter, we adapt our analysis of the resonator mechanics to study the temperature dependence of our optomechanical accelerometer.

We model the resonant frequency as a cantilever system with a mass on one end. The equation of this resonance is given by [61]:

$$f_0 = \frac{1}{2\pi}\sqrt{\frac{k}{M_{test} + M_{flexure}}}, k = \frac{Ywt^3}{4L^3} \tag{5.1}$$

where k is the flexure stiffness, $M_{flexure}$ is the flexure mass, M_{test} is the test mass, Y is Young's modulus, and w, t, and L are the flexure dimensions. By inspection, there are two mechanisms through which temperature effects can couple into the resonant frequency: thermal expansion of the flexures and the temperature dependence of Young's modulus, which are given by [39]:

$$\alpha = \frac{1}{L}\frac{dL}{dT}, \beta = \frac{1}{Y}\frac{dY}{dT} \tag{5.2}$$

where α is the coefficient of thermal expansion, β is the temperature rate-of-change of Young's modulus. Equations 5.2 have simple exponential solutions that can be substituted into Equation 5.1 to model the temperature dependence of a cantilever stiffness. Doing so yields the equation:

$$k(T) = \frac{Y_i w_i t_i^3}{4L_i^3} e^{(\alpha+\beta)(T-T_i)} = k_i e^{(\alpha+\beta)(T-T_i)} \tag{5.3}$$

where T_i is a reference temperature and k_i, Y_i, w_i, t_i, and L_i are the cantilever properties at that reference temperature. With this result, Equation 5.1 can be rewritten as:

$$f_0^2(T) = f_{0,i}^2 e^{(\alpha+\beta)(T-T_i)} \tag{5.4}$$

For fused silica, the values of α and β are $5.5 \times 10^{-7}\,\mathrm{K}^{-1}$ and $1.52 \times 10^{-4}\,\mathrm{K}^{-1}$, respectively [39]. Hence, we anticipate the change in Young's modulus to be the dominant mechanism through which temperature couples into our resonator's frequency.

Equation 5.4 can be verified experimentally by computing a spectrogram of the test mass displacement. Over the span of several days or longer, the vacuum chamber which houses the resonator will heat and cool with the ambient room temperature with fluctuations as large as $1\,\mathrm{K}$. For such temperature fluctuations, Equation 5.4 is approximately linear, with the resonance changing as much as $300\,\mu\mathrm{Hz}$. To visualize this experimentally, we take the spectrogram of a 144 hour measurement, with each FFT segment containing 2^{20} samples. With a sampling frequency of $37.25\,\mathrm{Hz}$, we obtain a frequency resolution of approximately $18\,\mu\mathrm{Hz}$ in each FFT of the spectrogram, which is anticipated to allow us to measure the resonant frequency to within 10% at 35 timestamps. Figure 5.1 compares the resonant frequency to the vacuum chamber temperature over 144 hours, from which we observe good agreement between the two.

Moreover, Figure 5.2 depicts the resonant frequency plotted against temperature, which demonstrates a linear relationship. This agrees well with Equation 5.4, which is approximately linear for small temperature changes. A simple Taylor expansion of Equation 5.4 yields a linearized form which can be fit to our experimental data:

$$f_0^2(T) \approx f_{0,i}^2(1 + (\alpha+\beta)(T - T_i)) \tag{5.5}$$

From a least-squares fit, we find a $\alpha + \beta$ value of $(2.3 \pm 0.4) \times 10^{-4}\,\mathrm{K}^{-1}$.

Although the change in resonant frequency less than $1\,\mathrm{mHz}$ under normal operating conditions, this effect can introduce noise into our acceleration measurements by changing the transfer function of displacement to acceleration. Recall from Chapter 2 that the transfer function depends on

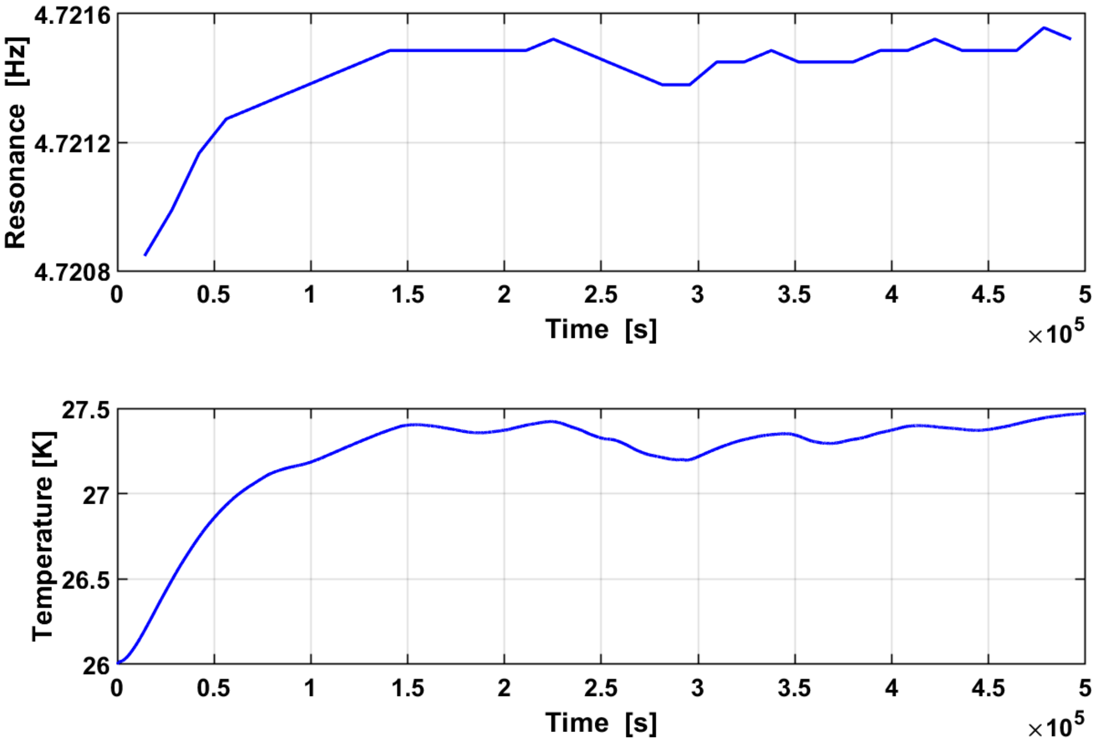

Figure 5.1: Time series plots of the resonant frequency of our resonator and the temperature inside the vacuum chamber.

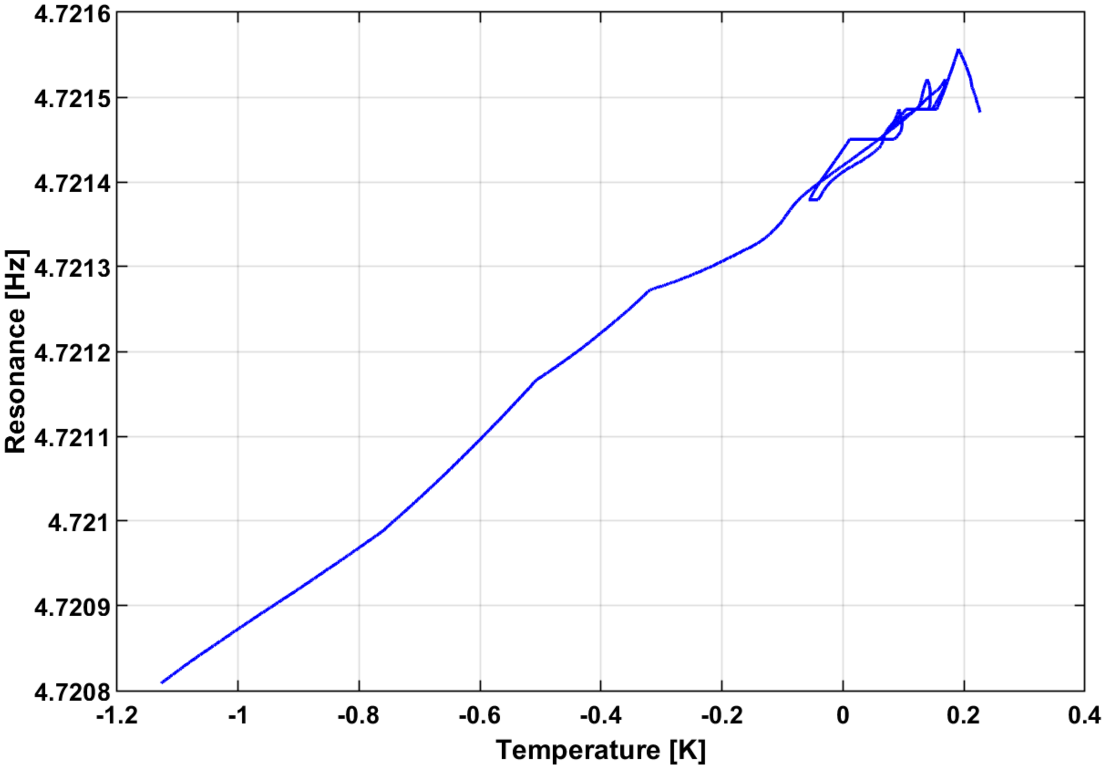

Figure 5.2: Time series plots of the resonant frequency of our resonator and the temperature inside the vacuum chamber.

the resonant frequency:

$$\tilde{a}(\omega) = -(\omega_0^2 - \omega^2 + i\omega_{0,i}\omega/Q)\tilde{x}(\omega) \tag{5.6}$$

We can calculate the noise introduced through the changing natural frequency by defining the acceleration $\tilde{a}$ as the sum of the mean acceleration $\bar{a}$ and a noise term:

$$\tilde{a}(\omega) = \bar{a}(\omega) + \delta a(\omega) \tag{5.7}$$

We can further substitute Equation 5.4 into Equation 5.6:

$$\bar{a}(\omega) + \delta a(\omega) = -(\omega_{0,i}^2 e^{(\alpha+\beta)(T-T_i)} - \omega^2 + i\omega_{0,i}\omega e^{\frac{1}{2}(\alpha+\beta)(T-T_i)}/Q)\tilde{x}(\omega) \tag{5.8}$$

Expanding the above equation for small temperature fluctuations using a Taylor series yields:

$$\begin{aligned}\bar{a}(\omega) + \delta a(\omega) = -[(&\omega_{0,i}^2 - \omega^2 + i\omega_0\omega/Q) + \\ &(\omega_{0,i}^2(\alpha+\beta)(T-T_i) + \frac{1}{2Q}i\omega_{0,i}\omega(\alpha+\beta)(T-T_i))]\tilde{x}(\omega)\end{aligned} \tag{5.9}$$

By inspection, we find the error term to be:

$$\delta a(\omega) = -(\omega_{0,i}^2(\alpha+\beta)(T-T_i) + \frac{1}{2Q}i\omega_{0,i}\omega(\alpha+\beta)(T-T_i))\tilde{x}(\omega) \tag{5.10}$$

For frequencies much below resonance, Equations 5.10 and 4.1 inform us that the acceleration noise induced by the changing resonant frequency is proportional to acceleration by a factor of $(\alpha + \beta)(T - T_i)$. Hence, under realistic operating conditions this noise source is not expected to significantly contribute to measurements. This is illustrated in Figure 5.3 which depicts the acceleration noise measured over a 6-day period and the expected noise caused by the changing resonance.

The results of this section have yielded valuable insights on how temperature fluctuations in our optomechanical accelerometer affect its mechanics and its acceleration sensitivity. Most im-

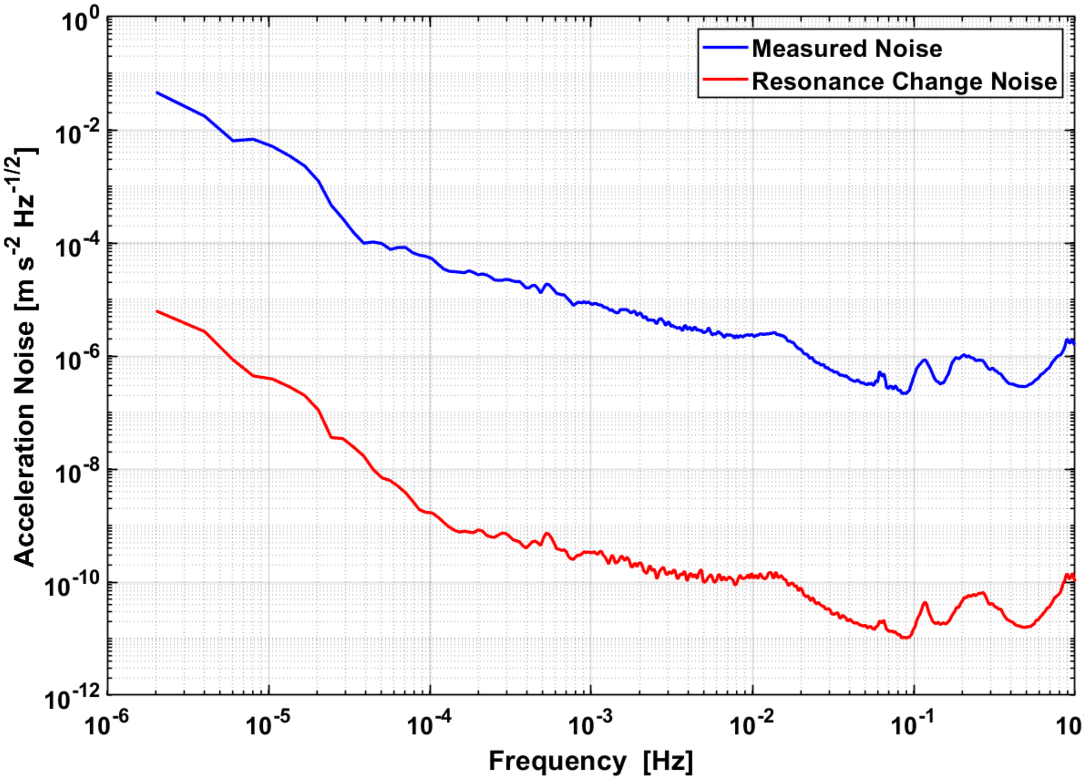

Figure 5.3: Linear spectral densities of a 6-day measurement comparing the observed acceleration noise and the calculated noise caused by temperature-induced resonance changes. We find that the resonance change noise is several orders of magnitude lower than the acceleration noise.

portantly, it has experimentally demonstrated that temperature-induced resonance change of the test mass is in good agreement with theoretical predictions. However, there are several flaws with the experimental approach presented here that if rectified could produce even more insights. Because the temperature fluctuations inside the vacuum chamber were small, about $1\,\mathrm{K}$, the change in resonant frequency was less than $1\,\mathrm{mHz}$. Not only does this measurement probe just a small temperature range, each FFT of the spectrogram requires more than 3 hours of data to adequately resolve one observation of the resonant frequency.

Rather than allowing the temperature to drift in accordance with daily cycles of the room temperature, this measurement could be improved by driving the temperature of the resonator with a polyimide heater. These electronic devices use resistive elements to produce heat through Joule heating and can reach temperatures greater than $200\,^{\circ}\mathrm{C}$ with watt densities of several W inch^{-2} [62]. From Equation 5.4, to heat the entire wafer of our optomechanical accelerometer from room temperature to $200\,^{\circ}\mathrm{C}$ would change the resonant frequency by approximately $48\,\mathrm{mHz}$. Hence, taking the FFT of a 200 second-long segment of data would be sufficient to resolve this frequency change to within 10%. In this way, the temperature dependence of our accelerometer could be probed over a much broader temperature range and in significantly less time.

6. INTEGRATION OF THE OPTICAL READOUT AND MECHANICAL RESONATOR

Despite our optomechanical accelerometer being designed to be easily integrated with a quasi-monolithic interferometer unit, the work presented in Chapter 4 did not use this compact optical unit. While the quasi-monolithic interferometer was under development and inspection, a larger heterodyne interferometer which operates on the same principles as the quasi-monolithic option was use to track the test mass of our optomechanical accelerometer. This readout solution was sufficient for the work in Chapter 4, however the larger optical setup introduced additional measurement noise as longer baselines are more susceptible to thermal effects and mechanical instabilities. In this chapter, we describe the the process of implementing the quasi-monolithic interferometer and present corresponding acceleration measurements. The design and testing of this optical unit was carried out by Dr. Yanqi Zhang. I then implemented the interferometer into our accelerometer setup and performed additional noise characterization.

Our quasi-monolithic interferometer, a diagram of which is shown in Figure 6.1, is a minitiarized version of the optical readout used in Chapter 4 which is adhered directly to the fused silica wafer. As a first attempt, double-sided tape was used to bond the optical unit to the wafer. Double-sided tape is advantageous as a short-term bonding solution because it has a uniform thickness and is easy to remove. Many industrial adhesives, on the other hand, allow optical alignments to drift while the glue cures if applied non-uniformly. This in turn can introduce significant noise in the our acceleration measurements through tilt-to-length coupling or worse ruin the optical alignment completely. Other rapidly curing adhesives, such as UV curing solutions, are difficult to remove making them unsuitable for a first attempt at bonding tilt-sensitive optical components.

An image of of our optomechanical accelerometer with the implemented quasi-monolithic interferometer is shown in Figure 6.2. Comparing this image to Figures 4.7 and 4.15(a) demonstrates the compact form of this interferometer in comparison to previous optical readouts. Particularly, the path length difference between the test mass mirror and the reference mirror, which is also bonded to the wafer, is significantly smaller. This consequently reduces the noise introduced

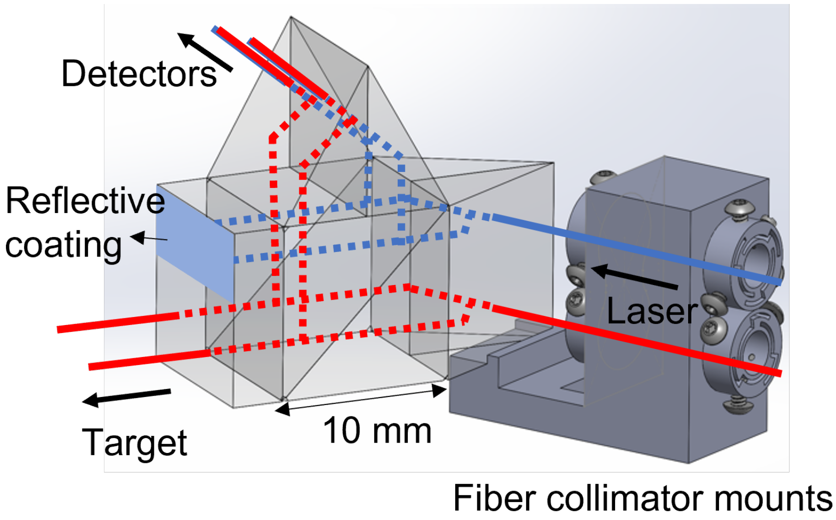

Figure 6.1: A rendering of the quasi-monolithic interferometer unit. The red and blue lines represent the paths of two laser beams with unlike frequency. In our setup, the frequency difference is $1\,\mathrm{MHz}$.

through laser frequency fluctuations and temperature fluctuations.

To test the acceleration noise floor achievable with the quasi-monolithic interferometer, we lock the test mass in place so that seismic motion does not couple into the measurements. This is shown in Figure 6.3, where we observe an acceleration noise floor as low as $1 \times 10^{-9}\,\mathrm{ms^{-2}Hz^{-1/2}}$ near $1\,\mathrm{Hz}$. The noise at $10\,\mathrm{mHz}$ is approximately $3 \times 10^{-7}\,\mathrm{ms^{-2}Hz^{-1/2}}$, better than the postcorrected trace in Figure 4.11(a) by more than a factor of 2. Moreover, this improvement in acceleration noise was achieved without decohering environmental variables. Compared to previous measurements, we did not observe laser frequency noise in this measurement as a result of the short path length difference between the measurement and reference interferometers. In addition, we did not observe a significant coherence between acceleration and temperature above $300\,\mu\mathrm{Hz}$ as we had in Chapter 4, indicating that the quasi-monolithic interferometer is less susceptible to temperature fluctuations in our optomechanical accelerometer. Similarly, we did not observe a significant noise contribution from barometric pressure like we had with our previous interferometer. Figure 6.4 depicts the coherences of temperature and barometric pressure with our measured acceleration noise where we a large reduction in coherence compared to the measurement presented in Figure 4.10.

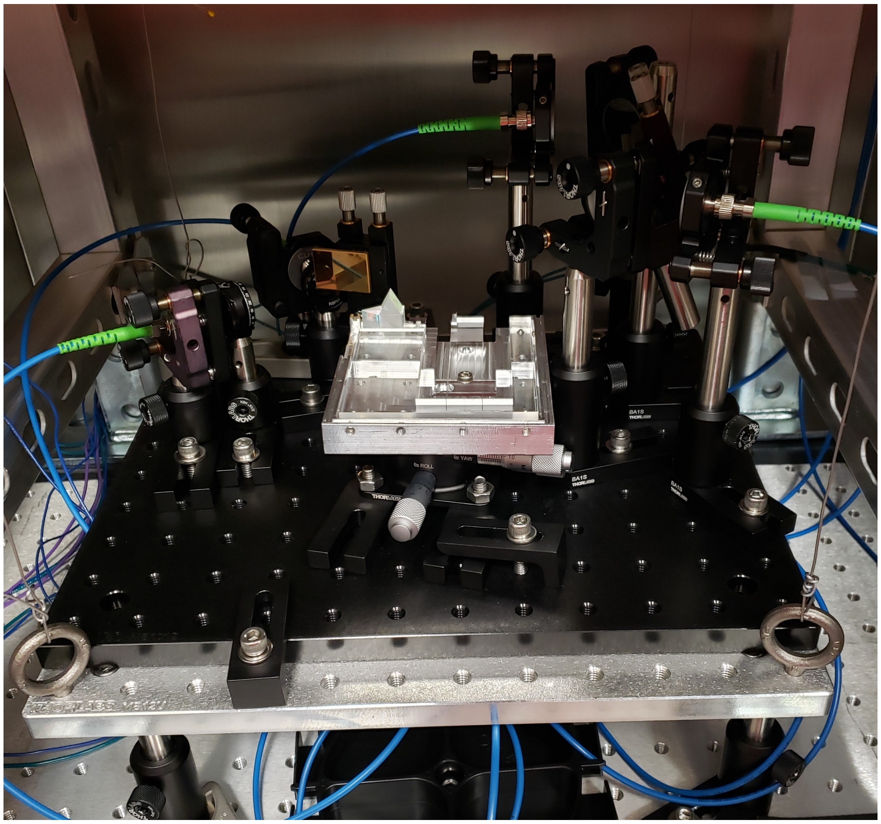

Figure 6.2: A photo of our optomechanical accelerometer setup using a quasi-monolithic inteferometer for test mass displacement measurement. This image can be compared to Figure 4.7 to visualize the size difference between the interferometers used in this work.

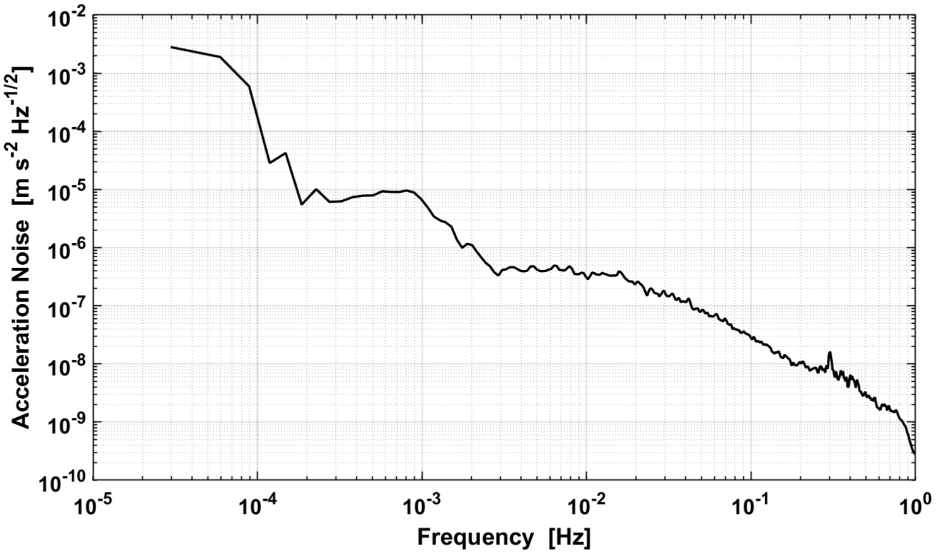

Figure 6.3: A photo of our optomechanical accelerometer setup using a quasi-monolithic inteferometer for test mass displacement measurement. This image can be compared to Figure 4.7 to visualize the size difference between the interferometers used in this work.

However, this measurement detected excess noise around $1\,\mathrm{mHz}$, which is similarly found in spectrum of the heterodyne signal amplitude. Figure 6.5 depicts the noise in the peak-to-peak heterodyne signal voltages of the measurement and reference interferometers, demonstrating that the reference interferometer found also found excess noise at $1\,\mathrm{mHz}$, but not the measurement interferometer. This indicates a periodic loss of fiber coupling efficiency due to a misalignment of the reference interferometer through tilting of the stationary reference mirror on the fused silica wafer or a mechanical instability of the output fiber collimation arm. The source of these mechanical instabilities are currently under investigation. To help diagnose these instabilities, quadrature photodetectors (QPDs) could be implemented into the setup to monitor the interferometer output beams. QPDs are photodetectors whose light detection surfaces are split into quadrants. If the output beams drift over time, the optical power on each quadrant will change. Hence, misalignments in the optical setup can be identified by comparing the relative intensities observed by each quadrant of the QPD.

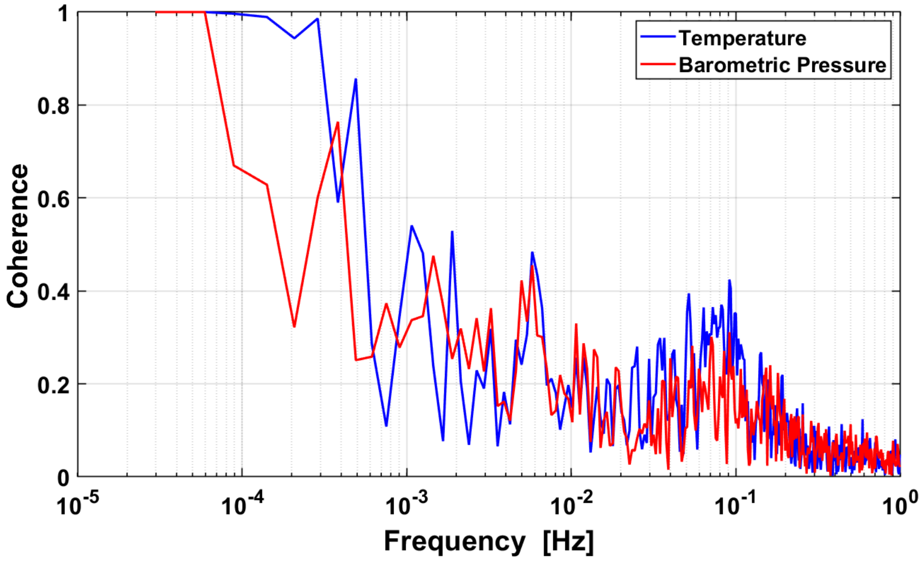

Figure 6.4: The coherences of temperature and barometric pressure with acceleration in our quasi-monolithic interferometer. Compared to measurements taken with the optical readout in Chapter 4, we observe a significant reduction in these coherences suggesting the quasi-monolithic interferometer is less susceptible to these noise sources.

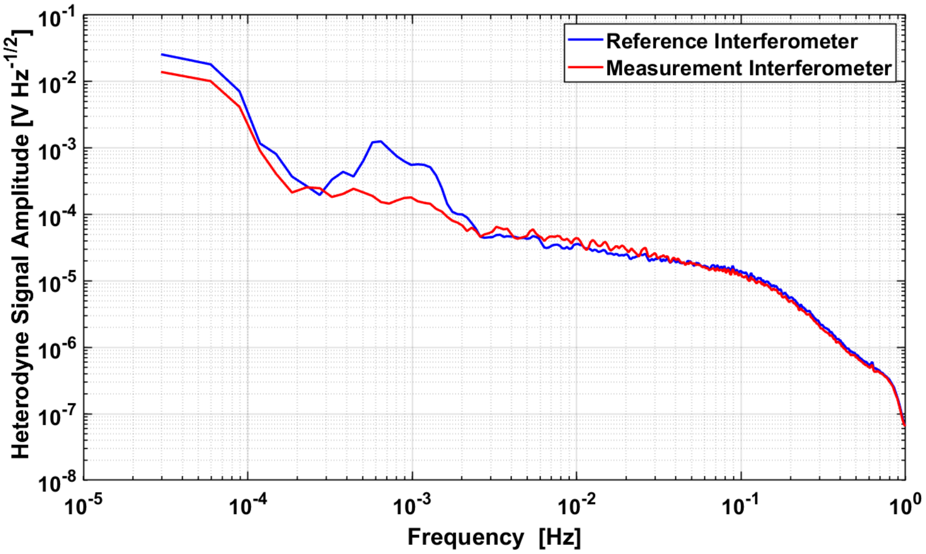

Figure 6.5: The amplitude spectral densities of the peak-to-peak voltage amplitude of the heterodyne beatnote in the measurement and reference arms of our quasi-monolithic interferometer. We observe the reference interferometer experienced excess noise around $1\,\mathrm{mHz}$, the same band of the excess noise in the corresponding acceleration measurement.

7. OPTOMECHANICAL RESONATOR TOPOLOGIES FOR OTHER APPLICATIONS *

7.1 Double-Mass Resonator for Extended Bandwidth Sensing

As shown in Chapter 3, low-frequency resonators are advantageous for detecting low-frequency noise due to the larger coupling factor between external acceleration and test mass motion. However, these resonators are simultaneously insensitive to accelerations at frequencies above resonance, which fundamentally limits the operational bandwidth of the accelerometer. For applications demanding the high-precision detection of noise both spanning multiple frequency regimes, the optomechanical resonator topology presented in Chapters 2-6 would not be sufficient. Rather, we propose an extension of this topology consisting of two resonators with different resonances to develop an optomechanical device appropriate for these applications. Both test masses use distinct optical readouts to take simultaneous measurements. Signals on the lower end of the detection band will couple more efficiently into the lower resonance test mass while signals on the higher end couple more efficiently into the higher resonance test mass. The two channels can be merged using a Kalman filter to create one data stream that contains the better performances of both test masses [63, 64]. For example, a double-mass resonator consisting of $10\,\mathrm{Hz}$ and $50\,\mathrm{Hz}$ would be suitable for detecting seismic noise in the sub-Hz regime as well as anthropogenic noise above $1\,\mathrm{Hz}$. Such a device, a photo of which is shown in Figure 7.1, could be used in LIGO detectors, which requirement the detection of vibrations both within and below their measurement bandwidth.

The noise floor of a double-mass optomechanical accelerometer can be estimated using the models developed in Chapters 2 and 4. Equations 4.2, 4.6 and 4.7 can be used to evaluate the acceleration noises of the two resonators, $\tilde{a}_{10}(\omega)$ and $\tilde{a}_{50}(\omega)$, independently. The noise of the merged signal is approximated as the smaller value of the two acceleration spectra at all frequencies:

$$\tilde{a}_{\text{merged}}(\omega) = \min(\tilde{a}_{10}(\omega), \tilde{a}_{50}(\omega)) \tag{7.1}$$

---

*Part of this chapter is reprinted with permission from "Quantum hybrid optomechanical inertial sensing" by Logan Richardson, Adam Hines, Andrew Schaffer, Brian P. Anderson, and Felipe Guzman, 2020. Applied Optics, Vol. 59, pp. pp. G160-G166, Copyright 2022 by Optica Publishing Group.

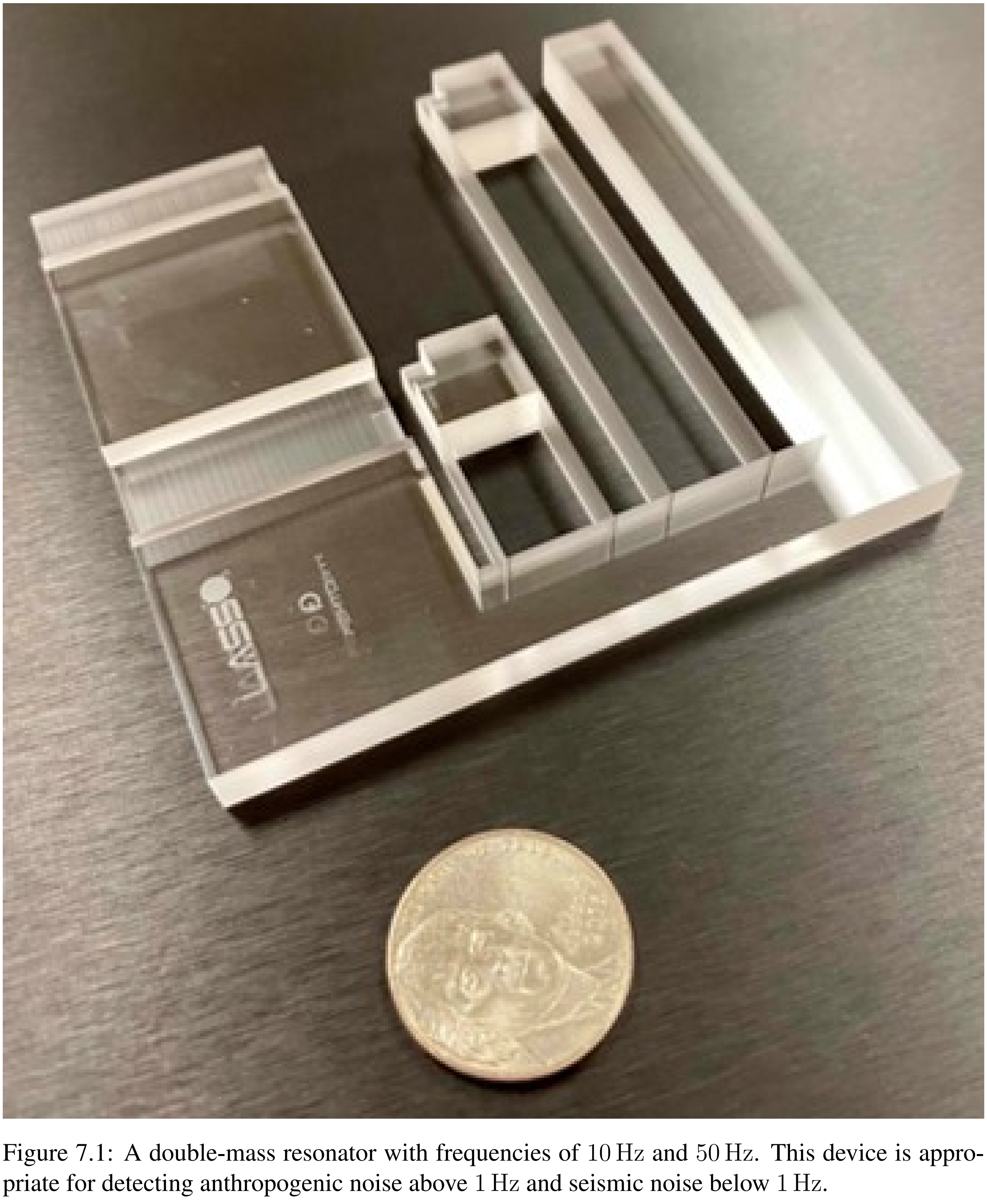

Figure 7.1: A double-mass resonator with frequencies of 10 Hz and 50 Hz. This device is appropriate for detecting anthropogenic noise above 1 Hz and seismic noise below 1 Hz.

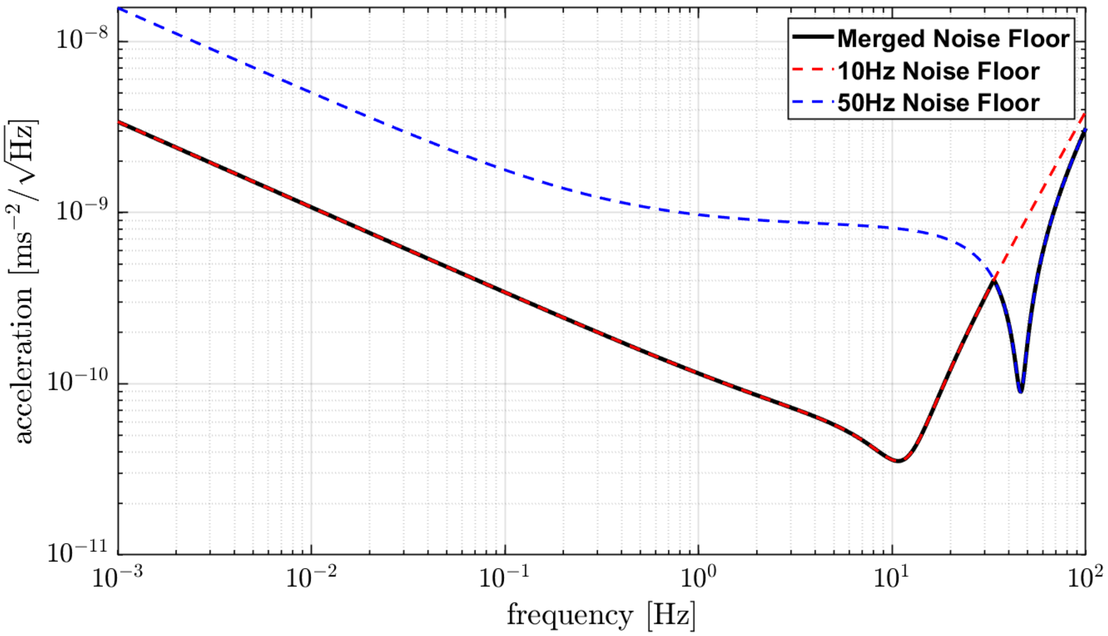

Figure 7.2: A double-mass resonator with frequencies of $10\,\mathrm{Hz}$ and $50\,\mathrm{Hz}$. The dashed lines represent the acceleration noises of the two test masses independently of each other, assuming $Q-$values of 4.77×10^5 and displacement readout sensitivities of $1 \times 10^{-14}\,\mathrm{mHz}^{-1/2}$. The solid line represent the acceleration noise of this optomechanical accelerometer when the data from its two test masses are merged with a Kalman filter.

Equation 7.1 is plotted in Figure 7.2, under the assumptions both the $10\,\mathrm{Hz}$ and $50\,\mathrm{Hz}$ resonators have mechanical $Q-$values of 4.77×10^5, a result that was experimentally demonstrated for a similar resonator in Chapter 4. Furthermore, we assume that the displacements of both resonators are measured using identical optical readouts, with a displacement sensitivity of $1 \times 10^{-14}\,\mathrm{mHz}^{-1/2}$. We observe that the use of two test masses for acceleration sensing lowers the resultant noise floor of the device by a factor of 5-10 relative to the noise floors of the independent test masses, allowing for improved broadband sensing.

7.2 Optomechanical Retroreflector for Novel Hybrid Atom Interferometer

In addition to standalone relative accelerometry solutions, optomechanical devices have the potential to compliment absolute gravimeters such as atom interferometers which suffer from non-inertial vibrations coupling into the apparatus. This section is based on the work in the following paper [2], which was written in collaboration with Dr. Logan Richardson, Dr. Brian Anderson, Dr. Felipe Guzman, and Andrew Schaffer. The description and analysis of the atom interferometer found below was conducted by Dr. Logan Richardson. I designed the optomechanical retroreflector intended to reflect the Raman beam and measure non-inertial accelerations within the atom interferometer.

Matter-wave interference of atoms enables repeatable precise measurement of inertial effects. Atom interferometry has been demonstrated with warm vapor, Bose–Einstein condensates, and in the case of this work, thermal cold atom clouds [65, 66]. We trap and cool an ensemble of atoms in a magneto-optical trap (MOT), and once this is loaded, the ensemble is released from the trap and falls along the direction of gravitational acceleration. By using timed pulses of light during free fall, we can manipulate the matter-wave state of the atoms in such a manner that we can detect the acceleration they experienced through their corresponding phase shift. We chose to perform interferometry with ^{87}Rb for compatibility with other atom interferometer systems.

During free fall we use counterpropagating two-photon Raman pulses to drive transitions between the two hyperfine states $|F = 1, m_F = 0\rangle$and $|F = 2, m_F = 0\rangle$of the $5^2S_{1/2}$ energy level of ^{87}Rb, which we simplify to $|1\rangle$and $|2\rangle$, respectively. We use these pulses to generate the matter-wave analogue of an optical beam splitter (π/2 pulse) and mirror (π pulse)[67]. By arranging these three pulses in a Mach–Zehnder-like configuration π/2 - π - π/2 with a separation time between pulses T we create a matter-wave interferometer sensitive to inertial effects.

To meet the Raman condition required for inertially sensitive interferometry [67], a two-beam counterpropagating configuration is realized by employing a retroreflection mirror. During the finite time required to measure acceleration with atom interferometers, retroreflector dynamics with frequencies higher than the measurement cycle frequency (f_c) couple into the interferometer and manifest as inertial noise in the measured matter-wave phase[68].

We designed the optomechanical retroreflector (OMRR) as a drumhead mechanical oscillator that will allow us to place and quasi-monolithically attach a fixed mirror to the sensor in order to

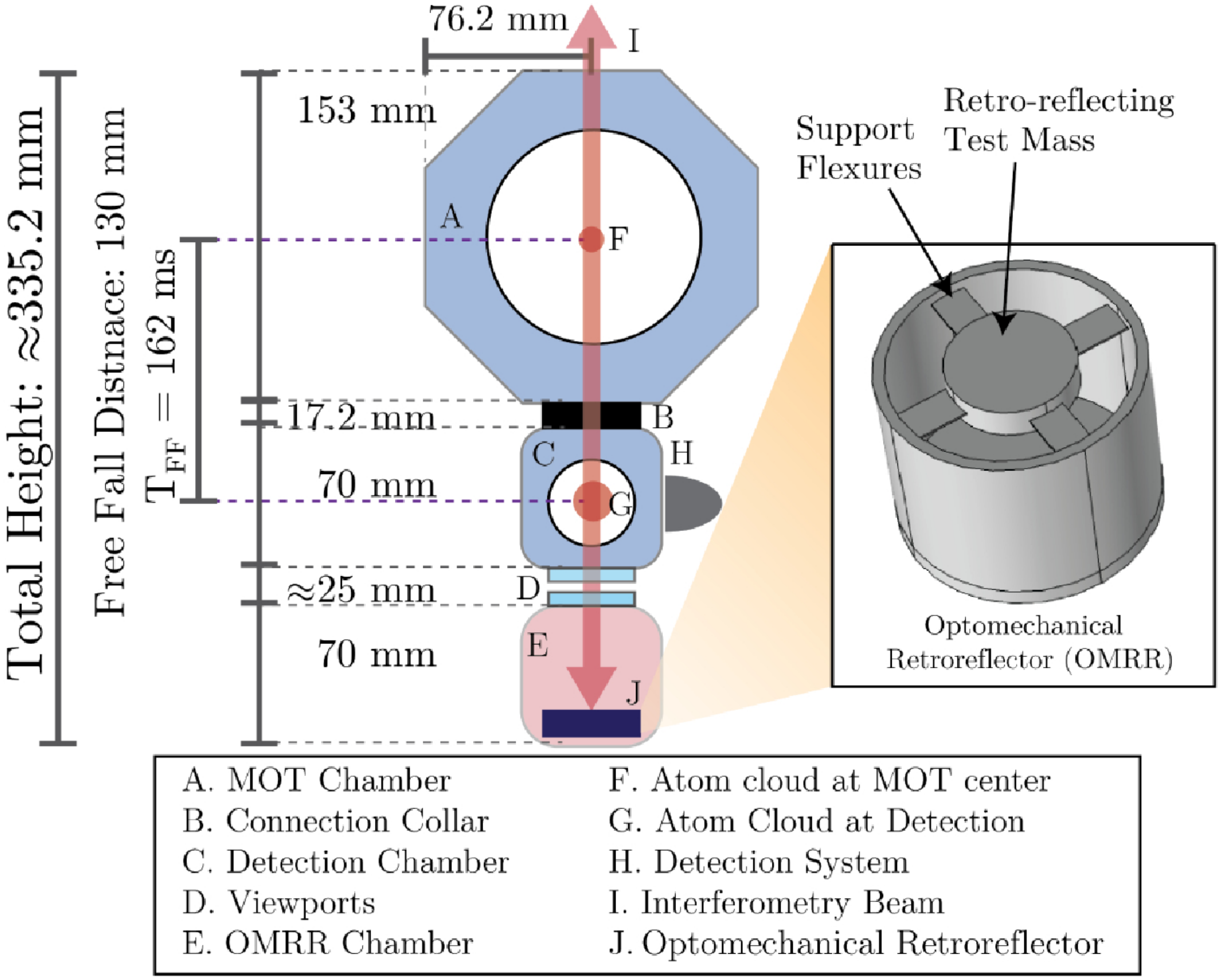

Figure 7.3: A diagram of the proposed testbed interferometer. The atom interferometer will consist of two separate vacuum systems at two different pressures: one for atom interferometry and one for the OMRR. The total free-fall distance from the center of the MOT to the detection region is roughly 130 mm corresponding to a total free-fall time of T_{FF}=162ms. The lower vacuum chamber will house the OMRR. A cutaway of the proposed OMRR can be seen depicting the retroreflecting test mass and support flexures. Atoms are cooled and trapped at the center of the MOT chamber (F), and once loading is complete, they are released into free fall. The interferometry beam (I) enters the system through the top of the MOT chamber (A) and is reflected off of the OMRR (J) along the axis of gravitational acceleration, generating a counterpropagating configuration that satisfies the conditions required for inertially sensitive interferometry. During free fall, three interferometry pulses separated by a pulse separation time T are used to generate a Mach–Zehnder-like interferometer. Once the atoms reach the detection area (G), the phase-dependent relative output population of the two-state system is measured, from which the acceleration of the atoms can be determined. Signal from the OMRR can be used to correct for vibrations occurring during atom interferometry, and the absolute measurement of the atom interferometer can be used to debias the OMRR signal at frequencies below the atom interferometer cycle rate. This figure is taken from [2].

complete the Fabry–Perot cavity to be used to measure the OMRR test mass displacement. We will coat the OMRR test mass on one (the inner) side with a highly reflective layer for 1560 nm light as part of the Fabry–Perot optics and on the other (outer) side to reflect the Raman beam at 780 nm that is used for atom interferometry. A diagram of the proposed atom interferometer with the optomechanical retroreflector is shown in Figure 7.3.

Physically, we are constrained to the dimensions of the 2.75" (69.85 mm) chamber cube shown in Figure 7.3, which has a bore distance of $\emptyset$=38.1mm. We run numerical analysis using COMSOL to determine a sensor design of suitable dimensions for this vacuum chamber. The optimized design yielded a cylindrical sensor with resonance $2\pi\times 1013.9\,\mathrm{Hz}$, a frame diameter of 35.5 mm, and a height of 27.9 mm. The test mass of the OMRR has a diameter of 17.3 mm, thickness of 3.6 mm, and mass of 2.3 g. The test mass is supported by four flexures; each flexure has a length of 7.6 mm, width of 5 mm, and thickness of 310 μm.

We modeled the dynamics of the OMRR sensor assuming a mechanical quality factor of 4.77×10^5 [7], and we conducted a finite element analysis to determine the first three mechanical modes, which are a) the fundamental test mass displacement mode at ω_0=$2\pi\times 1013.9\,\mathrm{Hz}$, b) a tip-tilt mode at ω_1=$2\pi\times 2045.4\,\mathrm{Hz}$ and c) a translational displacement mode at ω_0=$2\pi\times 18.4\,\mathrm{kHz}$. Figure 7.4 illustrates the fundamental oscillation of the sensor as well as these higher-order modes. Under a change of acceleration of 1 g, the maximum displacements for each mode are $2\times 10^{-7}\,\mathrm{m}$, $6\times 10^{-8}\,\mathrm{m}$, and $7\times 10^{-10}\,\mathrm{m}$, respectively. We designed the OMRR mechanics such that the frequency separation between the fundamental mode and higher-order modes, as well as any intermodal beats, occur at frequencies higher than ω_0 to minimize crosstalk.

The OMRR topology was optimizing following the procedure described in Chapter 3. Unlike the low-frequency parallelogram flexure design used throughout this dissertation, the flexure thickness of this new topology need not be constrained to a local maximum of the optimization criterion which is dominated by surface and thermoelastic losses. The higher frequency of the OMRR makes thicker flexures more accessible without the need for flexures that are impractically long. This is demonstrated in Figure 7.5, where we observe the Q-factor of this topology becomes

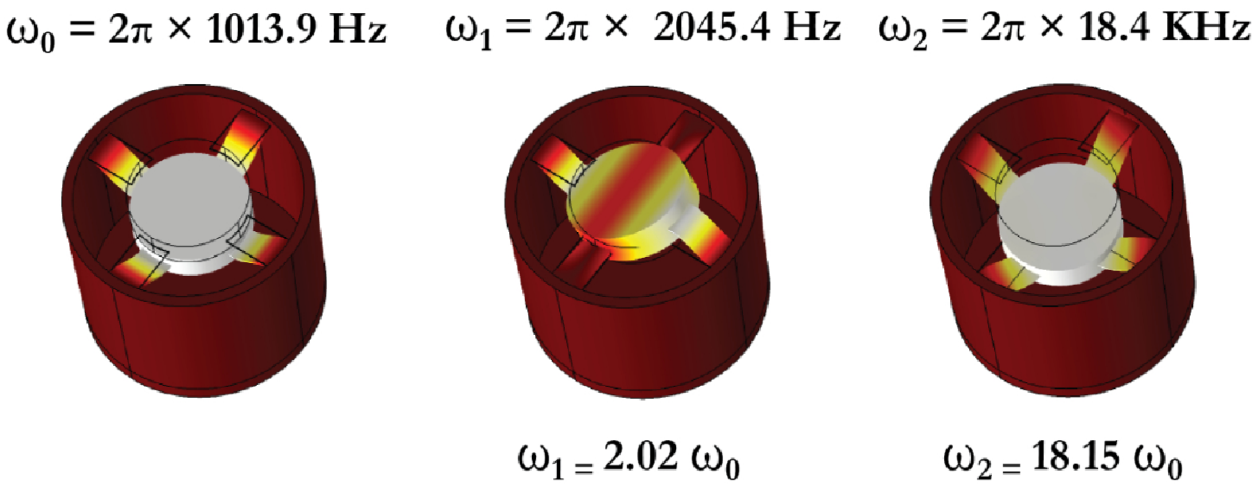

Figure 7.4: Modal finite element analysis of the fundamental and higher-order harmonics of the OMRR. Color indicates displacement from equilibrium, with red representing no displacement and white representing the maximum. The first harmonic is ω_1=$2\pi\times2045.4\,\mathrm{Hz}$ and the second harmonic is ω_0=$2\pi\times18.4\,\mathrm{kHz}$. Intentionally, the OMRR has been designed such that higher harmonics are high enough in frequency to avoid intermodal beat notes at frequencies at or below the fundamental resonance ω_0. This figure is taken from [2].

bulk-limited above $200\,\mu\mathrm{m}$. This is advantageous as the a bulk-limited resonator is anticipated to be less sensitive to its surface quality, which is highly dependent on fabrication limitations. At the chosen flexure thickness of $310\,\mu\mathrm{m}$, we the mechanical losses of fused silica predict a Q-factor of approximately 4×10^6.

Furthermore, the acceleration and displacement noise floors of the OMRR can be modeled using the work presented in Chapters 2 and 4. Because the OMRR has a resonance around $1\,\mathrm{kHz}$, the test mass' dynamic range is expected to be less than $0.25\,\mu\mathrm{m}$, indicating that this resonator's displacement is suitable for an optical cavity readout. High finesse cavities have demonstrated displacement sensitivities on the order of $1 \times 10^{-16}\,\mathrm{mHz}^{-1/2}$ and we use this result to estimate the noise floor of the OMRR [22]. Despite the topology optimization suggesting the feasibility of Q-values above 1×10^6, we assume a more conservative Q-factor of 4.77×10^5 for modelling the thermal motion of the OMRR. The displacement and acceleration noise floors are shown in Figure 7.6, where we observe that despite the high-precision displacement readout, the OMRR is only expected to be thermally-limited below $10\,\mathrm{Hz}$. The acceleration noise floor is projected to reach

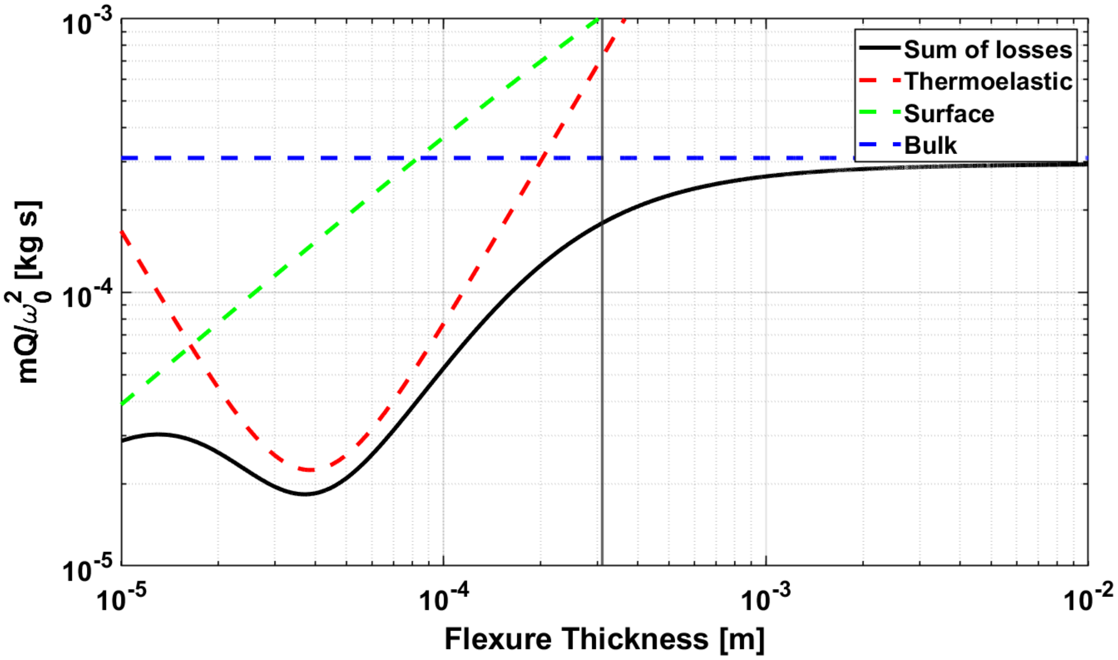

Figure 7.5: The optimization curve of the optomechanical retroreflector topology following the steps described in Chapter 3. The flexure thickness was chosen to be $310\,\mu\mathrm{m}$, which corresponds to a mechanical Q-value of approximately 4×10^6.

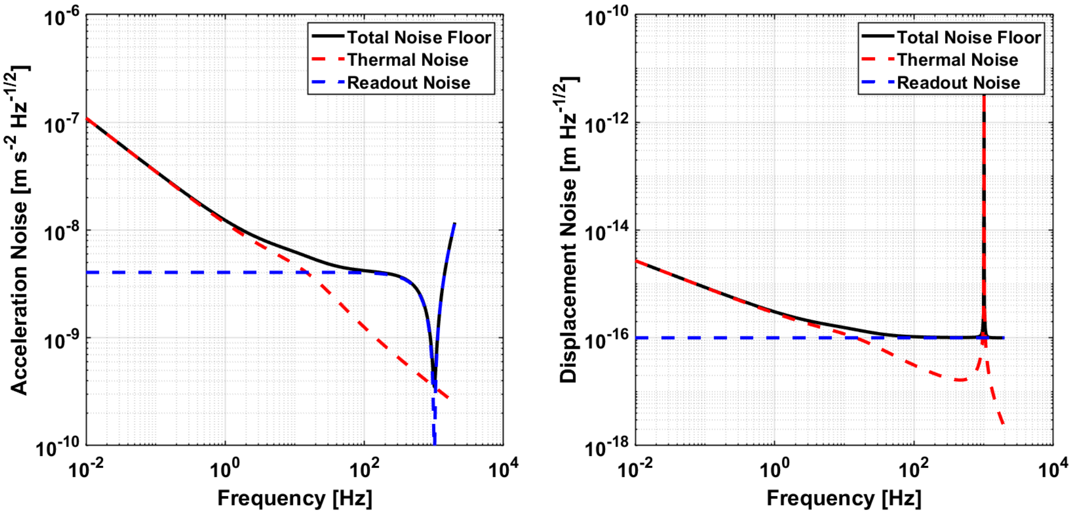

Figure 7.6: Simulations of the thermal motion and optical readout noise in our optomechanical retroreflector using the models developed in Chapters 2 and 4. We assume a mechanical Q-factor of 4.77×10^5 [7] and a displacement readout noise on the order of $1 \times 10^{-16}\,\mathrm{mHz}^{-1/2}$. From the displacement noise floor (left) we expect our acceleration noise floor (right) to be thermally limited below $10\,\mathrm{Hz}$.

sensitivities of $4 \times 10^{-9}\,\mathrm{ms}^{-2}\mathrm{Hz}^{-1/2}$ at higher frequencies with a $1/f^{1/2}$ low-frequency tail.

8. CONCLUSION

This dissertation details our development of an optomechanical accelerometer that couples a $5\,\mathrm{Hz}$ fused silica mechanical resonator with a heterodyne laser interferometer readout. This accelerometer is designed to detect signals in the sub-Hz regime, making it suitable for seismology, geophysics, gravitational wave detectors, inertial navigation, and more. Moreover, its compact, portable form and inherent vacuum compatibility make it a possible solution for geoscience field work and satellite geodesy missions. Our work encompasses the simulation, design, and optimization of mechanical resonator topologies as well as the assembly and testing of the optomechanical accelerometer. Preliminary measurements have demonstrated excellent coherence with a commercial seismometer at frequencies down to $1\,\mathrm{mHz}$ and have revealed several dominant noise soures including temperature fluctuations, barometric pressure fluctuations, and laser frequency noise.

The work in this dissertation can be furthered in several ways. Our optomechanical accelerometer is currently dominated by noise from various seismic and environmental sources that prevent us from resolving the device's noise floor. However, the simultaneous measurements of two identical optomechanical accelerometers all for the detection of common-mode noise between both sensors. A differential measurement of the two accelerometers would reject that common-mode noise, leaving only uncorrelated noise. In this way we can estimate the true acceleration noise floor of our accelerometer. Furthermore, it was found in Chapter 4 that temperature drifts restrict our sensitivity at very low frequencies with relatively high coupling factors on the order of $1 \times 10^{-3}\,\mathrm{ms^{-2}K^{-1}}$. This effect likely originated from a measurement arm length difference of our two interferometers, and reducing this arm length difference in Chapter 6 reduced the effects of temperature noise at higher frequencies. However, temperature drifts were still found to introduce noise at very low frequencies even with our quasi-monolithic interferometer and methods of decoupling our accelerometer from temperature should be investigated and implemented. Similarly, in Chapter 4 we observed a strong coupling of laser frequency noise to acceleration noise and estimated that a laser frequency stability of approximately $1\,\mathrm{kHzHz^{-1/2}}$ is required to achieve a thermally-limited acceleration measurement. This stability requirement can be accomplished with existing stabilization techniques [56], and should be utilized in this experiment.

Finally, we present two new resonator topolgies useful for different applications. The double-mass resonator uses two test masses with different resonant frequencies to extend the operational bandwidth of the resulting accelerometer. This device would be suitable as auxiliary sensors in gravitational wave detectors for the observation of both seismic noise and anthropogenic noise that couple into the detector measurements. Furthermore, we present the design of an optomechanical retroreflector for use in atom interferometers, which use a retroreflector to create counter-propagating Raman beams. This retroreflecting mirror however is susceptible to external vibrations which couple into the atom interferometer by phase-shifting the Raman beam wavefront. To overcome this effect, our optomechanical retroreflector is a drum-head shaped resonator where both sides of the drum test mass take simultaneous measurements. The top surface of the test mass is given a reflective coating to form the Raman beam retroreflector while the bottom surface is used to create an optical cavity which tracks the motion of the test mass. The vibration measurements obtained through the optical cavity can be used to remove the non-inertial noise added to the atom interferometer. In this way, our optomechanical retroreflector allows for the creation of a hybrid inertial sensor with a quantum atom interferometer for absolute gravimetry and long term stability coupled with a classical relative accelerometer for seismic detection.

REFERENCES

[1] Yanqi Zhang, Adam S Hines, Guillermo Valdes, and Felipe Guzman. Investigation and mitigation of noise contributions in a compact heterodyne interferometer. *Sensors*, 21(17):5788, 2021.

[2] Logan Richardson, Adam Hines, Andrew Schaffer, Brian P. Anderson, and Felipe Guzman. Quantum hybrid optomechanical inertial sensing. *arXiv:2005.08405*, 2020.

[3] M. Armano, H. Audley, G. Auger, J. T. Baird, M. Bassan, P. Binetruy, M. Born, D. Bortoluzzi, N. Brandt, M. Caleno, L. Carbone, A. Cavalleri, A. Cesarini, G. Ciani, G. Congedo, A. M. Cruise, K. Danzmann, M. de Deus Silva, R. De Rosa, M. Diaz-Aguiló, L. Di Fiore, I. Diepholz, G. Dixon, R. Dolesi, N. Dunbar, L. Ferraioli, V. Ferroni, W. Fichter, E. D. Fitzsimons, R. Flatscher, M. Freschi, A. F. García Marín, C. García Marirrodriga, R. Gerndt, L. Gesa, F. Gibert, D. Giardini, R. Giusteri, F. Guzmán, A. Grado, C. Grimani, A. Grynagier, J. Grzymisch, I. Harrison, G. Heinzel, M. Hewitson, D. Hollington, D. Hoyland, M. Hueller, H. Inchauspé, O. Jennrich, P. Jetzer, U. Johann, B. Johlander, N. Karnesis, B. Kaune, N. Korsakova, C. J. Killow, J. A. Lobo, I. Lloro, L. Liu, J. P. López-Zaragoza, R. Maarschalkerweerd, D. Mance, V. Martín, L. Martin-Polo, J. Martino, F. Martin-Porqueras, S. Madden, I. Mateos, P. W. McNamara, J. Mendes, L. Mendes, A. Monsky, D. Nicolodi, M. Nofrarias, S. Paczkowski, M. Perreur-Lloyd, A. Petiteau, P. Pivato, E. Plagnol, P. Prat, U. Ragnit, B. Raïs, J. Ramos-Castro, J. Reiche, D. I. Robertson, H. Rozemeijer, F. Rivas, G. Russano, J. Sanjuán, P. Sarra, A. Schleicher, D. Shaul, J. Slutsky, C. F. Sopuerta, R. Stanga, F. Steier, T. Sumner, D. Texier, J. I. Thorpe, C. Trenkel, M. Tröbs, H. B. Tu, D. Vetrugno, S. Vitale, V. Wand, G. Wanner, H. Ward, C. Warren, P. J. Wass, D. Wealthy, W. J. Weber, L. Wissel, A. Wittchen, A. Zambotti, C. Zanoni, T. Ziegler, and P. Zweifel. Sub-femto-g free fall for space-based gravitational wave observatories: Lisa pathfinder results. *Phys. Rev. Lett.*, 116:231101, Jun 2016.

[4] Jakob Flury, Srinivas Bettadpur, and Byron D Tapley. Precise accelerometry onboard the grace gravity field satellite mission. *Advances in Space Research*, 42(8):1414–1423, 2008.

[5] Tamara Bandikova, Christopher McCullough, Gerhard L. Kruizinga, Himanshu Save, and Bruno Christophe. Grace accelerometer data transplant. *Advances in Space Research*, 64(3):623–644, 2019.

[6] Private communication, r. middlemiss, ligo scientific collaboration, 2019.

[7] Adam Hines, Andrea Nelson, Yanqi Zhang, Guillermo Valdes, Jose Sanjuan, Jeremiah Stoddart, and Felipe Guzmán. Optomechanical accelerometers for geodesy. *Remote Sensing*, 14(17), 2022.

[8] Heewon Jeong, Kiyoko Yamanaka, Yasushi Goto, Takanori Aono, and Masahide Hayashi. Three-axis mems inertial sensor for automobile applications. In *SENSORS, 2011 IEEE*, pages 444–447. IEEE, 2011.

[9] Jacques Leclerc. Mems for aerospace navigation. *IEEE Aerospace and Electronic Systems Magazine*, 22(10):31–36, 2007.

[10] Shilong Yu and Long Qin. Human activity recognition with smartphone inertial sensors using bidir-lstm networks. In *2018 3rd international conference on mechanical, control and computer engineering (icmcce)*, pages 219–224. IEEE, 2018.

[11] B. D. Tapley, S. Bettadpur, M. Watkins, and C. Reigber. The gravity recovery and climate experiment: Mission overview and early results. *Geophysical Research Letters*, 31(9), 2004.

[12] Richard P Kornfeld, Bradford W Arnold, Michael A Gross, Neil T Dahya, William M Klipstein, Peter F Gath, and Srinivas Bettadpur. Grace-fo: the gravity recovery and climate experiment follow-on mission. *Journal of spacecraft and rockets*, 56(3):931–951, 2019.

[13] Nanometrics Inc. Trillium horizon 120. `https://www.nanometrics.ca/products/seismometers/trillium-horizon-120`.

[14] Kenji Numata, Shigemi Otsuka, Masaki Ando, and Kimio Tsubono. Intrinsic losses in various kinds of fused silica. *Classical and Quantum Gravity*, 19(7):1697–1702, mar 2002.

[15] William J. Startin, Mark A. Beilby, and Peter R. Saulson. Mechanical quality factors of fused silica resonators. *Review of Scientific Instruments*, 69(10):3681–3689, 1998.

[16] Joris Vincent van Heijningen. A fifty-fold improvement of thermal noise limited inertial sensitivity by operating at cryogenic temperatures. *Journal of Instrumentation*, 15(06):P06034, 2020.

[17] R.P. Middlemiss, A. Samarelli, D.J. Paul, J. Hough, S. Rowan, and G.D. Hammond. Measurement of the earth tides with a mems gravimeter. *Nature*, 531:614–617, 2016.

[18] Zhu Li, Wen Jie Wu, Pan Pan Zheng, Jin Quan Liu, Ji Fan, and Liang Cheng Tu. Novel capacitive sensing system design of a microelectromechanical systems accelerometer for gravity measurement applications. *Micromachines*, 7(9), 2016.

[19] John T. Melcher, Julian Stirling, Felipe Guzman, Jon R. Pratt, and Gordon A. Shaw. A self-calibrating optomechanical force sensor with femtonewton resolution. *Applied Physics Letters*, 105:233109, 2014.

[20] M. F. Colombano, G. Arregui, F. Bonell, N. E. Capuj, E. Chavez-Angel, A. Pitanti, S. O. Valenzuela, C. M. Sotomayor-Torres, D. Navarro-Urrios, and M. V. Costache. Ferromagnetic resonance assisted optomechanical magnetometer. *Phys. Rev. Lett.*, 125:147201, Oct 2020.

[21] Tianran Liu, Francesco Pagliano, René van Veldhoven, Vadim Pogoretskiy, Yuqing Jiao, and Andrea Fiore. Integrated nano-optomechanical displacement sensor with ultrawide optical bandwidth. *Nat Commun*, 11, May 2020.

[22] Felipe Guzman, Lee Kumanchik, Jon Pratt, and Jacob M. Taylor. High sensitivity optomechanical reference accelerometer over 10 khz. *Applied Physics Letters*, 104(22):221111, 2014.

[23] Adam Hines, Logan Richardson, Hayden Wisniewski, and Felipe Guzman. Optomechanical inertial sensors. *Appl. Opt.*, 59(22):G167–G174, Aug 2020.

[24] Zhili Hao and F. Ayazi. Support loss in micromechanical disk resonators. *18th IEEE International Conference on Micro Electro Mechanical Systems, 2005. MEMS 2005.*, pages 137–141, 2005.

[25] B. Le Foulgoc, O. Le Traon, S. Masson, A. Parent, T. Bourouina, F. Marty, A. Bosseboeuf, F. Parrain, H. Mathias, and J. . Gilles. High-q silicon flexural resonators for vibrating inertial sensors: Investigations of the limiting damping mechanisms. In *SENSORS, 2006 IEEE*, pages 1365–1368, Oct 2006.

[26] Zhili Hao and Yang Xu. Vibration displacement on substrate due to time-harmonic stress sources from a micromechanical resonator. *Journal of Sound and Vibration*, 322(1):196 – 215, 2009.

[27] Lucien Lacoste, Neal Clarkson, and George Hamilton. Lacoste and romberg stabilized platform shipboard gravity meter. *Geophysics*, 32(1):99–109, 1967.

[28] J. Weber and J. V. Larson. Operation of lacoste and romberg gravimeter at sensitivity approaching the thermal fluctuation limits. *Journal of Geophysical Research (1896-1977)*, 71(24):6005–6009, 1966.

[29] Scintrex. *CG-6 Autograv Survey Gravity Meter*. Scintrex.

[30] John M. Goodkind. The superconducting gravimeter. *Review of Scientific Instruments*, 70(11):4131–4152, 1999.

[31] W. A. Prothero and J. M. Goodkind. Earth-tide measurements with the superconducting gravimeter. *Journal of Geophysical Research (1896-1977)*, 77(5):926–937, 1972.

[32] R.J. Warburton, H. Pillai, and R.C. Reineman. Initial results with the new gwr igrav™ superconducting gravity meter. *International Association of Geodesy (IAG) Symposium Proceedings*, page 10, 2010.

[33] A. Prasad, S. G. Bramsiepc, R. P. Middlemiss, J. Hough, S. Rowan, G. D. Hammond, and D. J. Paul. A portable mems gravimeter for the detection of the earth tides. In *2018 IEEE SENSORS*, pages 1–3, Oct 2018.

[34] Micro g LaCoste. Fg5 absolute gravimeter user's manual. *Micro-g LaCoste*, 2006.

[35] K. Bongs, M. Holynski, J. Vovrosh, P. Bouyer, G. Condon, E. Rasel, C. Schubert, W.P Schleich, and A. Roura. Taking atom interferometric quantum sensors from the laboratory to real-world applications. *Nature Review Physics*, 1:731–739, 2019.

[36] S Merlet, J Le Gouët, Q Bodart, A Clairon, A Landragin, F Pereira Dos Santos, and P Rouchon. Operating an atom interferometer beyond its linear range. *Metrologia*, 46(1):87–94, 2009.

[37] Felipe Guzman, Lee Michael Kumanchik, Jacob M. Taylor, and Jon R. Pratt. Optomechanical gravimeter, 2017. US Patent 10,545,259.

[38] A Cumming, A Heptonstall, R Kumar, W Cunningham, C Torrie, M Barton, K A Strain, J Hough, and S Rowan. Finite element modelling of the mechanical loss of silica suspension fibres for advanced gravitational wave detectors. *Classical and Quantum Gravity*, 26(21):215012, oct 2009.

[39] A V Cumming, A S Bell, L Barsotti, M A Barton, G Cagnoli, D Cook, L Cunningham, M Evans, G D Hammond, G M Harry, A Heptonstall, J Hough, R Jones, R Kumar, R Mittleman, N A Robertson, S Rowan, B Shapiro, K A Strain, K Tokmakov, C Torrie, and A A van Veggel. Design and development of the advanced LIGO monolithic fused silica suspension. *Classical and Quantum Gravity*, 29(3):035003, jan 2012.

[40] Ki-Nam Joo, Erin Clark, Yanqi Zhang, Jonathan D. Ellis, and Felipe Guzman. A compact high-precision periodic-error-free heterodyne interferometer. *arXiv:2004.13837*, 2020.

[41] Alexandr Ageev, Belkis Cabrera Palmer, Antonio De Felice, Steven D Penn, and Peter R Saulson. Very high quality factor measured in annealed fused silica. *Classical and Quantum Gravity*, 21(16):3887–3892, jul 2004.

[42] A. Di Virgilio, S. Bigotta, L. Barsotti, S. Braccini, C. Bradaschia, G. Cella, V. Dattilo, M. Del Prete, I. Ferrante, F. Fidecaro, I. Fiori, F. Frasconi, A. Gennai, A. Giazotto, P. La Penna, G. Losurdo, E. Majorana, M. Mantovani, F. Paoletti, R. Passaquieti, D. Pas-

suello, F. Piergiovanni, A. Porzio, P. Puppo, F. Raffaelli, P. Rapagnani, F. Ricci, S. Solimeno, G. Vajente, and F. Vetrano. Experimental upper limit on the estimated thermal noise at low frequencies in a gravitational wave detector. *Phys. Rev. D*, 76:122004, Dec 2007.

[43] Peter R. Saulson. Thermal noise in mechanical experiments. *Phys. Rev. D*, 42:2437–2445, 1990.

[44] Steven D. Penn, Alexander Ageev, Dan Busby, Gregory M. Harry, Andri M. Gretarsson, Kenji Numata, and Phil Willems. Frequency and surface dependence of the mechanical loss in fused silica. *Physics Letters A*, 352(1):3 – 6, 2006.

[45] Andri M. Gretarsson, Gregory M. Harry, Steven D. Penn, Peter R. Saulson, William J. Startin, Sheila Rowan, Gianpietro Cagnoli, and Jim Hough. Pendulum mode thermal noise in advanced interferometers: a comparison of fused silica fibers and ribbons in the presence of surface loss. *Physics Letters A*, 270(3):108 – 114, 2000.

[46] Mehmet Colakoglu. Factors effecting internal damping in aluminum. *JOURNAL OF THEORETICAL AND APPLIED MECHANICS*, 42:95–105, 01 2004.

[47] S. Bianco, M. Cocuzza, S. Ferrero, E. Giuri, G. Piacenza, C. F. Pirri, A. Ricci, L. Scaltrito, D. Bich, A. Merialdo, P. Schina, and R. Correale. Silicon resonant microcantilevers for absolute pressure measurement. *Journal of Vacuum Science & Technology B: Microelectronics and Nanometer Structures Processing, Measurement, and Phenomena*, 24(4):1803–1809, 2006.

[48] FEMTOprint. 3d glass microdevices | femtoprint. `https://www.femtoprint.ch/`.

[49] Yanqi Zhang, Adam S. Hines, Guillermo Valdes, and Felipe Guzman. Investigation and mitigation of noise contributions in a compact heterodyne interferometer. *Sensors*, 21(17), 2021.

[50] Peter R. Saulson. Thermal noise in mechanical experiments. *Phys. Rev. D*, 42:2437–2445, Oct 1990.

[51] Mohammed J. Ahamed, Doruk Senkal, and Andrei M. Shkel. Effect of annealing on mechanical quality factor of fused quartz hemispherical resonator. In *2014 International Symposium on Inertial Sensors and Systems (ISISS)*, pages 1–4, 2014.

[52] Tal Nagourney, Jae Yoong Cho, Behrouz Shiari, Ali Darvishian, and Khalil Najafi. 259 second ring-down time and 4.45 million quality factor in 5.5 khz fused silica birdbath shell resonator. In *2017 19th International Conference on Solid-State Sensors, Actuators and Microsystems (TRANSDUCERS)*, pages 790–793, 2017.

[53] Sajal Singh, Tal Nagourney, Jae Yoong Cho, Ali Darvishian, Khalil Najafi, and Behrouz Shiari. Design and fabrication of high-q birdbath resonator for mems gyroscopes. In *2018 IEEE/ION Position, Location and Navigation Symposium (PLANS)*, pages 15–19, 2018.

[54] Anja Schroeter, Ronny Nawrodt, Roman Schnabel, Stuart Reid, Iain Martin, Sheila Rowan, Christian Schwarz, Torsten Koettig, Ralf Neubert, Matthias Thürk, et al. On the mechanical quality factors of cryogenic test masses from fused silica and crystalline quartz. *arXiv preprint arXiv:0709.4359*, 2007.

[55] Texas A&M University Department of Atmospheric Sciences. Mesonet site. `https://atmo.tamu.edu/facilities-resources/mesonet-site/index.html`.

[56] R Thompson, WM Folkner, Glenn De Vine, WM Klipstein, Kirk McKenzie, Robert Spero, N Yu, M Stephens, J Leitch, R Pierce, et al. A flight-like optical reference cavity for grace follow-on laser frequency stabilization. In *2011 Joint conference of the IEEE international frequency control and the European frequency and time forum (FCS) proceedings*, pages 1–3. IEEE, 2011.

[57] M Nofrarias, F Gibert, N Karnesis, AF Garcia, M Hewitson, G Heinzel, and K Danzmann. Subtraction of temperature induced phase noise in the lisa frequency band. *Physical review D*, 87(10):102003, 2013.

[58] Julius S Bendat. Statistical errors in measurement of coherence functions and input/output quantities. *Journal of Sound and Vibration*, 59(3):405–421, 1978.

[59] Ltpda: a matlab toolbox for accountable and reproducible data analysis. `https://www.elisascience.org/ltpda/`.

[60] David N Wiese, Robert S Nerem, and Shin-Chan Han. Expected improvements in determining continental hydrology, ice mass variations, ocean bottom pressure signals, and earthquakes using two pairs of dedicated satellites for temporal gravity recovery. *Journal of Geophysical Research: Solid Earth*, 116(B11), 2011.

[61] Warren C Young, Richard G Budynas, and Ali M Sadegh. *Roark's formulas for stress and strain*. McGraw-Hill Education, 2012.

[62] Kalyan Rapolu, Shannon Dugan, Matthew Manelis, Jonathan Weldon, and Richard Wessel. Kapton rs flexible heaters–design and applications. In *2018 17th IEEE Intersociety Conference on Thermal and Thermomechanical Phenomena in Electronic Systems (ITherm)*, pages 19–25. IEEE, 2018.

[63] Greg Welch, Gary Bishop, et al. An introduction to the kalman filter. 1995.

[64] Gregory F Welch. Kalman filter. *Computer Vision: A Reference Guide*, pages 1–3, 2020.

[65] Kai Bongs, Michael Holynski, Jamie Vovrosh, Philippe Bouyer, Gabriel Condon, Ernst Rasel, Christian Schubert, Wolfgang P Schleich, and Albert Roura. Taking atom interferometric quantum sensors from the laboratory to real-world applications. *Nature Reviews Physics*, 1(12):731–739, 2019.

[66] Alexander D Cronin, Jörg Schmiedmayer, and David E Pritchard. Optics and interferometry with atoms and molecules. *Reviews of Modern Physics*, 81(3):1051, 2009.

[67] Mark Kasevich and Steven Chu. Measurement of the gravitational acceleration of an atom with a light-pulse atom interferometer. *Applied Physics B*, 54(5):321–332, 1992.

[68] Patrick Cheinet, Benjamin Canuel, Franck Pereira Dos Santos, Alexandre Gauguet, Florence Yver-Leduc, and Arnaud Landragin. Measurement of the sensitivity function in a time-domain atomic interferometer. *IEEE Transactions on instrumentation and measurement*, 57(6):1141–1148, 2008.